

Time-domain investigation of the  
ro-vibrational  $\text{CH}_4$   $\nu_2$  Raman  
spectrum via fs/ps CRS for  
combustion diagnostics

**M.Sc. Thesis**

**O.L. Thornquist**



# Time-domain investigation of the ro-vibrational $\text{CH}_4$ $\nu_2$ Raman spectrum via fs/ps CRS for combustion diagnostics

## M.Sc. Thesis

by

O.L. Thornquist

to obtain the degree of Master of Science  
at the Delft University of Technology,

to be defended publicly on Monday December 19, 2022 at 12:00 PM.

Student number:	5112370	
Thesis committee:	Prof. dr. ing. G. Eitelberg,	TU Delft, chair
	Dr. A. Anisimov,	TU Delft, external examiner
	Dr. ir. A. Bohlin,	TU Delft, principal supervisor
	Ir. F. Mazza,	TU Delft, daily supervisor

An electronic version of this thesis is available at <http://repository.tudelft.nl/>.



# Summary

With the onset of climate change and its calamitous consequences, it is crucial to investigate technological solutions to reduce or eliminate emissions. This impetus is particularly significant for the aviation industry, which relies on the energy density of jet fuel and its combustion in gas turbine engines. To improve the design of aircraft combustors, it is necessary to utilize computational models that are validated with experiments for accurate results. However, acquiring experimental data in the turbulent, multi-phase environment of a combustion chamber is often difficult. Fortunately, the advancements in laser diagnostics over the past few decades have extended their capabilities for combustion research by achieving non-intrusive measurements in gas-phase flows with high resolution. Out of all the laser diagnostic techniques, hybrid femtosecond/picosecond (fs/ps) coherent Raman scattering (CRS) is considered the gold standard for temperature and species concentration measurements in gas flows and flames. Through employing ultrashort laser pulses, this technique can perform time- and frequency-resolved measurements; a degenerate fs-duration pump/Stokes pulse excites the Raman-active modes of the target molecule, while a ps-duration probe pulse is scattered from the excited molecules to generate a coherent signal.

For this thesis project, the goal was to develop hybrid fs/ps CRS spectroscopy for the  $\nu_2$  vibrational mode of methane. Methane merits investigation due to its status as a short-lived climate forcer alongside its prospective use in the carbon-neutral production of hydrogen. While laser diagnostics have been traditionally applied to methane's  $\nu_1$  mode, the  $\nu_2$  mode spectrally overlaps with several other species in a "molecular fingerprint" region and offers potential multi-species detection significant for combustion. To characterize the  $\nu_2$  mode of methane the thesis focuses on three main areas: the behavior of the mode on a collision-independent timescale, the collisional dephasing of the mode at longer timescales, and the spectroscopy of the mode in a laminar diffusion flame. An overall time-domain CRS model was constructed using a methane spectral database and supplemented with a modified exponential gap (MEG) model for the calculation of collisional dephasing coefficients, or Raman linewidths, needed at longer timescales.

In this work, time-resolved CRS spectroscopy of the  $\text{CH}_4$   $\nu_2$  mode was performed at ambient conditions with single-shot measurements for the collision-independent timescale below 100 ps and shot-averaged measurements for a collision-dependent timescale up to 220 ps. For collision-independent measurements, the model was able to replicate the intensity "beating patterns" of spectral lines while considering only the fundamental mode and neglecting vibrational hot bands. For the collision-dependent timescale, the main effort was the extraction of molecule-specific dephasing linewidths of the Q-branch ( $\Delta J = 0$ ) through fitting parameters of the MEG model. The resulting fit of the model agreed well with experimental measurements, although several limitations were identified and discussed for further improvements. Similar measurements were also performed for gas mixtures of  $\text{CH}_4$  with  $\text{N}_2$ , Ar, and  $\text{H}_2$  to investigate the effect of collisional partners on the signal decay.

Finally, CRS spectroscopy was performed in a laminar  $\text{CH}_4$ -air diffusion flame to assess the potential of multi-species detection in the molecular fingerprint region. Spatially-resolved measurements were taken at a collision-independent probe delay across the flame front starting at the fuel stream, progressing to the reaction zone, then ending in the oxidizer stream. Four different chemical species were observed: the  $\text{CH}_4$   $\nu_2$  ro-vibrational spectrum, the  $\text{CO}_2$  Fermi dyad, pure-rotational lines of  $\text{H}_2$ , and the  $\text{O}_2$  ro-vibrational spectrum. In addition, the fundamental physical-chemical processes were observed through the Raman spectrum of these species such as  $\text{CH}_4$  dissociation,  $\text{H}_2$  synthesis and consumption, mass diffusion, and fuel/oxidizer mixing. Overall, the project demonstrates the feasibility of CRS measurements for temperature and concentration quantification of the  $\text{CH}_4$   $\nu_2$  mode and of the greater molecular fingerprint region. With continued improvements to the model, there is great promise for further *in-situ* measurements of  $\text{CH}_4$ -rich environments and more complex combustion diagnostics.



# Contents

<b>1</b>	<b>Introduction</b>	<b>1</b>
1.1	Background . . . . .	1
1.2	Motivation and outline . . . . .	2
<b>2</b>	<b>Theoretical Background</b>	<b>3</b>
2.1	Molecular structure and spectra . . . . .	3
2.1.1	Molecular energy states . . . . .	3
2.1.1.1	Rotational motion and energy levels . . . . .	3
2.1.1.2	Vibrational motion and energy levels . . . . .	5
2.1.2	Energy level transitions and selection rules . . . . .	6
2.1.2.1	Rotational selection rules . . . . .	7
2.1.2.2	Vibrational selection rules . . . . .	8
2.1.2.3	Rotation-vibration selection rules . . . . .	8
2.1.3	Population distribution . . . . .	10
2.2	Fundamentals of coherent Raman scattering . . . . .	11
2.2.1	Scattering of light . . . . .	11
2.2.2	Coherent Raman scattering processes . . . . .	12
2.2.3	CRS spectra and molecular response . . . . .	15
2.3	Time-resolved CRS spectroscopy . . . . .	17
<b>3</b>	<b>Time-Domain CRS Model</b>	<b>19</b>
3.1	Methane characterization and Raman spectra . . . . .	19
3.2	Modeling approach . . . . .	21
3.3	Synthetic molecular response and spectral simulation . . . . .	25
3.4	Theoretical library and fitting routine. . . . .	26
<b>4</b>	<b>Experimental Methodology</b>	<b>27</b>
4.1	Laboratory setup . . . . .	27
4.2	Experimental procedure . . . . .	29
4.3	Output and data processing . . . . .	30
<b>5</b>	<b>Results and Discussion</b>	<b>33</b>
5.1	Time-resolved CH <sub>4</sub> $\nu_2$ measurements. . . . .	33
5.2	Linewidth measurements. . . . .	37
5.3	CH <sub>4</sub> /air flame measurements . . . . .	43
<b>6</b>	<b>Conclusions and Recommendations</b>	<b>47</b>



# List of Figures

2.1	Representation of diatomic rigid rotor model for rotational motion . . . . .	4
2.2	Representation of diatomic harmonic oscillator model for vibrational motion . . . . .	5
2.3	Harmonic and anharmonic potentials with rotational and vibrational states. Wave functions are shown for vibrational levels of harmonic energy potential. For the anharmonic potential some vibrational levels are omitted and only one set of rotational levels are shown for clarity, but rotational sub-levels are present for all vibrational states. . . . .	6
2.4	Depiction of rotational energy levels $J$ imposed on vibrational levels $v$ with possible ro-vibrational transitions and respective branch labels . . . . .	9
2.5	Boltzmann population distributions for rotational (a) and vibrational (b) states of $N_2$ between 300 to 2000 K . . . . .	10
2.6	Energy level diagram for elastic and inelastic scattering processes [16] . . . . .	11
2.7	Diagram of molecular states and generation of the CARS signal [14] . . . . .	12
2.8	Diagrams of FWM processes for resonant and non-resonant CARS [20] . . . . .	13
2.9	BOXCARS configuration (left) and phase-matching condition diagram (right) [14] . . . . .	14
2.10	Overlaid profiles for Gaussian, Lorentzian, and Voigt line shapes . . . . .	16
2.11	Time-domain spectroscopy process illustrating probing of the coherence decay after time delay $\tau$ . . . . .	17
2.12	Comparison between frequency and time domain Raman spectroscopy [31] . . . . .	18
3.1	(a) Diagrams of the motion of the four fundamental vibrational modes of $CH_4$ (b) Corresponding spectra labeled for different modes across between Raman shift of 1200 to 3300 $cm^{-1}$ [43] . . . . .	20
3.2	Raman spectrum of natural gas in the range 250-2500 $cm^{-1}$ [65] . . . . .	21
3.3	$CH_4$ Raman transitions included in MeCaSDa, with polyads labeled at the top of the figure [83] . . . . .	25
3.4	SSQ optimization surface for coarse MEG library. Sum of squares values are not normalized for comparison between different library fits. . . . .	26
4.1	Diagram of the ultrabroadband two-beam CRS system. The regenerative amplifier output is split 65%-35% and fed into a second-harmonic bandwidth compressor (SHBC) and external compressor, respectively. TG, transmission gratings; S, slit; SL, spherical lens; $CL_v$ , cylindrical lenses with vertical alignment symmetry axis; TS, automated translation stage; $\lambda/2$ , half-wave plates; P, polarizer; PBS, polarization beam splitter; TF, angle-tuneable band-pass filter; BS, beam stop; B, burner. . . . .	28
4.2	Diagram of optical setup for pump/Stokes beam alignment. TS, translation stage; P, polarizer; WP, wedge plate; CL, cylindrical lens; BP, beam profiler. . . . .	29
4.3	Measurement locations across a $CH_4$ /air diffusion flame for $\tau_{pr} = 32$ ps. Acquisitions were taken at 25 locations in steps of 0.5mm. . . . .	30
4.4	General image processing for each acquired spectra shown at probe delay of $\tau = 48.3$ ps. (a) Single shot raw image captured with 1 ms exposure time. (b) Image after background subtraction and 2x2 binning. (c) Calibration spectrum containing $O_2$ and $CO_2$ Q-branch peaks used to convert x-axis pixels to wavenumber [ $cm^{-1}$ ]. (d) Resonant line spectrum after frame-averaging, normalization, and wavenumber calibration. . . . .	31
4.5	Individual processing steps conducted for probe delay $\tau = 153.3$ ps. After normalization with the NR spectrum, the baseline of the $\nu_2$ spectrum may still be offset along the y-axis. The baseline is corrected through subtracting a polynomial curve fit [86]. For acquisitions in the latter half of the probe delay scan, the intensity was scaled to match the relative magnitude of the initial half on the basis of exposure time. . . . .	32

5.1	Single-shot CH <sub>4</sub> $\nu_2$ CSRS spectrum acquired at T = 296 K and $\tau_{pr} = 28.3$ ps. Spectral branches are labeled in reverse from that of a CARS spectrum, with negative quantum number transitions ( $\Delta J = -1, -2$ for P- and O- branch, respectively) appearing at a higher frequencies. . . . .	33
5.2	Time-resolved CH <sub>4</sub> $\nu_2$ CRS spectrograms with probe pulse delay extending from $\tau_{pr} = 32$ ps to $\tau_{pr} = 85$ ps for comparison of experimental and time-domain model results. Individual spectra at each probe delay are normalized to their maximum intensity value. (a) Experimental spectrogram of the CH <sub>4</sub> $\nu_2$ mode acquired in a CH <sub>4</sub> gas flow with single-shot measurements at T = 296 K and ambient pressure. (b) Modeled spectrogram at T=296 K considering only the fundamental $\nu_2$ mode (0000 $\leftarrow$ 0100) which limits the included rotational states from J=1 to J=23 . . . . .	34
5.3	Comparison between experimental and modeled CH <sub>4</sub> $\nu_2$ Q-branch spectrograms. (a) Experimental Q-branch spectrogram acquired in room-temperature CH <sub>4</sub> flow. (b) Modeled spectrogram using 558 filtered spectral lines to model the $\nu_2$ Q-branch. . . . .	35
5.4	Spectrograms selected from the S-, R-, P-, and O-branches of the CH <sub>4</sub> $\nu_2$ spectrum comparing experimental CRS measurements with modeled ro-vibrational lines. (a) Experimental spectrogram of the convolved P(7) and O(4) lines. (b) Modeled spectrogram of the convolved P(7) and O(4) lines. (c) Experimental spectrogram of the O(8) line in the O-branch spectrum. (d) Modeled spectrogram of the O(8) line in the O-branch spectrum. (e) Experimental spectrogram of the R(5) line in the R-branch spectrum. (f) Modeled spectrogram of the R(5) line in the R-branch spectrum. (g) Experimental spectrogram of the convolved R(2) and S(0) lines. (h) Modeled spectrogram of the convolved R(2) and S(0) lines. Individual spectral lines are normalized to their own maximum intensity to better visualize their behavior. . . . .	36
5.5	Coriolis effect on the CH <sub>4</sub> $\nu_2$ vibrational mode. As a result of vibrations, the atoms of CH <sub>4</sub> are moving relative to the rotating coordinate system. Blue arrows depict the original vibrational motion, while orange arrows depict the contributions of the Coriolis effect. . .	37
5.6	Collisional dephasing of the CH <sub>4</sub> $\nu_2$ Q-branch CRS signal. Experimental $\nu_2$ CRS spectra were acquired between $\tau_{pr}=35$ and $\tau_{pr}=220$ ps for room temperature and atmospheric pressure. The Q-branch ( $\Delta J = 0$ ) peak was isolated and summed for fitting in the time-domain. MEG linewidth parameters were determined through a least-squares fitting routine with $\alpha=0.0445$ and $\beta=1.52$ . . . . .	38
5.7	Calculated transition rate matrix from $\nu_2$ Q-branch MEG fit at 296 K and 1 atm. Only rotational states from J=1 to J=23 are included as a result of the database filtering. The intensity of an element represents the rate of transition between its respective states. The total matrix is separated into two parts: an upper triangle corresponding to transitions from a higher rotational state to lower state (Equation 3.12) and a lower triangle corresponding to transitions from a lower rotational state to a higher one (Equation 3.13). . . . .	38
5.8	Evaluated sum of squares (SSQ) values across generated library entries, represented as an optimization surface as a function of the two fitting parameters $\alpha$ and $\beta$ . . . . .	39
5.9	Comparison between scaling methods for the latter half of collisional dephasing measurements of the CH <sub>4</sub> $\nu_2$ Q-branch. Up to the first 160 ps, data points with 10 ms exposure time remain the same. At 160 ps the differences between the scaling methods and the original intensity are observable. . . . .	40
5.10	Probe delay scans of the CH <sub>4</sub> $\nu_2$ Q-branch for varying CH <sub>4</sub> -gas mixtures at T = 296 K and atmospheric pressure. Three different colliding partners N <sub>2</sub> , Ar, and H <sub>2</sub> are mixed with CH <sub>4</sub> for 25% and 50% of the gas flow. All measurements are normalized to their intensity at $\tau_{pr}$ for comparison of their time-domain beating behavior. . . . .	41
5.11	Separated probe delay scans for CH <sub>4</sub> $\nu_2$ Q-branch under gas mixtures with N <sub>2</sub> , Ar, and H <sub>2</sub> . The same pure CH <sub>4</sub> probe delay scan is shown in each sub-figure for comparison. The extent of the measured dephasing timescale is different for each case due to the rate of decay in signal intensity for each mixtures. (a) Collisional dephasing for 75%/25% and 50%/50% gas mixtures of CH <sub>4</sub> -N <sub>2</sub> , respectively. (b) Collisional dephasing for 75%/25% and 50%/50% gas mixtures of CH <sub>4</sub> -Ar. (c) Collisional dephasing for 75%/25% and 50%/50% gas mixtures of CH <sub>4</sub> -H <sub>2</sub> . . . . .	42

- 
- 5.12 Collisionally induced rotational energy transfer process between a radiator  $\text{CH}_4$  and different perturbers  $\text{CH}_4$  and  $\text{H}_2$ . With more adjacent states between the radiator and perturber, the energy transfer process is more likely. . . . . 43
- 5.13 CRS spectra acquired across a laminar  $\text{CH}_4$ /air diffusion flame. Three labeled slices of the spatially resolved measurements are shown with greater detail in Figure 5.14. All spectra were acquired with a probe delay of  $\tau_{pr}$ . Because of the overwhelming intensity of the  $\text{O}_2$  Q-branch, it was necessary to compress the color-scale (Gamma compression) during post-processing to reveal other spectral features. . . . . 44
- 5.14 Three spectral slices in the molecular fingerprint region containing the  $\text{CH}_4$   $\nu_2$  mode. Each spectrum is acquired at a different location in the flame. (a) Fuel flow at burner center ( $y=1$  mm) containing the full spectrum of  $\text{CH}_4$   $\nu_2$  and ro-vibrational peaks of  $\text{CO}_2$ . (b) Reaction zone ( $y=8.5$  mm) where several species such as  $\text{H}_2$ ,  $\text{O}_2$ , and  $\text{CO}_2$  are present, with a vast range of intensities indicating increased temperature. (c) Oxidizer flow ( $y=11.5$  mm) displaying spectral branches of both  $\text{O}_2$  and  $\text{CO}_2$ . . . . . 45

# List of Tables

3.1	CH <sub>4</sub> fundamental vibrational frequencies, symmetry, and degeneracy [41, 42] . . . . .	19
5.1	Point group T <sub>d</sub> irreducible representations and associated spatial dimensions and degeneracy. . . . .	41



# Introduction

## 1.1. Background

The most omnipresent issue today is the onset of anthropogenic climate change and its catastrophic effects on our environment. In 2017, human-induced warming of global mean temperature reached approximately 1°C above pre-industrial levels. If global warming continues increasing at the current rate, this temperature will likely reach 1.5°C between 2030 and 2052 [1]. While warming beyond 1.5°C is not unavoidable, its development is dependent on current and future reduction of greenhouse gas (GHG) emissions.

Aviation is estimated to contribute between 3.5 and 4.9% of total anthropogenic radiative forcing (RF) and is expected to increase by a factor of 3 to 4 by 2050 [2]. The largest amount of aviation emissions - such as CO<sub>2</sub>, H<sub>2</sub>O, and NO<sub>x</sub> gases - are produced at cruise altitudes of 8 to 12 km which increases the impact of their climate forcing effects. Furthermore, aviation is uniquely reliant on combustion due to the energy density of jet fuel and the lack of viable alternative energy sources for propulsion. In addition, air quality and human health are affected, with an estimated 16000 early deaths occurring each year due to air pollutant exposure [3]. While the aviation industry has struggled over the course of the global pandemic, the overall increase of air traffic demand will likely continue. From 1992 to 2005, aviation passenger transport in terms of revenue passenger kilometer (RPK) increased at an average rate of 5.2% per year despite multiple world crises in the same period [2]. In response to this trend, many institutions have prepared initiatives to reduce the aviation impact on climate change.

The International Civil Aviation Organization (ICAO) has begun to implement the Carbon Offsetting and Reduction Scheme for International Aviation, or CORSIA, with the goal of carbon-neutral growth of international aviation relative to 2020 levels through market-based carbon offset measures [4]. The measures include improvements in technology and operations, as well as increasing adoption of sustainable jet fuels [5]. Likewise, the International Air Transport Association (IATA), an aviation trade association whose members carry 82% of the world's air traffic, has three main targets for its own air transport emissions mitigation. The targets are an average improvement in fuel efficiency, carbon-neutral growth, and net-zero carbon emissions by 2050 [6].

To accomplish goals like those set by ICAO and IATA, the aviation industry must reduce fuel consumption through operational improvements and aircraft design while introducing alternative fuels to reduce the amount of GHG emissions per unit of fuel consumption [7]. The implementation of new technologies within aviation takes time and the benefits are not necessarily immediately realized, although short-term improvements can be gained from air traffic management and alternative fuels [8]. Regardless of the approach, the fundamental source of aviation emissions is the aircraft engine combustion process.

Combustion is a major source of global energy production and used in industrial processes, power generation, and transportation. Research into the combustion process has primarily focused on fuel efficiency but has developed to include air quality and environmental concerns as well. The design process for combustors is heavily reliant on computational modeling and numerical simulations for

many reasons, including faster analysis of systems, the high cost of lab and field testing, and safety precautions. However, combustion modeling is challenging due to the coupling between fluid dynamics and chemical kinetics which influences the species concentrations, reaction progress, and pollutant formation and emission. To ensure that combustion simulation results are both robust and accurate, it is vital to validate models through comparison with experimental data [9].

In aircraft engines, the gas turbine combustor is the main component responsible for fuel efficiency and emissions production. The combustion chamber is a turbulent multi-phase flow environment that operates under conditions of high pressure and temperature, making acquisition of experimental data difficult. Additionally, physical probes are limited in their temporal and spatial resolution and disrupt the flow-field of the flames they are measuring [10]. Luckily, the advancement of laser diagnostic techniques and their capabilities has expanded the possibilities of measurement acquisition in combustion research.

Laser diagnostics have proven to be invaluable measurement tools in combustion research over the past few decades of their development. With these techniques, laser light sources are used to probe the molecules in gas-phase reacting flows and acquire non-intrusive, in-situ measurements that overcome the drawbacks of physical probes [10]. Additionally, the techniques can measure temperature, velocity, and species concentrations with very high temporal and spatial resolution [11, 12]. Applications to foundational combustion studies have been outlined in previous articles, with emphasis on the iterative process between laser diagnostics and computational models for the purpose of optimizing and controlling combustion processes [13].

## 1.2. Motivation and outline

Laser diagnostics have been applied to a variety of relevant fuels and gases in combustion and methane is no exception. It is a major natural gas component and used in many chemical processes. When directly released into the environment methane is an influential greenhouse gas, however, as fuel methane performs better than heavier hydrocarbons and coal. Therefore, the ability to quantitatively detect temperature and concentration of methane molecules with high resolution in reactive systems is significant.

One powerful diagnostic technique is coherent Raman scattering (CRS), which can achieve measurements with very high precision and accuracy in gas-phase reacting flows. The advantages of the method over other spectroscopic techniques are its spectral selectivity, directional coherent signal, and micrometer spatial resolution [14]. State-of-the-art CRS techniques are based on the use of ultra-short femtosecond (fs) or picosecond (ps) laser pulses which can measure the time-domain evolution of the ro-vibrational motion of the target molecules.

In-situ detection of methane and its use as a probe molecule has progressed in the past several decades, including applications of CRS techniques. Methane has four fundamental Raman-active vibrational modes, for which the  $\nu_1$  mode consisting of a symmetric CH stretch has been extensively characterized. While much of the focus has been on the  $\text{CH}_4$   $\nu_1$  Q-branch, the  $\nu_2$  mode comprised of a H-C-H bending vibration lies within a suitable region for natural gas diagnostics. For this thesis, the goal is to develop hybrid fs/ps CRS spectroscopy for the Raman-active  $\text{CH}_4$   $\nu_2$  vibrational mode. To this end, it is necessary to acquire measurements of the time-domain response of the  $\text{CH}_4$   $\nu_2$  mode and model its collisional dephasing.

The thesis report is sectioned into six parts. After the introduction (Chapter 1), the necessary theoretical background of molecular spectra, the CRS process, and time-resolved CRS spectroscopy will be established in Chapter 2. Subsequently, the modeling approach towards the  $\nu_2$  mode of methane and simulation of its molecular response will be discussed in Chapter 3. In Chapter 4 the experimental methodology implemented in the thesis is presented, including the laboratory setup, procedure, and processing of the output. Next, the results of the experimental campaign will be presented and discussed in Chapter 5. Finally, Chapter 6 will conclude the findings from the thesis research and suggest future improvements.

# 2

## Theoretical Background

Optical and laser diagnostics involve the scattering, absorption, and emission of light and interaction with the molecules of interest. The structure of a molecule determines how it interacts with electromagnetic radiation. Additionally, a molecule's structure will affect its spectrum, or the absorption, emission, or scattered intensity across the continuum of electromagnetic wavelengths. Therefore, fundamental understanding of molecular structure and the spectroscopy methods involved is necessary for the analysis of experimental spectra and the aims of the project. This chapter provides an overview of the theory related to molecular physics and spectra, the fundamentals of the CRS process, and the specifics of time-resolved CRS spectroscopy.

### 2.1. Molecular structure and spectra

To interpret and analyze spectra, the corresponding molecular structure from which it is obtained must first be understood. Consequently, a description of the quantized molecular energy levels is necessary. This section of the theoretical background will present the related quantum physics including characterization of molecular energy levels, selection rules and allowed system transitions, and the population distribution amongst energy levels. The preliminary theory will be focused on diatomic molecules for simplicity, with additional information for polyatomic methane when relevant.

#### 2.1.1. Molecular energy states

A molecule's structure and its energy are directly related to the spectra it produces when absorbing, emitting, or scattering electromagnetic radiation and are therefore relevant to understand for spectroscopy. Molecules are systems with discrete values of internal energy whose quantized energy spectra are characteristic for specific species. With the Born-Oppenheimer approximation, which assumes separable electronic and nuclear motion in molecules based on relative size and velocity, the internal energy of a molecule can be written as follows:

$$E = E_e + E_v + E_j \quad (2.1)$$

As seen in Equation 2.1, the internal energy is composed of three contributions – electronic ( $E_e$ ), vibrational ( $E_v$ ), and rotational ( $E_j$ ) energy. The relative magnitude of each energy is  $E_e > E_v > E_j$ , with multiple rotational states existing in a vibrational state and multiple vibrational states existing within an electronic state. The rotational and vibrational motion and energy levels of diatomic and polyatomic molecules will be discussed in this sub-section, as they are of primary concern to the thesis. Explanations of electronic structure is entrusted to other resources such as [15].

##### 2.1.1.1 Rotational motion and energy levels

The rotational motion of a diatomic molecule can be described as a system consisting of two point-masses connected by a massless, rigid rod which can rotate end-over-end, termed the rigid rotor approximation. A depiction of the model can be seen in Figure 2.1, where  $m_1$  and  $m_2$  are the point-mass

representations of nuclei and  $r$  is the internuclear distance. The system's moment of inertia, with respect to its center of mass, is  $I = \mu r^2$  with the reduced mass  $\mu = \frac{m_1 m_2}{m_1 + m_2}$  and the previously mentioned internuclear distance  $r$ .

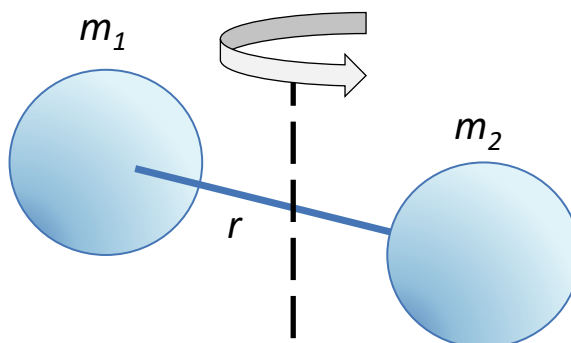


Figure 2.1: Representation of diatomic rigid rotor model for rotational motion

For a rigid rotor, the rotational energy of the system in classical mechanics is  $E_J = \frac{1}{2}I\omega^2$ , where  $I$  is the system's moment of inertia and  $\omega$  is the angular velocity. The expression for rotational energy can also be written in terms of the system's angular momentum,  $P = I\omega$ , which when substituted, results in the expression:  $E_J = \frac{P^2}{2I}$ .

The fundamental motion of the molecule is described by the Schrödinger equation, given as:

$$\hat{H}\psi = E\psi \quad (2.2)$$

in its time-independent form in terms of the Hamiltonian operator  $\hat{H}$ , the energy of the system  $E$ , and wave function  $\psi$  representing the probability amplitude of a quantum system (e.g. subatomic particle) to occupy one specific state amongst those possible. Additionally, the actual probability of finding the particle is given by the product of the wave function with its complex conjugate  $\psi \times \psi^*$ . If the Schrödinger equation is solved for the rigid rotor, the rotational energy becomes discretized and is represented by:  $E_J = \frac{h^2}{8\pi^2 I} J(J+1)$  where  $h$  is Planck's constant and  $J$  is the rotational quantum number which can assume positive integer values [15].

The rotational energy equation can also be written in its term value form, which is the wave mechanic form divided by Planck's constant  $h$  and the velocity of light  $c$ , as seen with Equation 2.3. By doing this, the term values are measured by  $cm^{-1}$ , or wavenumber, which is easier to use in the context of molecular spectroscopy.

$$F(J) = \frac{E_J}{hc} = BJ(J+1) \quad (2.3)$$

The term  $B$ , known as the rotational constant, is inversely proportional to the molecule's moment of inertia  $I$  and is defined as:

$$B = \frac{h}{8\pi^2 c I} \quad (2.4)$$

For realistic applications, the rigid rotor model must be corrected for real molecules. Two areas for further model refinement are centrifugal stretching and the dependence of the rotational constant on the vibrational state [14]. When a real molecule is rotating, it experiences a centrifugal force which affects its internuclear distance. To account for this effect, the initial equation given for rotational term values can be modified via a Taylor expansion of the  $J(J+1)$  term to obtain:  $F(J) = BJ(J+1) - DJ^2(J+1)^2 + \dots$ , which is truncated to the second order. For this expression,  $B$  is the previously defined rotational constant and  $D$  is a centrifugal correction term approximated as  $D = \frac{4B^3}{\omega^2}$ .

After incorporating the effect of centrifugal force, the dependence on the molecule's vibrational state is considered. The rotational and vibrational motions of a molecule happen simultaneously, resulting in a continuously changing internuclear distance  $r$  and moment of inertia  $I$ . Therefore, the rotational constant  $B$  and centrifugal constant  $D$  will be different for a given vibrational level  $v$  compared to the equilibrium position.

$$B_v = B_e - \alpha_e \left( v + \frac{1}{2} \right) + \dots \quad (2.5)$$

$$D_v = D_e - \beta_e \left( v + \frac{1}{2} \right) + \dots \quad (2.6)$$

The vibrational level-dependent terms, with subscript  $v$ , can be defined using the equilibrium terms  $B_e$  and  $D_e$  with rotational-vibrational interaction constants  $\alpha_e$  and  $\beta_e$ . With these modifications accounted for, the expression for rotational term values becomes:

$$F_v(J) = B_v J(J + 1) - D_v J^2(J + 1)^2 + \dots \quad (2.7)$$

### 2.1.1.2 Vibrational motion and energy levels

A diatomic molecule's vibrations can be modeled as a harmonic oscillator, a system with a point-mass under a restoring force that is proportional to the mass' displacement  $x$  from equilibrium. Like the rigid rotor, the nuclei are represented by two point-masses, but instead of a rigid rod they are connected by a spring as shown in Figure 2.2.

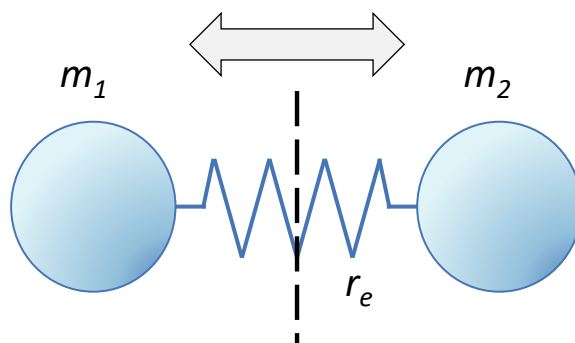


Figure 2.2: Representation of diatomic harmonic oscillator model for vibrational motion

For this system, the potential energy is expressed in terms of the equilibrium internuclear distance  $r_e$ :

$$E_v = \frac{1}{2} k (r - r_e)^2 = \frac{1}{2} k x^2 \quad (2.8)$$

where  $x$  is the displacement distance from equilibrium and  $k$  is the spring or force constant. The value of  $k$  can be defined in terms of the molecule's oscillation frequency  $\nu_{osc}$  and expressed as:

$$k = 4\pi^2 \mu \nu_{osc}^2 \quad (2.9)$$

When the potential energy expression is substituted in the Schrödinger equation, the quantized harmonic oscillator energy levels are defined by the equation below, with the vibrational quantum number  $v$  taking positive integer values [15].

$$E_v = h\nu_{osc} \left( v + \frac{1}{2} \right) \quad (2.10)$$

The term value arrangement for the vibrational energy can be seen in Equation 2.11:

$$G(v) = \frac{E_v}{hc} = \omega \left( v + \frac{1}{2} \right) \quad (2.11)$$

where the vibrational frequency  $\omega = \nu_{osc}/c$  and is measured by wavenumber units of  $\text{cm}^{-1}$ .

Like the initial rotational energy model, the harmonic oscillator model for vibrational motion is idealized. If the potential energy defined in Equation 2.8 is plotted as a function of the internuclear distance, the outcome will be a parabolic potential energy curve with equally spaced energy states. The minimum energy of a potential curve for a particular electronic state defines the equilibrium internuclear distance with a zero-point, or ground state, energy  $\hbar\omega/2$  above the minimum. While the model is valid at the bottom of the potential and close to the equilibrium inter-nuclear distance, real molecules behave as anharmonic oscillators. To approximate the entire potential function for an anharmonic oscillator, the empirical Morse potential function is used:

$$E_v = D_e [1 - e^{\beta(r-r_e)}]^2 \quad (2.12)$$

where  $D_e$  is the dissociation energy and the parameter  $\beta$  is given by  $\beta = \sqrt{\frac{2\pi^2 c \mu}{D_e \hbar}} \omega_e$ . In Figure 2.3, the potential curves for each model are overlaid for comparison. The vibrational term-values for the Morse potential are obtained from substituting the potential energy in the wave equation, resulting in the expression:

$$G(v) = \omega_e \left( v + \frac{1}{2} \right) - \omega_e x_e \left( v + \frac{1}{2} \right)^2 + \omega_e y_e \left( v + \frac{1}{2} \right)^3 + \dots \quad (2.13)$$

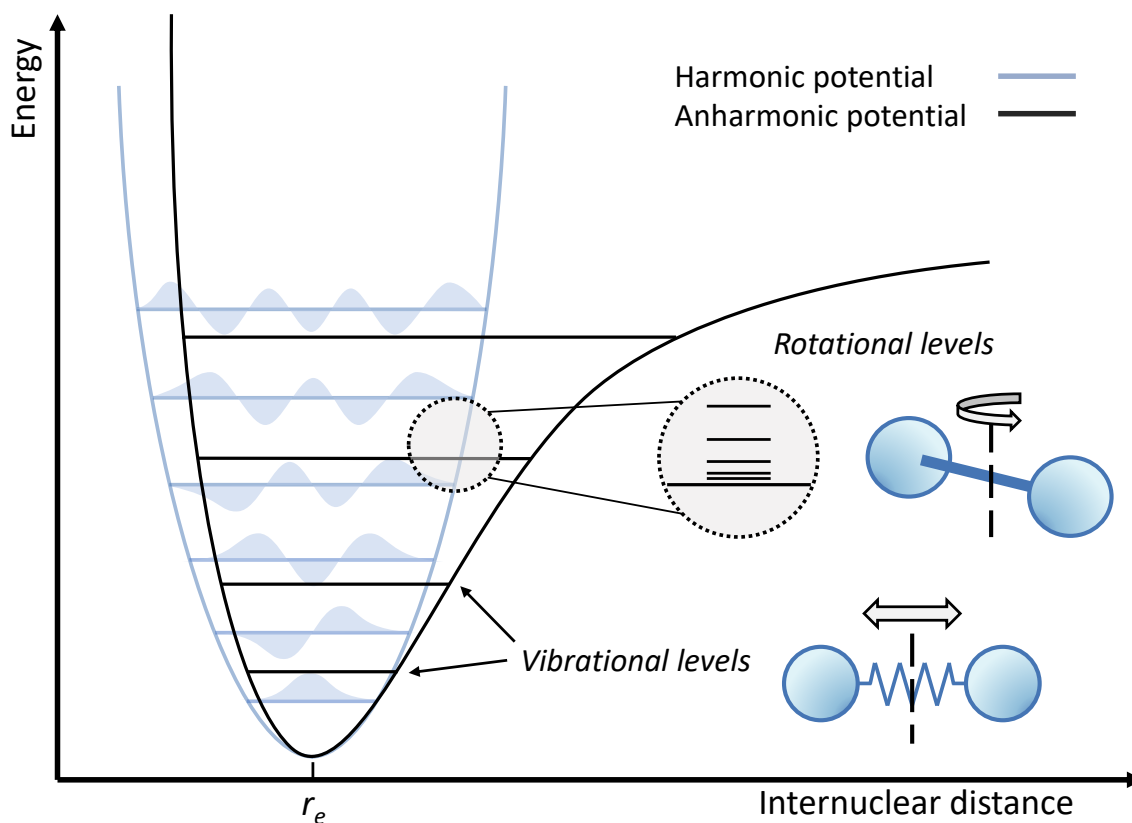


Figure 2.3: Harmonic and anharmonic potentials with rotational and vibrational states. Wave functions are shown for vibrational levels of harmonic energy potential. For the anharmonic potential some vibrational levels are omitted and only one set of rotational levels are shown for clarity, but rotational sub-levels are present for all vibrational states.

### 2.1.2. Energy level transitions and selection rules

In the previous section, the possible energy levels of a molecule – rotational, vibrational, and electronic – were detailed. However, not all energy level transitions will occur when a photon and a molecule

interact. Transitions that obey certain requirements, or selection rules, are called allowed transitions while those that do not are designated as forbidden transitions. For transition notation, the upper state is commonly listed first. An arrow may be added, such as  $A \rightarrow B$  or  $A \leftarrow B$ , to clarify whether the observed transition is emission or absorption.

Selection rules filter the transitions that can occur in principle and exist for rotational, vibrational, and electronic levels. The probability of a transition is based on the value of the transition moment  $R$ , shown in Equation 2.14:

$$R = \int \psi' \mu \psi'' d\tau \quad (2.14)$$

where  $\mu$  is the transition moment operator and  $\psi'$  and  $\psi''$  are the wave functions of the upper and lower states, respectively. If the moment has a non-zero value, the transition is allowed and if it is zero then the transition is forbidden. The probability or intensity of the transition is proportional to the square of the magnitude of the transition moment  $|R|^2$ . In addition, the value of the moment is dependent on the quantum numbers characterizing the wave functions of the states [15].

Due to the Born-Oppenheimer approximation and the consequent separability of energy contributions, there are separate selection rules for the electronic, vibrational, and rotational levels. Furthermore, the applicable selection rules are dependent on the symmetry of the molecule. A molecule may have one or more elements of symmetry that correspond to symmetry operations of reflection or rotation. While a linear molecule has an infinite number of symmetry elements, nonlinear molecules are typically constrained by a finite combination of symmetry elements termed point groups [15]. Polyatomic molecules are characterized by their three principal moments of inertia ( $I_A, I_B$ , and  $I_C$ ), whose axes pass through the center of mass and are mutually perpendicular. The relative magnitudes of the principal moments of inertia are the basis for polyatomic classification, leading to groups of linear ( $I_A \approx 0, I_B = I_C$ ), symmetric top ( $I_A \neq I_B = I_C$ ), spherical top ( $I_A = I_B = I_C$ ), and asymmetric rotor ( $I_A \neq I_B \neq I_C$ ) molecules.

Methane is classified as a spherical top molecule with three equal principal moments of inertia. This thesis is focused on the analysis of the methane ro-vibrational spectra. Therefore, electronic selection rules will not be detailed here. The rotational and vibrational selection rules will be elaborated on for diatomic molecules first, then extended to the polyatomic  $\text{CH}_4$ .

### 2.1.2.1 Rotational selection rules

The spectrum and transitions of interest are that of Raman scattering, a process which will be discussed with further detail in upcoming sections. The molecular property of most importance in scattering is the polarizability  $\alpha$ , which is a measure of how much the electric dipole of a molecule can be distorted by application of an external electromagnetic field. For pure rotational spectroscopy the gross selection rule is that the molecule must be anisotropically polarizable, where its properties are different dependent on direction [16]. Rotational energy levels of a molecule can be characterized by the rotational quantum number  $J$ , as previously mentioned. The specific selection rule for diatomic rotational Raman scattering is:

$$\Delta J = \pm 2$$

Since Raman spectroscopy mainly uses lasers as incident radiation for scattering, it is useful to define the Raman wavenumber displacement as  $\Delta\Omega = \Omega - \Omega_L$ , where  $\Omega_L$  is the exciting radiation wavenumber. The form of the rotational Raman spectrum can be predicted by applying the selection rule to the rotational energy levels, as shown below:

$$\Delta F = F(J + 2) - F(J) = \Delta\Omega$$

For spontaneous Raman scattering, the transition wavenumber can be found for Stokes transitions ( $\Delta J = +2$ ) and anti-Stokes transitions ( $\Delta J = -2$ ) through the expressions:

$$\Delta\Omega_S = -2B(2J + 3) \quad (2.15)$$

$$\Delta\Omega_{AS} = 2B(2J - 1) \quad (2.16)$$

The context for why there are two possible transition outcomes will be expanded upon later. When extending the expected spectra and selection rules to methane, the polarizability of the molecule must be examined.

### 2.1.2.2 Vibrational selection rules

For vibrational motion, the energy levels are indicated by the vibrational quantum number  $v$ . The gross selection rule for pure vibrational spectroscopy is that a molecule's polarizability must change during its vibration. The vibrational Raman transition moment is evaluated with the molecule polarizability  $\alpha$  to find the specific harmonic selection rule:

$$\Delta v = \pm 1$$

which holds for both homonuclear and heteronuclear diatomic molecules. When anharmonicity is incorporated the vibrational term values and wave functions are modified and the vibration wavenumber  $\omega_e$  cannot be directly measured [16]. One effect is the modification of the specific selection rule to:

$$\Delta v = \pm 1, \pm 2, \pm 3, \dots$$

to include weaker overtone transitions of  $\Delta v = \pm 2, \pm 3, \dots$  alongside the main  $\Delta v = \pm 1$  transition. In addition, wavenumbers for fundamental, overtones, and hot band transitions are given by [16]:

$$v = 1 \leftarrow v = 0 : \quad \Delta\Omega_{\text{fundamental}} = \tilde{\omega}_e(1 - 2\chi_e) \quad (2.17)$$

$$v = 2 \leftarrow v = 0 : \quad \Delta\Omega_{\text{overtone}} = 2\tilde{\omega}_e(1 - 3\chi_e) \quad (2.18)$$

$$v = 2 \leftarrow v = 1 : \quad \Delta\Omega_{\text{hot}} = \tilde{\omega}_e(1 - 4\chi_e) \quad (2.19)$$

where  $\tilde{\omega}_e$  is the equilibrium vibrational frequency in wavenumbers and  $\chi_e$  is the anharmonicity constant. Although all the possible transitions have been listed, mainly fundamental transitions are present in a Raman spectrum for diatomic molecules at room temperature. However, at high temperature hot bands can become even more prominent than the fundamental bands.

With a nonlinear N-atomic molecule there will be  $3N - 6$  vibrational modes, where all nuclei are in harmonic motion with the same oscillation frequency [16]. Through application, it follows that the  $\text{CH}_4$  molecule will have nine vibrational modes. In an approximation analogous to diatomic molecules polyatomic vibrations can be treated as harmonic oscillators, called the polyad approximation. If two or more different states of a molecule are measured to have the same energy value, then are considered degenerate.

For each normal vibration  $i$ , the non-degenerate vibrational term values  $G(v_i)$  are defined using the classical vibration wavenumber  $\omega_i$  and the vibrational quantum number  $v_i$  in the following expression:

$$G(v_i) = \omega_i \left( v_i + \frac{1}{2} \right) \quad (2.20)$$

For vibrations with a degree of degeneracy, the term value expression incorporates the degeneracy  $d_i$  and becomes:

$$G(v_i) = \omega_i \left( v_i + \frac{d_i}{2} \right) \quad (2.21)$$

Furthermore, the polyatomic general selection rule is the same as that for diatomic molecules, where the vibrational transitions follow:

$$\Delta v_i = \pm 1$$

For vibrational transitions to be allowed in the Raman spectrum, the induced dipole moment of the molecule must have a change of amplitude that requires further symmetry-dependent selection rules. While the application of group theory to methane will not be detailed here, more information about the procedure can be found in literature such as [17].

### 2.1.2.3 Rotation-vibration selection rules

In previous sections, the idea of lower-energy rotational sub-levels associated with vibrational energy levels was introduced. Unlike pure rotational or vibrational spectroscopy, rotation-vibration, or ro-vibrational, spectroscopy observes transitions between the rotational energy levels of two different

vibrational levels. For diatomic molecules, the rotational selection rule for ro-vibrational transitions is given by [16]:

$$\Delta J = 0, \pm 2$$

This rule results in three possible branches when a molecule transitions between two vibrational levels: the Q branch, O branch, and S branch. In the Q branch, the transition between the vibrational levels occurs without any rotational change ( $\Delta J = 0$ ). In the O and S branches the rotational change is ( $\Delta J = -2$ ) or ( $\Delta J = +2$ ), respectively. In Figure 2.4, the three branches can be seen and compared to one another. While not relevant to the selection rule at hand, the P and R branches with rotational change of ( $\Delta J = -1$ ) or ( $\Delta J = +1$ ), respectively, are included for context.

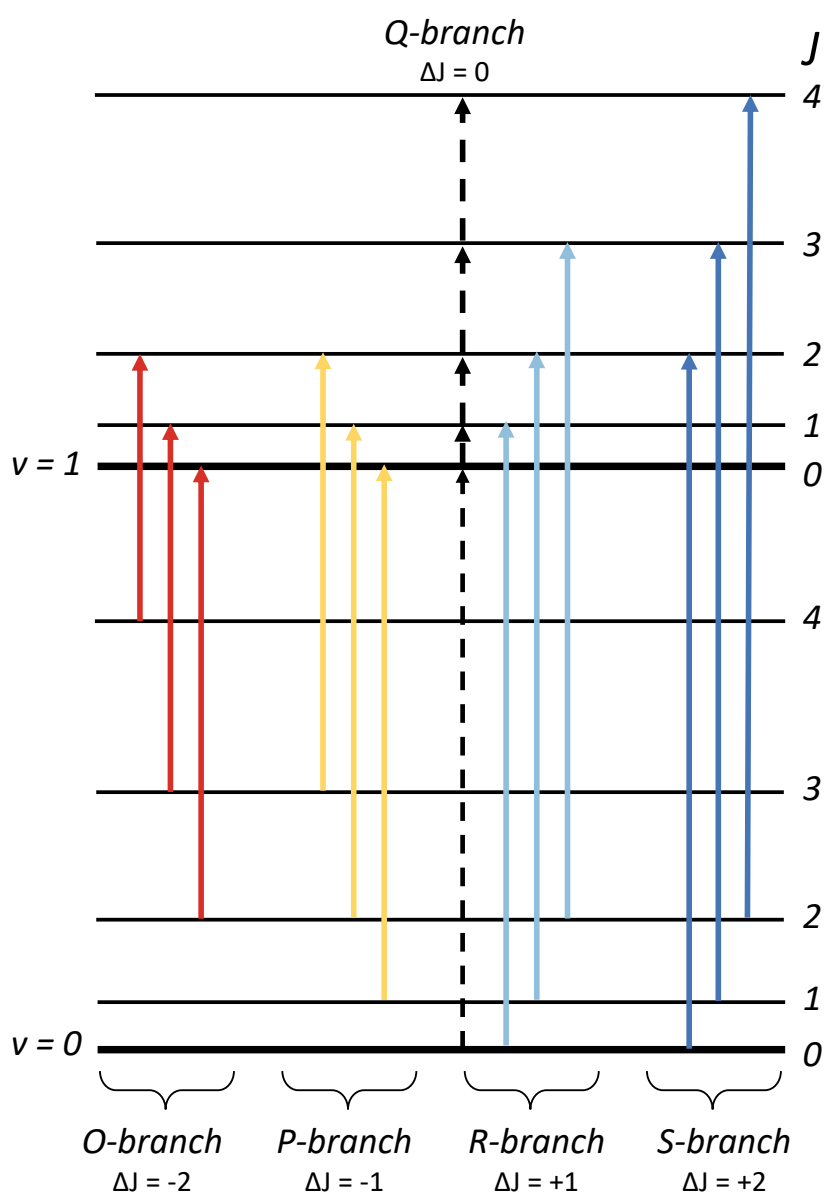


Figure 2.4: Depiction of rotational energy levels  $J$  imposed on vibrational levels  $v$  with possible ro-vibrational transitions and respective branch labels

If it is assumed that  $B_1 = B_0 = B$ , then the transition wavenumbers of the O, Q, and S branches are:

$$\Delta\Omega_O = \omega_0 - 4BJ + 2B \quad (2.22)$$

$$\Delta\Omega_Q = \omega_0 \quad (2.23)$$

$$\Delta\Omega_S = \omega_0 + 4BJ + 2B \quad (2.24)$$

where  $\omega_0$  is the separation of the vibrational levels in wavenumber. The approach to polyatomic molecules is similar to that for diatomic molecules. The resulting term values  $S$  of such transitions are the sum of the rotational and vibrational term values, where  $i$  is for a particular vibration:

$$S = F_{v_i} + G(v_i) \quad (2.25)$$

### 2.1.3. Population distribution

While transition selection rules determine the spacing of lines in a spectrum, the strength of the spectral lines is dependent on the transition probability. Equation 2.14 describes a microscopic transition probability, where only the probability of a single molecule transiting between states is considered. For macroscopic ensemble of molecules, the microscopic probability is incorporated into statistical descriptions such as the Boltzmann distribution to predict the average number of molecules per ro-vibrational state. If the system is in thermal equilibrium, the population of energy states will have a certain probability. In addition, higher molecular energy states are populated at higher temperatures. For a particular energy state  $m$ , the fraction of molecules in that state as a function of temperature  $T$  is found by:

$$\rho_m = \frac{N_m}{N_{tot}} = \frac{g_j g_m \exp\left[-\frac{E_m}{k_B T}\right]}{Z(T)} \quad \text{where} \quad Z(T) = \sum_m g_m \exp\left[-\frac{E_m}{k_B T}\right] \quad (2.26)$$

where  $E_m$  is the energy of the state,  $k_B$  is the Boltzmann constant,  $N_m$  is the number density of state  $m$ ,  $N_{tot}$  is the total number density of the chemical species,  $g_j$  is spin degeneracy,  $g_m$  is the degeneracy of the rotational state, and  $Z(T)$  is the partition function which can be factorized into electronic, vibrational, and rotational components. The partition function is the sum of the population in all possible states and serves as a normalizing factor for the Boltzmann distribution. In Figure 2.5, the fractional population distribution for molecular nitrogen is shown for rotational and vibrational states across a range of temperatures. In the figure, the Boltzmann population is distributed among lower rotational quantum numbers for lower temperatures. Additionally, nearly all molecules reside in the first vibrational state. As the temperature rises, higher quantum levels for both rotational and vibrational states become increasingly populated.

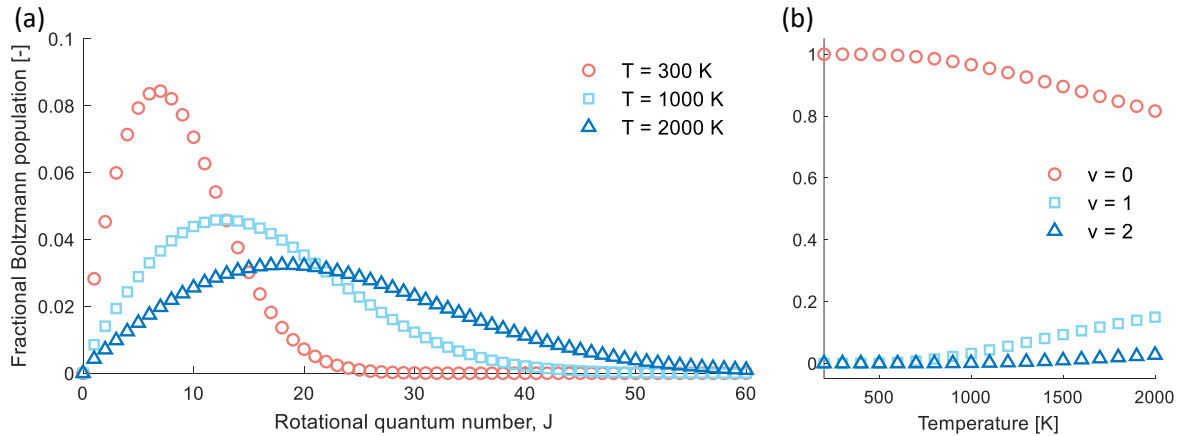


Figure 2.5: Boltzmann population distributions for rotational (a) and vibrational (b) states of  $N_2$  between 300 to 2000 K

When considering a transition between an upper energy state  $f$  and lower energy state  $i$ , the population ratio between them can be given by the Boltzmann distribution law:

$$\frac{\rho_f}{\rho_i} = \frac{N_f}{N_i} = \frac{g_f}{g_i} \exp\left[-\frac{\Delta E_{fi}}{k_B T}\right] \quad (2.27)$$

For spontaneous emission, Raman scattering, and incoherent optical processes in general, the intensity of a transition can be evaluated using the transition probability  $A_{fi}$ , Planck's constant  $h$ , the transition

frequency  $\nu$ , and the initial state population  $N_i$  using Equation 2.28.

$$I_{fi} = A_{fi} N_i h \nu \quad (2.28)$$

In upcoming sections, descriptions will be provided for the intensity of coherent scattering which is mainly differentiated by scaling with the square of the number density  $N^2$  instead of scaling linearly like in Equation 2.28. Through these expressions, the spectral line intensities of an atom or molecule can be predicted. Conversely, the application of the Boltzmann distribution allows for thermometry of a chemical species using the information of its populated states. Excluding the effect of other terms included in  $A_{fi}$ , the acquired intensity spectrum of a molecule represents the thermal Boltzmann distribution of its rotational and vibrational populations. Due to this, CRS is regarded as a very effective thermometric technique.

## 2.2. Fundamentals of coherent Raman scattering

With the theory related to molecular physics and spectra covered, the fundamentals of coherent Raman scattering, or CRS, needs to be described. This diagnostic technique is relevant to the thesis as the main method to obtain methane spectra and characterize its bending mode. In this section, the light scattering, the theory underlying the CRS process, and factors affecting the molecular response will be presented.

### 2.2.1. Scattering of light

Even if a photon incident on a molecule does not result in absorption, it can still interact with the molecule through either stimulated emission or a process called scattering. Scattering can be thought of as a collision between a photon and a molecule that excites the molecule to a virtual state, which immediately relaxes and emits another photon. If the energy of the molecule and emitted photon is unchanged, the process is called elastic Rayleigh scattering. In the case of inelastic Raman scattering, the emitted photon is changed through a loss or gain of energy, or Stokes or anti-Stokes, respectively.

In Stokes scattering, the molecule relaxes to a higher state than its initial state, while anti-Stokes scattering results in a molecule relaxing to a state lower than its initial state. The difference in energy of the photon before and after its scattering is called a Raman shift. When observed experimentally, the Stokes scattered intensity is greater than the anti-Stokes scattered intensity. This difference is due to the Boltzmann statistics that demonstrate that the excited states will be less populated than the ground state at thermal equilibrium. In Figure 2.6, a diagram is provided for comparison of elastic and inelastic scattering processes with virtual energy states  $\nu_0$  and  $\nu_1$ .

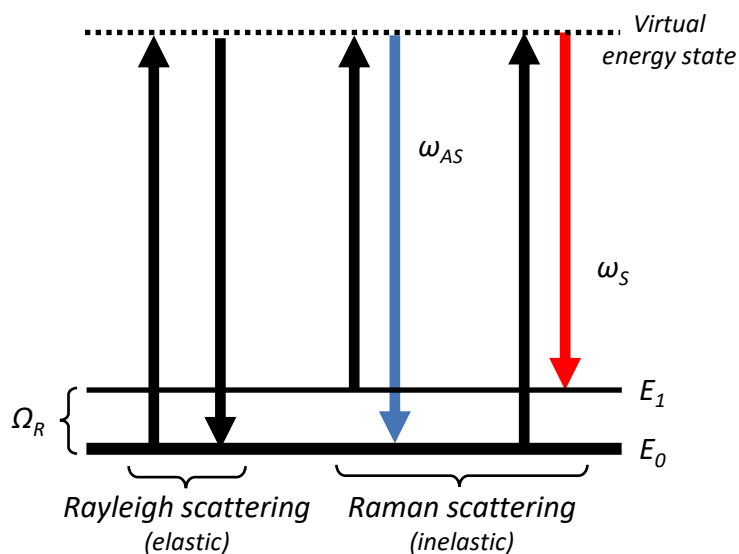


Figure 2.6: Energy level diagram for elastic and inelastic scattering processes [16]

Scattering can be distinguished from other photophysical processes such as stimulated absorption and emission, as well as spontaneous emission, because the molecule is excited to a virtual state instead of an observable state. In addition, the probabilities of each type of scattering vary widely. Rayleigh scattering is the most dominant process, with Raman scattering several orders of magnitude less likely to occur. Despite these rare occurrences, the process can be coupled to a laser to achieve higher signal intensity and probe otherwise inaccessible molecules in the visible spectral region.

### 2.2.2. Coherent Raman scattering processes

Coherent Raman scattering is a resonant, coherent technique used to obtain spectroscopic information on Raman-active molecules with a considerably higher efficiency than spontaneous Raman scattering. The four-wave mixing (FWM) process utilizes the third-order nonlinear interaction of two lasers to excite a molecule that is then probed by a third laser to generate a fourth, coherent signal. This process can be implemented in both its Stokes and anti-Stokes forms, respectively CSRS and CARS, whose spectra are identically dependent on molecular parameters. There is a general preference for the CARS technique due to the convenience of producing its probe beam and fluorescence rejection, resulting in more extensive experimental use than CSRS. Therefore, the process explanation will primarily be in reference to CARS, however, it is also applicable to CSRS. A diagram visualizing the CARS process is presented in Figure 2.7.

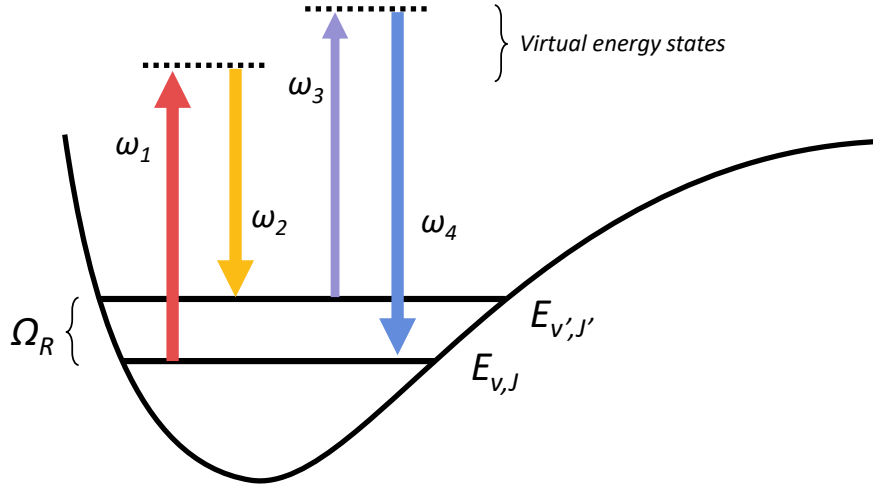


Figure 2.7: Diagram of molecular states and generation of the CARS signal [14]

The first two beams, called the pump ( $\omega_1$ ) and Stokes ( $\omega_2$ ), interfere with each other and create a beating frequency ( $\omega = \omega_1 - \omega_2$ ) which can be set to coincide with a ro-vibrational transition in the molecule ( $\omega = \Omega_R$ ), resulting in an induced Raman coherence. A third beam termed the probe ( $\omega_3$ ) interacts with the excited molecules in a coherent ro-vibrational state via Raman scattering, which generates a fourth signal at the anti-Stokes frequency such that:

$$\omega_4 = \omega_1 - \omega_2 + \omega_3 \quad (2.29)$$

The fourth signal is then sent to a spectrometer and the spectrum is acquired by a sensor or camera. The process is distinctly nonlinear in contrast to the previously named processes (i.e. Rayleigh and Raman scattering, absorption, and spontaneous and stimulated emission) and occurs only at high enough light intensities to modify the optical properties of the system, typically through use of lasers. When an applied electric field of strength  $\vec{E}(t)$  interacts with a system, there is an induced dipole moment per unit volume, or polarization  $\vec{P}(t)$  of a macroscopic medium. The response of the medium can be described using the polarization expressed as a power series in the field  $\vec{E}(t)$  as:

$$\vec{P}(t) = \epsilon_0 [\chi^{(1)}\vec{E}(t) + \chi^{(2)}\vec{E}(t)^2 + \chi^{(3)}\vec{E}(t)^3 + \dots] \quad (2.30)$$

where  $\epsilon_0$  is the permittivity of free space,  $\chi^{(1)}$  is the linear susceptibility, and  $\chi^{(2)}$  and  $\chi^{(3)}$  are the second- and third-order nonlinear optical susceptibilities. The first-order susceptibility term is the most

significant in low-intensity fields, while the higher order terms become more dominant at very high field strengths [18]. Furthermore, CARS is termed a third-order nonlinear process because of the absence of second-order effects due to the inversion symmetry of gas or liquid mediums, leaving  $\chi^{(3)}$  as the lowest order nonlinearity present.

The third-order nonlinear susceptibility  $\chi^{(3)}$  is responsible for four-wave mixing processes, in which three electromagnetic fields interact to produce a fourth field. Within a dielectric medium, the first field creates an initial polarization. With a second field applied, the wave interference results in harmonics at the sum and difference frequencies. When the third field is introduced, it beats with the other two fields and the sum and difference frequencies of all fields and generates the fourth field. This general process of induced nonlinear polarization can result in many different interactions, one of which is CARS [19].

In addition to the resonant CARS signal, a non-resonant background (NRB) CARS signal is also generated from the four-wave mixing process. Instead of originating from resonance with the molecular energy state, the NRB signal is a result of the instantaneous electronic response of the medium and will always be present where the three input fields, i.e., the pump, Stokes, and probe, overlap in time [20]. As seen in Figure 2.8, the NRB process is a combination of the same frequencies as resonant CARS but do not correspond to a resonant state.

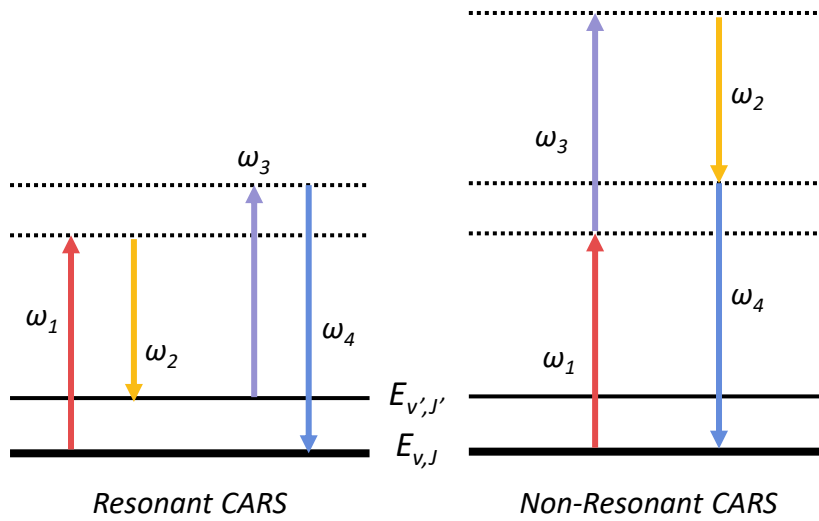


Figure 2.8: Diagrams of FWM processes for resonant and non-resonant CARS [20]

Accounting for both parts of the four-wave mixing, the total susceptibility can be defined as a sum of the resonant part and the non-resonant part:

$$\chi^{(3)} = \chi_{NR} + \chi_{res} \quad (2.31)$$

In the absence of nearby resonances or a low number density of resonant species, the CARS signal will be dominated by the non-resonant susceptibility. Furthermore, the NRB interferes with the resonant CARS signal and limits the sensitivity of the technique [18]. There are several methods to remove the contribution of the NRB and are ideally applied in conjunction with optimizing the resonant CARS signal itself.

The resonant CARS signal intensity can be derived from solving Maxwell's equations for a nonlinear optical medium, resulting in the expression:

$$I_{CARS}(z) = \frac{16\pi^2 \omega_{CARS}^2}{n^4 c^4} I_{pump} I_{Stokes} I_{Probe} |\chi_{res}^{(3)}|^2 z^2 \text{sinc}^2\left(\frac{\Delta kz}{2}\right) \quad (2.32)$$

where  $\omega_{CARS}$  is the frequency of the CARS signal,  $n$  is the refractive index,  $I_{pump}$ ,  $I_{Stokes}$ , and  $I_{probe}$  are the incident beam intensities,  $\chi^{(3)}$  is the third-order susceptibility,  $z$  is the probe volume length,

and  $\text{sinc}^2\left(\frac{\Delta kz}{2}\right)$  is known as the phase mismatch factor [21]. The intensity is linearly dependent on each of the input beams and quadratically dependent on a combined pump-Stokes beam, which is regularly implemented in experimental CARS set-ups. In addition, the signal strength is proportional to the square of the third-order susceptibility magnitude and the phase mismatch factor, or phase matching condition. The phase matching condition is reliant on the mismatch of the wavevectors of the beams, expressed as:

$$\Delta k = (k_{\text{pump}} - k_{\text{Stokes}} + k_{\text{probe}}) - k_{\text{CARS}} \quad (2.33)$$

The CARS signal is only efficiently generated if  $\frac{\Delta kz}{2} \ll 1$ , with  $\Delta k = 0$  called perfect phase matching. This is due to the coherent summation of the anti-Stokes fields emitted from the points along  $z$  for the total field that requires the fields to be in phase to achieve constructive interference [20]. The phase matching angle  $\theta$  between the incoming beams is determined by the Raman resonance frequency ( $\omega_R = \omega_{\text{pump}} - \omega_{\text{Stokes}}$ ) and the dispersion of the medium, given by [22]:

$$\theta \approx \omega_R \sqrt{\frac{2}{n_1 \omega_1} \cdot \frac{\partial n}{\partial \omega}} \quad (2.34)$$

where  $n_1$  is the refractive index of the medium at  $\omega_1$  and  $\partial n/\partial \omega$  is the dispersion of the medium. For small Raman shifts and non-dispersing gaseous media, the phase matching angle  $\theta$  approaches zero and results in a collinear geometry where the desired signal must be separated using spectral filters. However, the collinear configuration has disadvantages resulting from the beams' spatial overlap, such as ambiguous spatial resolution. This can be overcome through other geometries like the BOXCARS approach, which considerably increases spatial resolution, allows for the separation of the output beam via apertures and beam stops, and improves the signal-to-noise ratio of the CARS signal [23, 24].

A depiction of the BOXCARS approach can be seen in Figure 2.9, along with a vector representation of the phase-matching condition. Since initial CARS investigations done in the 1960s, the development

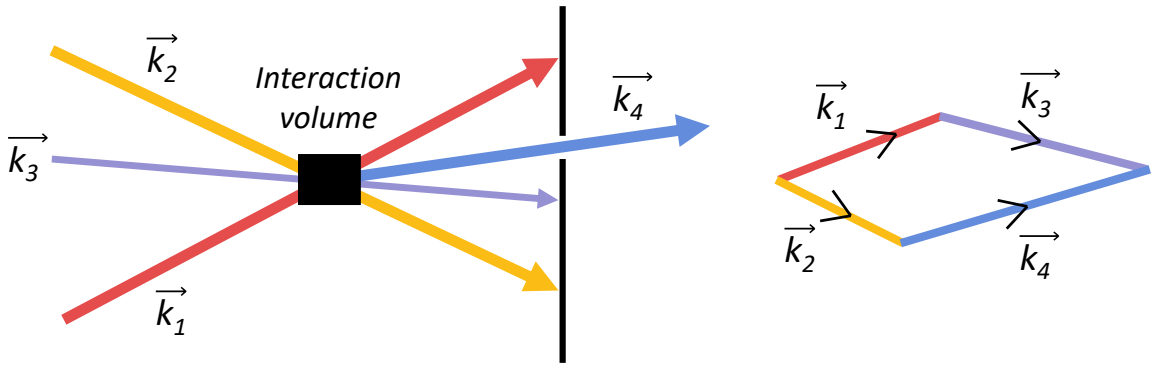


Figure 2.9: BOXCARS configuration (left) and phase-matching condition diagram (right) [14]

of the technique has progressed significantly in its application to gas-phase flows. For sufficient CARS signals, pulsed lasers are implemented due to their high peak power. Nanosecond ( $\text{ns} = 10^{-9}\text{s}$ ) pulse width lasers are the most common diagnostic method which has focused on extending simultaneous temperature and multiple-species concentration measurements. This has been done through a variety of techniques such as: dual- and triple- pump CARS, dual-broadband CARS, and dual-pump dual-broadband CARS. However, the non-resonant background (NRB) signal remains a drawback of this approach and limits its accuracy, sensitivity, and applicability in environments rich in hydrocarbons [25].

Picosecond ( $\text{ps} = 10^{-12}\text{s}$ ) and femtosecond ( $\text{fs} = 10^{-15}\text{s}$ ) CARS were developed to overcome the limitations of NRB interference, dependence on the collisional environment, and the low data-acquisition rate [14]. In ps-CARS, the NRB is suppressed through delaying the probe beam in time from the pump and Stokes beams while measuring state relaxation rates through the same delay [26]. Despite this improvement, ps-CARS alone still contains the same collisional dependence and data-acquisition effects

as ns-CARS. Fs-CARS can address collisional dependence, species-selectivity, and NRB suppression through its significantly higher 1 kHz or greater repetition rate when compared to ns- or ps- lasers [27]. However, fs-CARS is unable to conduct single-shot measurements due to the need to reconstruct the time-domain Raman response of the medium by scanning the fs probe.

At the Faculty of Aerospace Engineering, the experimental set-up is capable of hybrid fs/ps CRS with fs pump and Stokes and ps probe pulse durations. In this configuration, there is high-resolution simultaneous detection of Raman transitions, easily discriminated effects of collisions, and the ability to suppress NRB through temporal pulse delay [28]. Further details of the set-up will be discussed in Chapter 4.

### 2.2.3. CRS spectra and molecular response

Now that the CRS process has been introduced, this section will take a closer focus on the CRS molecular response and factors that affect the experimental spectra. As previously discussed, the CRS signal is created through the interaction between the probe beam and the excited Raman coherence and is imbued with the spectral signature of the molecule's state. The resonance or line position, response strength, and spectral line broadening are all significant for the interpretation of the signal. The location of spectral lines is governed by the molecular structure and allowed transitions, which have been detailed in Section 2.1. The strength of the molecular response is determined by the population distribution of states for a molecule. Therefore, this section will primarily deal with spectral line broadening and its significance to the molecular response.

Theoretically, transitions are introduced as entirely discrete with corresponding spectral lines that can be described with the Dirac  $\delta$ -function. However, in practice there is always a finite linewidth for experimental spectral transitions. The broadening of spectral lines significantly complicate spectral modeling. Consequently, Raman linewidth models are utilized to account for different broadening effects. Spectral line broadening is attributable to several factors, but three main sources are natural broadening, Doppler broadening, and collisional or pressure broadening.

The Heisenberg uncertainty principle relates the uncertainties of an excited state's energy  $E_i$  and mean lifetime  $\tau_i$  through the expression:

$$\Delta E_i \cdot \tau_i \geq \hbar \quad (2.35)$$

The excited state would have an exactly defined energy with an infinite lifetime, however, there is always a finite radiative lifetime that results in natural line broadening. Using the uncertainty principle and energy uncertainty  $\Delta E = h\Delta\nu$ , the frequency spread from natural broadening can be related to the lifetime with:

$$\Delta\nu_N \approx \frac{1}{2\pi c\tau_i} \quad (2.36)$$

Since all atoms or molecules are affected equally, the effect is designated as homogeneous line broadening and results in a characteristic Lorentzian line shape. Natural line broadening is not typically directly observed due to the dominating influence of other sources but sets the absolute minimum width of spectral lines.

For Doppler broadening, the broadening effect is due to the thermal motion of atoms or molecules relative to the observer. It is dependent on the Maxwell velocity distribution and is inhomogeneous, resulting in a Gaussian line shape. Therefore, Doppler broadening becomes more significant at shorter wavelengths and higher temperatures. The characteristic broadening is given by:

$$\Delta\nu_D = \frac{\nu}{2\pi c} \sqrt{\frac{8k_B T \ln 2}{M}} \quad (2.37)$$

where  $\nu$  is the transition frequency,  $T$  is the temperature, and  $M$  is the mass of the atom or molecule. In the visible and UV regions, Doppler broadening exceeds natural linewidth broadening by approximately two orders of magnitude [23].

The last main source is collisional or pressure broadening, resulting from the collisional energy exchange between gas-phase atoms or molecules that reduces the lifetime of the state. The effect is homogeneous, and the rate of collisions is dependent on the density and temperature of the species.

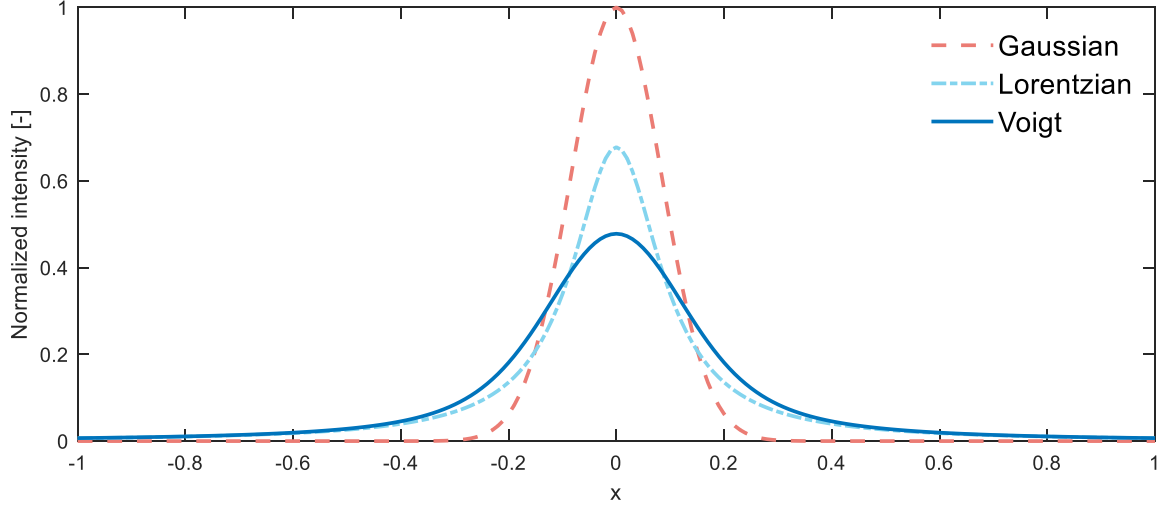


Figure 2.10: Overlaid profiles for Gaussian, Lorentzian, and Voigt line shapes

If a collision is elastic, then no internal energy of the collision partners is transferred and inelastic otherwise. The characteristic line broadening caused by elastic collisions is defined by:

$$\Delta v_{col,elastic} = \frac{1}{2\pi} N_B \cdot \bar{v} \cdot \sigma_b \quad (2.38)$$

where  $N_B$  is the number density of collision parameters  $B$ ,  $\bar{v}$  is the mean relative velocity, and  $\sigma_b$  is the broadening collisional cross-section. For inelastic collisions where the excitation energy of the atom is partially or entirely transferred to its collisional partner's internal energy or into translational energy, the collision is called a quenching collision. The line broadening attributed to inelastic collisions is given as:

$$\Delta v_{col,inelastic} = \frac{1}{2\pi} \sigma_{ik} \sqrt{\frac{8}{\pi \mu k_B T}} \cdot p_B \quad (2.39)$$

where  $\sigma_{ik}$  is the collisional cross-section,  $\mu$  is the reduced mass of the partners,  $T$  is the gas temperature, and  $p_B$  is the pressure. Similar to natural broadening, the effect produces a Lorentzian line shape. However, the experimental collision-induced line shape is dependent on the interaction potential between collision partners and often deviates from a pure Lorentzian profile [23]. Overall, the most dominant types of broadening are from collision effects, but other types such as Stark and instrument broadening can affect spectral lines as well.

In practice, experimental set-ups will need to consider multiple line broadening effects that are defined with different line shapes. If the effects are independent of one another, then the line shape or profile is a convolution of the individual effects. As a result, the line shape typically used for spectral fitting is a convolution of the Gaussian and Lorentz profiles named the Voigt profile.

Shown in Figure 2.10, the three profiles are overlaid on each other for comparison of their features. Both the Lorentzian and Gaussian (or Doppler) profiles are normalized in area, so characteristics of each shape are defined by their distribution around the central wavelength. From observation, the Gaussian line shape has a higher peak while the Lorentzian line shape has larger "tails". If line broadening parameters are known for the molecule of interest, then a realistic line shape can be simulated. Conversely if quantitative spectral measurements have been taken, then the broadening parameters can be found from a spectral fitting algorithm. Through the implementation of linewidth models, quantities such as temperature and concentration of the species can be extracted from experimental CARS measurements [29].

## 2.3. Time-resolved CRS spectroscopy

Time-domain spectroscopy of  $\text{CH}_4$  is the primary focus of this thesis project and requires the comparison of a model with experimental measurements to characterize the  $\nu_2$  vibrational mode. In spectroscopy the most familiar domain is the frequency domain, where a 'steady state' spectrum is observed through radiation intensity dependent on wavelength. However, if frequency-domain spectra are measured at discrete time intervals, the time-dependent progression can be observed. Utilization of time-domain spectroscopy can allow for the investigation of fast processes, such as motion of atoms and molecules or decay of excited energy levels, as well as provide insight about the dynamics of transient environments.

For experimental study of fast processes, the method used must have a sufficient time resolution. This means that the minimum time interval that can be resolved must be shorter than the timescale of the observed process. Through the maturation of ultrashort laser pulses and spectroscopic techniques, very high time resolution has been achieved in the femtosecond to attosecond range [23]. As a result, time-resolved ultrafast laser spectroscopy can acquire useful measurements in both the time and frequency domains [30].

In addition to other pump-probe methods, ultrashort laser pulses have been implemented in time-resolved Raman spectroscopy and CARS [31]. To review, CARS involves three input pulses - pump, Stokes, and probe - which are spatially coincident at the measurement location and ideally phase-matching for momentum conservation. For time-resolved CARS, the Raman coherence is excited in the medium through the simultaneous arrival of the pump and Stokes pulses. The decay of the coherence is then measured with the probe pulse, which is time-delayed by using a translational stage to vary the difference in path length. The process is represented in Figure 2.11 where a broadband fs pump/Stokes exciting the Raman coherence is separated from the ps probe pulse by time delay  $\tau$ .

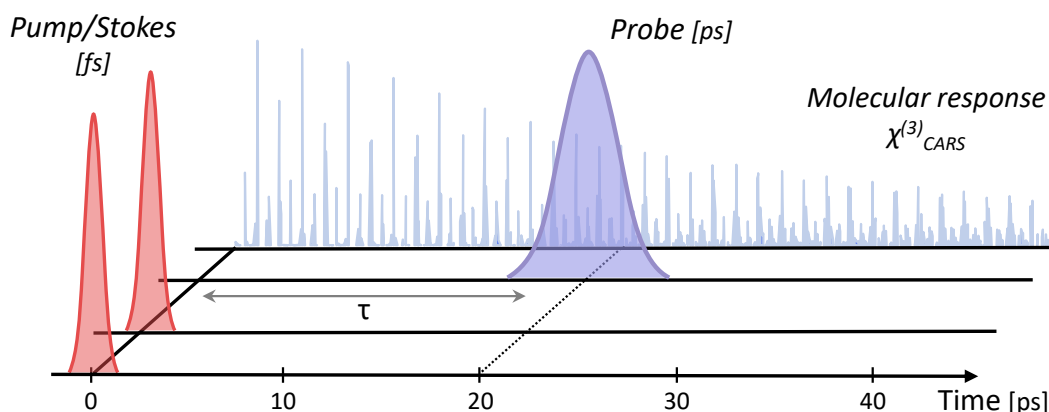


Figure 2.11: Time-domain spectroscopy process illustrating probing of the coherence decay after time delay  $\tau$

As mentioned previously in Section 2.2.2, the temporal delay of the probe pulse suppresses the non-resonant background, which is highest when all three beams temporally coincide and interfere with the observed spectrum [32]. Initially, the ro-vibrational modes are in phase but begin to oscillate at their natural frequency and dephase. Due to the destructive interference caused by the natural dephasing of each Raman transition, the resonant CARS signal exhibits a beating pattern with the process termed frequency-spread dephasing [33]. By delaying the probe relative to the excitation pump and probe pulses, the temporal evolution of excited states can be analyzed.

The time and frequency domains are related through a Fourier transformation, resulting in the time-domain signal decay and period corresponding to the frequency-domain spectrum bandwidth and frequency, respectively [31]. The radiation intensity resulting from a transition can be described in the time-domain as an exponentially decaying sine wave, which can be seen in Figure 2.12. The decay rate of the signal is dependent on molecular composition, temperature, and pressure, all of which affect the rate of collisions. Time-resolved CARS can be used to acquire temperature and concentration measurements but has been focused on molecular dynamics and coherence decay [34].

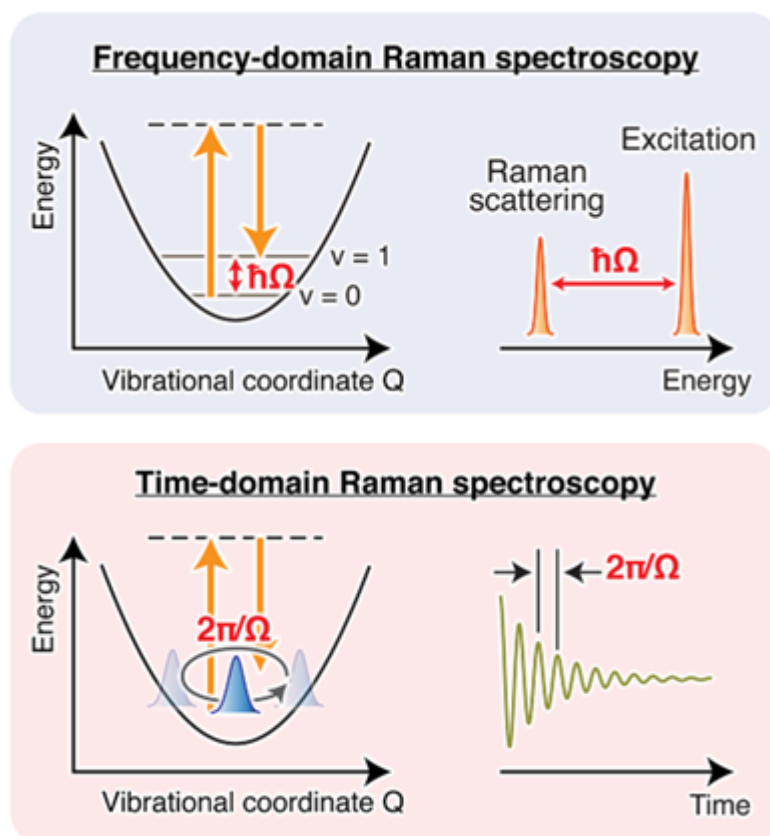


Figure 2.12: Comparison between frequency and time domain Raman spectroscopy [31]

Hybrid femtosecond/picosecond (fs/ps) CARS is a variation of time-resolved CARS that substitutes a broadband, fs probe pulse ( $\omega_3$ ) with a time-delayed narrowband, ps pulse for multiplexed detection of molecular Raman frequencies while maintaining ultrafast time resolution [35]. With this configuration, the relatively narrowband ps-duration probe allows for time-resolved frequency-domain information while a scan through probe delays can provide time-domain information. The technique is unrivalled for non-intrusive gas-phase thermometry due to its comparable precision to fs time-domain spectroscopy with higher accuracy and ability to obtain kHz rate single-shot temperature measurements [35–37]. There are several advantages to hybrid fs/ps CARS that motivate its use in this project.

One of the most significant advantages of fs/ps CARS is the temporal discrimination of the non-resonant background contribution resulting from FWM. Through the probe pulse delay, the non-resonant background can be effectively eliminated while maintaining an adequate signal-to-noise ratio (SNR) [38]. Furthermore, a feature of this approach is the interdependence between the time delay of the probe pulse and the frequency-domain signal that exists due to the spectrally narrow bandwidth of the probe [39]. In addition, the technique can perform measurements within the first few picoseconds of the initial signal decay, which is not affected by collision rates, and extract gas-phase temperatures [34].

# 3

## Time-Domain CRS Model

With the background theory established, this chapter will focus on modeling the methane Raman spectrum for its  $\nu_2$  mode. The modeling approach for generating synthetic  $\text{CH}_4$   $\nu_2$  spectra will be detailed, along with the spectroscopic database used for Raman transitions. Python was used for the initial formatting and filtering of the spectroscopic database while the main model was developed in MATLAB. Section 3.1 introduces prior characterization of methane spectra using various Raman techniques and previous spectroscopy of the  $\nu_2$  mode. Subsequently, Section 3.2 describes the modeling approach for fs/ps CRS in the time and frequency domains. In Section 3.3 an overview of the database for  $\text{CH}_4$  Raman transitions is presented with the procedure for theoretical spectra generation. Finally, Section 3.4 describes the fitting routine to extract quantitative parameters from experimental data.

### 3.1. Methane characterization and Raman spectra

Methane ( $\text{CH}_4$ ) is a primary constituent in natural gas and used as feedstock in chemical reforming. Its status as the second most important anthropogenic greenhouse gas makes it a crucial species to be able to detect and measure with high resolution. Despite its relatively small atmospheric concentration, its global warming potential (GWP) is 28 times that of  $\text{CO}_2$  over 100 years and 84 times more influential over 20 years [40]. This section will present previous endeavors to research and characterize the spectral features of  $\text{CH}_4$ , as well as identifying the literature gap that the thesis aims to address.

Assignment	Symmetry	Degeneracy	Frequency ( $\text{cm}^{-1}$ )
$\nu_1$	$A_1$ - <i>symmetric stretch</i>	1	2932.369
$\nu_2$	$E$ - <i>bending</i>	2	1533.333
$\nu_3$	$F_2$ - <i>stretching</i>	3	3018.529
$\nu_4$	$F_2$ - <i>bending</i>	3	1310.761

Table 3.1:  $\text{CH}_4$  fundamental vibrational frequencies, symmetry, and degeneracy [41, 42]

Methane is a  $\text{XY}_4$  tetrahedral molecule with 9 total vibrational modes that can be described using four Raman-active fundamental modes, depicted in Figure 3.1a. The four normal vibrational frequencies of methane are given in Table 3.1, along with their symmetry groups and degeneracy [41, 42]. A vibrational state of methane can be described using a set of quantum numbers  $(\nu_1, \nu_2, \nu_3, \nu_4)$  with the fundamental frequencies satisfying the relation between stretching and bending modes:

$$\nu_1(A_1) \cong \nu_3(F_2) \cong 2\nu_2(E) \cong 2\nu_4(F_2)$$

Due to this coupling and interaction between the modes, the methane spectrum consists of groups of vibrational states called polyads. Each polyad ( $P_n$ ) and its polyad quantum number can be defined through fundamental vibrational modes using the relation:

$$n = 2(\nu_1 + \nu_3) + \nu_2 + \nu_4 \quad (3.1)$$

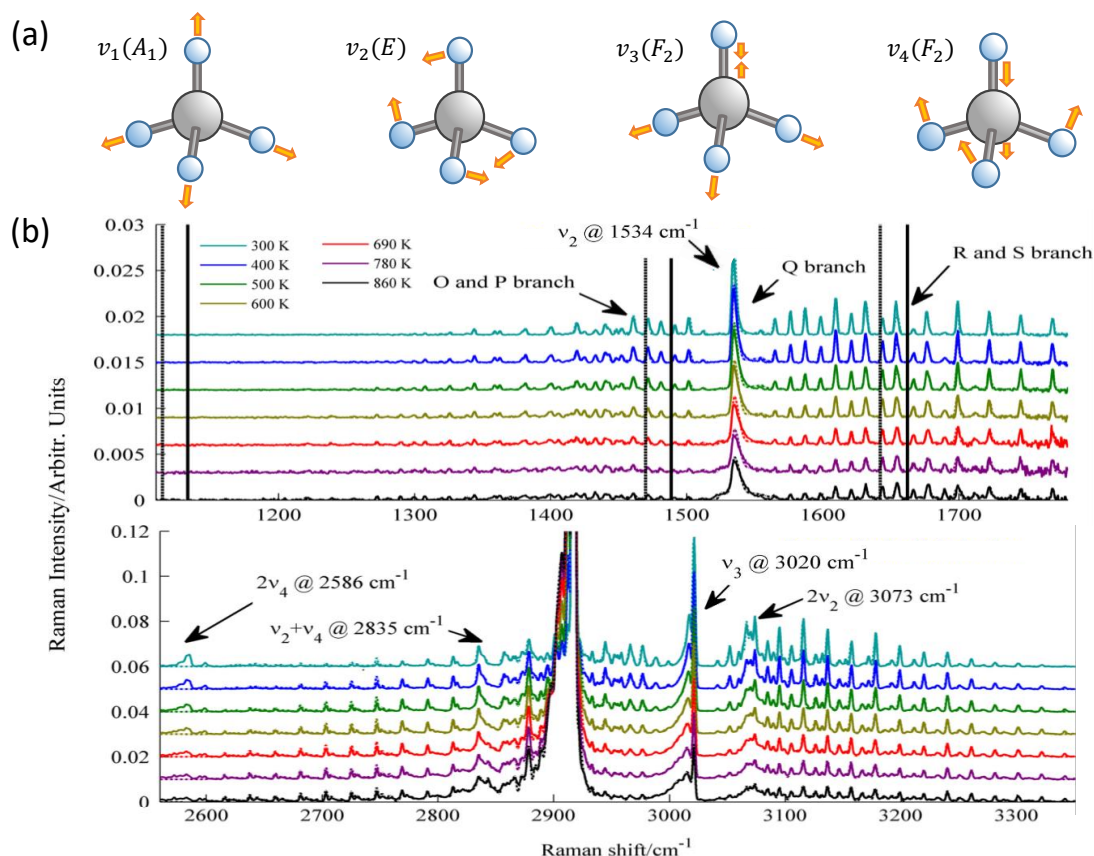


Figure 3.1: (a) Diagrams of the motion of the four fundamental vibrational modes of  $\text{CH}_4$  (b) Corresponding spectra labeled for different modes across between Raman shift of 1200 to 3300  $\text{cm}^{-1}$  [43]

The dyad ( $n=2$ ) is the first of the polyads, occurring around 1500  $\text{cm}^{-1}$  and consists of the  $\nu_2$  and  $\nu_4$  bending modes as individual transitions. The second polyad is the pentad which is present around 3000  $\text{cm}^{-1}$  and contains five Raman transitions:  $\nu_1$ ,  $\nu_3$ ,  $2\nu_2$ ,  $2\nu_4$ , and  $\nu_2 + \nu_4$ . The distortion of a molecule's electric dipole under an applied field, or polarizability, can be represented in various directions by its polarizability ellipsoid. Since  $\text{CH}_4$  is a spherical top molecule, its polarizability ellipsoid is isotropic in its ground vibrational state and in the  $\nu_1$  mode, resulting in no Raman-active pure rotational transitions. In Figure 3.1b, ro-vibrational Raman spectra of the dyad and pentad are given for a range of temperatures with labeled peaks identifying the contributions of fundamental, overtone ( $2\nu_2$  and  $2\nu_4$ ), and combination ( $\nu_2 + \nu_4$ ) modes.

The detection and characterization of methane has developed over the past few decades with use of laser-based non-linear Raman techniques such as stimulated Raman scattering [44, 45], continuous wave (CW) CARS [46–49], and ns CARS [50–56]. In addition, hybrid fs/ps CARS has been utilized for studies of the methane Raman spectrum. Thermometry and species detection of  $\text{CH}_4$  have been achieved with high spectral and spatial resolution using fs/ps CARS [57–61], including single-shot [57] and one-dimensional [58, 61] measurements. Time-domain fs/ps CARS measurements of  $\text{CH}_4$  were performed first at room temperature [60] and later expanded upon at higher temperatures and for longer probe delays [61].

The  $\nu_1$  symmetric stretching mode of methane has been one of the most thoroughly characterized  $\text{CH}_4$  Raman bands under varying temperature, pressure, and gas mixture conditions [45–61]. This is due to the relatively high intensity and larger Raman scattering cross-section of the  $\nu_1$  Q-branch, which is 86 times larger than that of the  $\text{CH}_4$   $\nu_2$  mode [62]. As such, the capability of the  $\nu_1$  Q-branch to be used for thermometry has been verified using spontaneous Raman scattering measurements [43, 63, 64],

ns CARS [56], and hybrid fs/ps CARS [61] along with validation of spectral characteristics of the  $\nu_1$  hot band. However, the  $\nu_2$  bending mode has also been considered to have diagnostic potential.

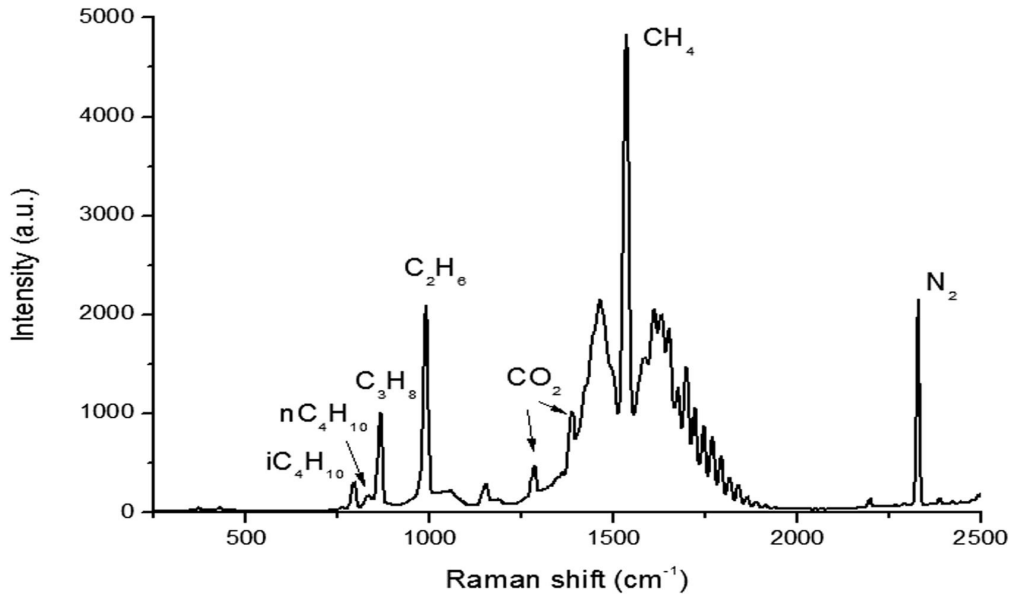


Figure 3.2: Raman spectrum of natural gas in the range 250-2500  $\text{cm}^{-1}$  [65]

While the high intensity  $\text{CH}_4$   $\nu_1$  mode has been sufficiently characterized, other Raman bands of methane are useful in the context of gas-phase diagnostics [62, 65]. For example, diagnostics for natural gas components composition have been developed for the spectral range of 250-2500  $\text{cm}^{-1}$  where the  $\nu_2$  and  $2\nu_4$   $\text{CH}_4$  modes are observed. As seen in Figure 3.2 the  $\text{CH}_4$   $\nu_2$  band intensity is dominant in this spectral range, which also contains the stretching C-C bond vibrations of heavier hydrocarbons and  $\text{CO}_2$  and  $\text{N}_2$  bands [65]. Furthermore, the spontaneous Raman gas analyzer used in [65] was used to study the influence of temperature [66], pressure [67], and gas-mixture [68] on the  $\text{CH}_4$  Raman spectrum and  $\nu_2$  band.

The  $\text{CH}_4$   $\nu_2$  bending mode has been previously studied with infrared absorption focused on collisional effects [69, 70], infrared emission [41], and spontaneous Raman measurements at high temperature [63]. Additionally, spontaneous Raman scattering has been used to acquire high-resolution  $\text{CH}_4$  spectra in the  $\nu_2$  dyad range 1100-1800  $\text{cm}^{-1}$  for a temperature range of 300-860 K [43]. The region was chosen for its importance to combustion diagnostics, since it coincides with bands in the spectra of  $\text{CO}_2$  and  $\text{O}_2$ . The spectral resolution of the experimental set-up in [43] was sufficient to resolve the P and R ( $\Delta J = \pm 1$ ) and S and O ( $\Delta J = \pm 2$ ) branch transitions, but not adequate to resolve the  $\nu_2$  Q-branch ro-vibrational transitions. While [64] does not consider the  $\text{CH}_4$  dyad because of its low SRS signal intensity, it acknowledges the rotational temperature information that could be extracted from the Q, P, O, R, and S branches. With the present research into the  $\nu_2$  band, there are no known CRS applications, time-domain measurements, or flame spectroscopy focused on this spectral region of methane.

### 3.2. Modeling approach

The fs/ps CRS signal intensity can be described as a function of time  $t$  and temporal spacing between the pump-Stokes ( $\tau_{12}$ ) and Stokes-probe ( $\tau_{23}$ ) pulses:

$$S_{\text{CRS}}(t, \tau_{12}, \tau_{23}) \propto \left| P_{\text{res}}^{(3)}(t, \tau_{12}, \tau_{23}) + P_{\text{NR}}^{(3)}(t, \tau_{12}, \tau_{23}) \right|^2 \quad (3.2)$$

with  $\tau_{12}$  and  $\tau_{23}$  representing the time delays between the pump-Stokes and Stokes-probe pulses. Time-domain modeling of the coherent Raman scattering process can begin with the third-order polarization, previously described as the macroscopic non-linear response of a medium to an applied electric field. While the induced polarization includes both resonant and non-resonant components, only the

resonant polarization is considered due to the rapid dephasing of the non-resonant contribution under the assumption of non-resonant input laser fields oscillating at optical frequencies. The resulting time-dependent resonant polarization can be viewed as the gas-phase medium response, or electric susceptibility  $\chi^{(3)}$ , convolved with the input electric field envelopes and written as [39]:

$$P_{Res}^{(3)}(t, \tau_{12}, \tau_{23}) = \left(\frac{i}{\hbar}\right)^3 \int_0^\infty dt_3 \int_0^\infty dt_2 \int_0^\infty dt_1 [\chi^{(3)}(t_3, t_2, t_1) \times E_3(t - t_3) \times E_2^*(t + \tau_{23} - t_3 - t_2) \times E_1(t + \tau_{23} + \tau_{12} - t_3 - t_2 - t_1) e^{i(\omega_1 - \omega_2 + \omega_3)t_3} e^{i(\omega_1 - \omega_2)t_2} e^{i\omega_1 t_1}] \quad (3.3)$$

where  $E_1$ ,  $E_2$ , and  $E_3$  are the electric field envelopes for the pump, Stokes, and probe pulses, respectively. The corresponding frequencies of the pulses are  $\omega_1$ ,  $\omega_2$ , and  $\omega_3$  while  $t_1$ ,  $t_2$ ,  $t_3$  are the coherence timescales during the pump-Stokes, Stokes-probe, and probe-CRS interactions.

Computing the numerical integration of Equation 3.3 can be time intensive because of the three integration domains and motivates simplifications when applicable. The first simplifying assumption is the instantaneous dephasing of the electronic coherence for virtual states, meaning an impulsive molecular response with respect to variations of the pump-Stokes pulses and probe-CRS pulses over the  $t_1$  and  $t_3$  timescales, respectively. Consequently, the molecular response function  $\chi^{(3)}(t_3, t_2, t_1)$  can be modified to  $\delta(t_3)\chi^{(3)}(t_2)\delta(t_1)$ , replacing the response over the first and third coherence timescales with a Dirac delta function. Second, the pump-Stokes time delay can be set equal to zero ( $\tau_{12} = 0$ ) and their electric fields can be written as a single degenerate pulse envelope  $E_{12}$  due to the two-beam experimental setup. With these assumptions, Equation 3.3 can be simplified to the expression:

$$P_{Res}^{(3)}(t, \tau_{23}) = \left(\frac{i}{\hbar}\right)^3 E_3(t) \int_0^\infty dt_2 [\chi^{(3)}(t_2) \times E_{12}(t + \tau_{23} - t_2) e^{i(\omega_1 - \omega_2)t_2}] \quad (3.4)$$

One last assumption is that of an impulsively excited Raman coherence where the envelope of the degenerate pump/Stokes pulse  $E_{12}$  is assumed to be short with respect to the oscillations of  $\chi^{(3)}$ , allowing  $E_{12}$  to be modeled as a Dirac delta function as well and reducing Equation 3.4 further to:

$$P_{CRS}^{(3)}(t) = \alpha E_3(t - \tau)\chi^{(3)}(t) \quad (3.5)$$

With this, the time-domain CRS polarization is obtained as the simple product of the probe pulse envelope and the optical susceptibility instead of the temporal convolution between the pump and Stokes envelopes. When the pump, Stokes, and probe pulses are known, the foundation of the model is based on the molecular response  $\chi^{(3)}$ , or the third-order nonlinear susceptibility. A phenomenological model describes the molecular response as a sum of dampened oscillations with frequencies corresponding to Raman-active transitions, expressed as:

$$\chi_{CSRS}^{(3)} = \sum_k \sum_v \sum_J X_k I_{(v_f, J_f) \leftarrow (v_i, J_i)}^{(k)} \exp \left[ \left( i\omega_{(v_f, J_f) \leftarrow (v_i, J_i)}^{(k)} - \Gamma_{(v_f, J_f) \leftarrow (v_i, J_i)}^{(k)} \right) t \right] \quad (3.6)$$

for transitions between initial  $(v_i, J_i)$  and final  $(v_f, J_f)$  ro-vibrational energy states. In Equation 3.6,  $X_k$  is the mole fraction of the  $k$ -th species in the medium,  $I$  is the Boltzmann-weighted Raman transition intensity,  $\omega$  is the frequency of the transition, and  $\Gamma$  is the transition spectral linewidth, or dephasing coefficient [37]. Further elaboration will be provided for each element of Equation 3.6.

The transition frequency is proportional to the energy difference between the initial and final ro-vibrational states. For  $\text{CH}_4$   $v_2$  transitions, the energy of any state  $E_{vJ}$  is assumed to be the sum of the vibrational and rotational components. If the energies are known, the frequency can be calculated as:

$$\omega_{(v_f, J_f) \leftarrow (v_i, J_i)} = \frac{1}{\hbar c} (E_{vJ_f} - E_{vJ_i}) \quad (3.7)$$

The rotational energy levels are calculated using Equations 3.2 truncated to the second order. While the basics of vibrational energy levels were explained in Section 2.1.1, their calculation differs for polyatomic molecules with high symmetry such as  $\text{CH}_4$ . Instead, the vibrational energy is defined using the

quantum numbers  $v_i$  for the  $i$ -th fundamental vibrational mode with:

$$E_v = (E_{v_1} v_1) + (E_{v_2} v_2) + (E_{v_3} v_3) + (E_{v_4} v_4) \quad (3.8)$$

For each mode at  $J = 0$ , the energies are given as:  $E_{v_1} - 2771 \text{cm}^{-1}$ ,  $E_{v_2} - 1444 \text{cm}^{-1}$ ,  $E_{v_3} - 2930 \text{cm}^{-1}$ , and  $E_{v_4} - 1282 \text{cm}^{-1}$ . When calculating the vibrational energy, the molecule is treated as a harmonic oscillator and the contribution of individual modes are summed for a polyad vibrational state.

In the molecular response function given by Equation 3.6 each Raman transition has a corresponding transition strength proportional to the molecular wave function overlap of the two considered states ( $\langle \Psi_f | \alpha | \Psi_i \rangle$ ), carried out by transforming the initial state wave function by the polarizability operator  $\alpha$  and projecting it onto the wave function of the final state. The Raman transition strength can be expressed as a function of the differential Raman cross-section  $\left(\frac{\partial \sigma}{\partial \Omega}\right)$  and the population difference  $\Delta \rho_{if} = \rho_f - \rho_i$  between the initial and final energy states:

$$I_{if} \propto \left(\frac{\partial \sigma}{\partial \Omega}\right) \Delta \rho_{if}(T) \quad (3.9)$$

where the fractional population of an individual state can be found using Equation 2.26. The differential Raman scattering cross-section is proportional to the probability of an incident photon being scattered at a particular Raman shift and varies for rotational or vibrational transitions, as well as the spectral branch of the transition. Theoretical Raman transition cross-sections can be expressed in terms of quantum numbers for simpler molecules through the Placzek approximation of the polarizability tensor [71]. Typically, the Raman cross-section expressions are represented in a form such as the  $N_2$  pure rotational S-branch cross-section [72]:

$$\frac{\partial \sigma}{\partial \Omega_{S\text{-branch}}} \propto \frac{4}{45} b_{J+2,J} \gamma'^2 F^S(J) \quad (3.10)$$

where  $b$  is the Placzek-Teller coefficient,  $\gamma'^2$  is the polarization anisotropy dependent on the transition and molecule type, and  $F(J)$  is the Herman-Wallis factor. The Placzek-Teller coefficient quantifies the probability of coupling different angular momenta in a two-photon interaction such as Raman scattering, while the Herman-Wallis factor accounts for the influence of ro-vibrational coupling on rotational line intensity. However, a different approach is required for  $\text{CH}_4$  and other spherical top molecules.

The symmetry properties of spherical top molecules increase the degeneracy of their energy levels and complicate descriptions of ro-vibrational interactions. The vibration-rotation energy levels and transition moments of spherical top molecules can be given as straightforward formulas, derived from the rigid rotor and harmonic oscillator approximations, which predict simple, low-resolution spectra [73]. For spherical top spectra of higher resolution, the complexity of the rotational fine structure cannot be predicted by analytical formulas due to the spectral density of ro-vibrational states. This has led to the modeling of states using tetrahedral formalism well-suited for numerical implementation. The full theory involved with this approach goes beyond the scope of the thesis, but is thoroughly detailed in References [73, 74]. Alternatively, a brief description is given for the calculation of the relevant Raman line intensities. For a transition between two states  $i$  and  $f$ , the Boltzmann-weighted Raman intensity strength for a spherical top molecule is given as [74]:

$$I_{if} = R_{if} g_i e^{\frac{-hcE_i}{k_B T}} (2J_i + 1)(2J_f + 1) \left( S_0 |J_{if}|^2 + S_2 |A_{if}|^2 \right) \quad (3.11)$$

where  $R_{if}$  is a constant depending on experimental conditions and  $g_i$  is the nuclear spin statistical weight of level  $E_i$  which is equal to 5, 2, and 3 for A, E, and F symmetries, respectively. The terms  $S_0$  and  $S_2$  are Stone coefficients that depend on the direction of observation and polarizations of the involved electric fields [63]. Finally, the terms  $J_{if}$  and  $A_{if}$  correspond, respectively, to the isotropic and anisotropic parts of the polarizability. Because the  $v_2$  mode is entirely anisotropic and results in a depolarized Raman scatter, only the anisotropic part of the polarizability tensor is non-zero when considering the  $v_2$  transition intensity [43].

The final term of the molecular response in Equation 3.6 is the Raman linewidth  $\Gamma$ . In order to interpret CRS spectra it is necessary to have accurate frequency-domain linewidth, or time-domain decay rate,

models. For hybrid fs/ps CARS the width of the observed CRS spectral lines are dominated by the contribution of the probe pulse linewidth for gas-phase experiments at atmospheric pressure, due to a longer molecular decay timescale relative to the probe decay time [39]. However, since the dephasing mechanism is independent of the probe, the linewidth becomes dictated by collisions once the the probe linewidth is deconvolved.

The coherence lifetime, or linewidth, of an excited ro-vibrational mode is a function of the mechanisms introduced in Section 2.2.3. At atmospheric pressure, most molecules are mainly affected by inelastic collisions resulting in rotational energy transfer with a negligible contribution from Doppler broadening. Because of the spectral and temporal resolution of fs/ps CRS, the collisional dephasing rates of individual rotational lines can be measured through recording peak intensities while delaying the ps- probe pulse in time. Once signal intensity is plotted as a function of probe time delay, the collisional lifetimes associated with state-resolved molecular transitions can be directly measured through the time-decay constant of a single-exponential fit. In turn, collisional frequency-domain linewidths are determined by their respective time constants. For example, an isolated Raman transition will have a Lorentzian linewidth  $\Gamma$  related to the exponential time decay constant  $\tau$  through the expression  $\Gamma = (2\pi c\tau)^{-1}$  with the speed of light  $c$  as a result of inelastic collisional dephasing [75]. Linewidths have been directly measured in the time-domain using time-resolved CARS, but much of the focus has been on diatomic molecules [75–78] - such as  $N_2$ ,  $O_2$ , and  $H_2$  – or basic triatomic molecules like  $CO_2$  [79].

Linewidths for Raman transitions have been modeled through a variety of methods, such as semi-classical calculations, the modified exponential energy gap scaling law (MEG), and energy corrected sudden scaling law (ECS) [29]. For the  $CH_4$   $\nu_2$  mode specifically, ro-vibrational line broadening coefficients were compared with experimental IR absorption spectra for  $CH_4$ -He and  $CH_4$ -Ar mixtures using semi-classical calculations [70]. However, there are no known studies including  $\nu_2$  band linewidth modeling and validation using CRS measurements.

For CARS measurements of  $CH_4$ , linewidths of the  $\nu_1$  Q-branch have been determined through a quantum model for rotational energy transfer [80], semi-classical calculations [54, 56] and MEG modeling [61]. Although [61] focuses on the  $\nu_1$   $CH_4$  Q-branch, it employs hybrid fs/ps CARS to acquire time-domain measurements for validation of its simplified MEG model. In [61], the choice of a MEG scaling law for a linewidth model is justified through its ability to be directly validated by time-domain data and previous success with its use for linewidth fitting of  $N_2$  and  $O_2$  [38, 76, 80]. As a result, the thesis is focused on the modeling approach of [61] and aims to achieve a similar outcome for the  $\nu_2$  ro-vibrational mode. Therefore, a modified exponential gap law is implemented for the calculation of Raman linewidths. The MEG model is a semi-empirical scaling law based on experimental data, expressed as [81]:

$$\Gamma_{ji} = p\alpha \left(\frac{T}{T_0}\right)^{-n} \left(\frac{1 + a\hbar\omega_{v+1,J_i}/k_B T \delta}{1 + a\hbar\omega_{v+1,J_j}/k_B T}\right)^2 \times \exp(-\beta\hbar(\omega_{v+1,J_j} - \omega_{v+1,J_i})/k_B T) \quad (3.12)$$

$$\Gamma_{ij} = \Gamma_{ji} \frac{2J_i + 1}{2J_j + 1} \exp(\hbar(\omega_{v+1,J_j} - \omega_{v+1,J_i})/k_B T) \quad (3.13)$$

$$\Gamma_j = \sum_{i \neq j} \Gamma_{ij} \quad (3.14)$$

where  $\Gamma_{ji}$  is the upward collisional transition from the  $i$ -th rotational state to the  $j$ -th rotational state ( $J_i \rightarrow J_j$ ),  $\Gamma_{ij}$  is the downward collisional transition of the rotational states ( $J_j \rightarrow J_i$ ),  $\Gamma_j$  is the transition linewidth of rotational energy level  $J_j$ ,  $p$  is the pressure,  $T$  is the temperature,  $T_0$  is the reference temperature,  $a$  is a species-specific constant set to 2,  $\omega_{v+1,J_i}$  and  $\omega_{v+1,J_j}$  are the frequencies of the states, and  $\alpha, \beta, \delta$ , and  $n$  are adjustable parameters for least-squares fitting of experimental linewidths. In the study, the linewidth parameters  $\alpha, \beta, \delta$ , and  $n$  were determined using the model and fitting of the time-domain fs/ps  $CH_4$  CARS measurements. However, only two parameters were varied at a time to reduce the number of simulated spectra, resulting in two fitted linewidth models: one validated at 295 K and a second validated from 500 K to 1000 K [61].

### 3.3. Synthetic molecular response and spectral simulation

The generation of synthetic spectra is required for qualitative and quantitative measurements of the  $\text{CH}_4$   $\nu_2$  spectrum time-domain response. To accomplish this, the model described in Section 3.2 is implemented as a MATLAB code which can simulate the spectral response across a range of probe delays. The  $\nu_2$  Raman transitions were obtained from the Methane Calculated Spectroscopic Database provided by the Virtual Atomic and Molecular Data Centre (VAMDC) Consortium [82]. First the database will be introduced, along with the details and format of its calculated line lists. Then, adjustments to the MeCaSDa line lists needed to generate the CRS response will be covered. Finally, an overview of the code for spectral simulation will be described.

The Methane Calculated Spectroscopic Database (MeCaSDa) is a theoretical database containing ro-vibrational methane line lists for both absorption and Raman scattering data [83]. The effective Hamiltonian, dipole moment, and polarizability parameters used to calculate the data were acquired from fits of assigned experimental lines using the XTDS software, developed by the Dijon group [84]. Then calculated line lists for  $^{12}\text{CH}_4$  were generated from an XTDS global analysis of the first four polyads. The database information includes line positions, line intensities, and full descriptions of upper and lower states with associated quantum numbers and symmetries. For the purposes of the thesis only the relevant  $\nu_2$  region between 1200 and 2000  $\text{cm}^{-1}$  was considered, yielding a total of 16 million lines across four different sets of polyad transitions.

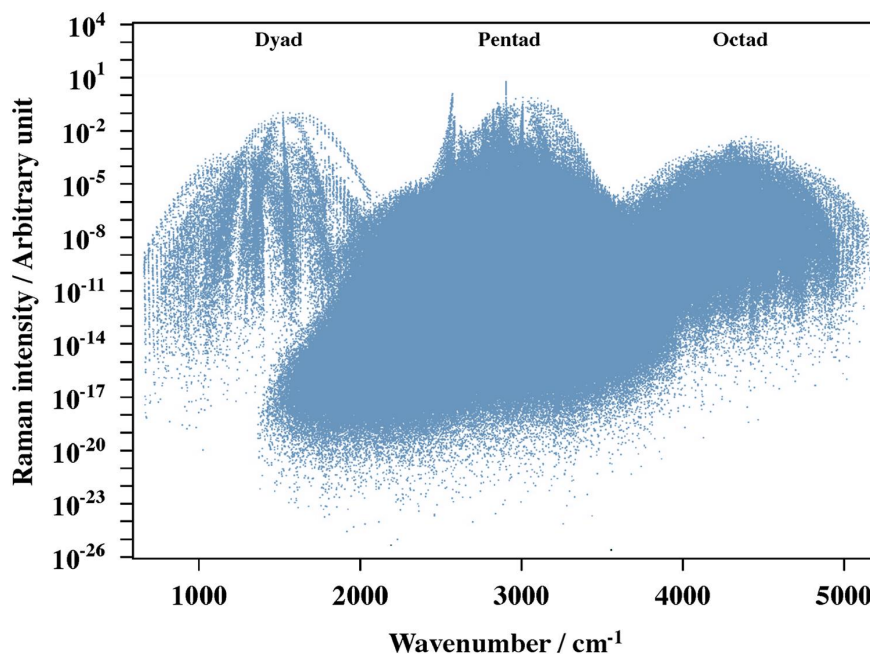


Figure 3.3:  $\text{CH}_4$  Raman transitions included in MeCaSDa, with polyads labeled at the top of the figure [83]

Two main modifications were made to the MeCaSDa line lists before generating synthetic spectra: filtering for only  $\nu_2$ -relevant transitions and rescaling the transition intensities. When constrained between 1200 and 2000  $\text{cm}^{-1}$ , the initial line lists of polyad transitions contained both  $\nu_2$  and  $\nu_4$  Dyad transitions. A filter was applied to include any transitions with a change in the vibrational quantum number for the  $\nu_2$  bending mode, resulting in about 11 million transitions. After the filter, it was necessary to rescale the database intensity values which were calculated for spontaneous Raman transitions. While spontaneous Raman includes the entire Boltzmann population of each ro-vibrational state, CARS and CSRS only account for molecules in a coherent ro-vibrational state. First, the Boltzmann population at the database reference temperature (1450 K) was factored from all the transition intensities. Then, the remaining transition probabilities were multiplied by the population difference ( $\Delta\rho_{i,f}$ ) at room temperature

to obtain the correct intensity weighting. This weighting can be expressed with Equation 3.15:

$$W_{(v_i,J_i)\rightarrow(v_f,J_f)} = I_{(v_i,J_i)\rightarrow(v_f,J_f)} \left( \frac{\rho(v_f,J_f) - \rho(v_i,J_i)}{\rho(v_i,J_i)|T_0} \right) \quad (3.15)$$

where  $W_{(v_i,J_i)\rightarrow(v_f,J_f)}$  are the CRS-weighted line intensities,  $I_{(v_i,J_i)\rightarrow(v_f,J_f)}$  are the spectral database intensities, and  $\rho_{v,J}$  is the Boltzmann distribution of a given state.

After adjusting the database values, the synthetic molecular response and spectrum could be generated. Due to the large number of transitions remaining an intensity-based filter was implemented to reduce the line list to a few million lines. Using a time vector encompassing 1 ns with 8 fs time steps, the time-domain molecular response was calculated with Equation 3.6. In order to not exceed memory limits, the computation of  $\chi^{(3)}$  was implemented as a running sum for every transition input. Subsequently, the time-domain signal was generated by multiplying the molecular response with the probe electric field then performing a Fourier-transform to compute the frequency-domain spectrum.

### 3.4. Theoretical library and fitting routine

To extract quantitative information from CRS spectra, it is necessary to generate a theoretical library to fit experimental measurements. Generally, the theoretical library is created by simulating spectra across a range for the values of interest, such as temperature, concentration, or linewidth parameters. After generation of the library, a spectral fitting technique can be performed to find the best fit for the experimental spectra. For this thesis, the parameters  $\alpha$  and  $\beta$  were chosen to fit the collisional dephasing of the  $\text{CH}_4 \nu_2$  mode at room temperature to reduce the number of synthetic spectra needed for the theoretical library. At every experimental probe delay, the  $\text{CH}_4 \nu_2$  Q-branch intensity is summed and stored as a function of probe delay.

The fitting routine begins with calculating the sum of squares (SSQ) of the residuals between the synthetic ( $I^{syn}$ ) and experimental ( $I^{exp}$ ) spectra with:

$$SSQ = \sum_i (I_i^{syn} - I_i^{exp})^2 \quad (3.16)$$

where  $I$  is the intensity of the spectrum at pixel  $i$ . Once all synthetic spectra in library have been evaluated, the calculated SSQ values can be represented as an optimization surface as a function of the two fitting parameters, such as in Figure 3.4. The minimum of the resulting curve is the best fit of the measured spectrum and optimized parameters. Furthermore, this process can be repeated with increasingly refined libraries until the desired precision of fitting parameters is reached.

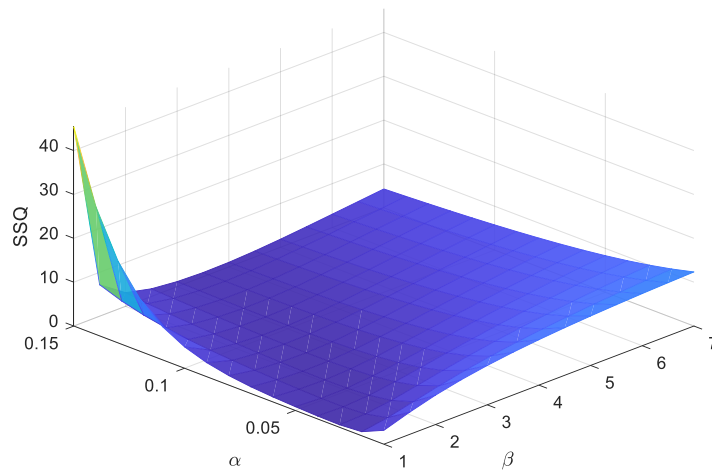


Figure 3.4: SSQ optimization surface for coarse MEG library. Sum of squares values are not normalized for comparison between different library fits.

# 4

## Experimental Methodology

Previous sections have now covered the theoretical background and the modeling approach to the  $\text{CH}_4 \nu_2$  mode molecular response in the time-domain. In the current section, the methodology used to acquire and process experimental data will be detailed. Section 4.1 describes the laboratory setup used to acquire time-resolved measurements and its limitations. In Section 4.2, an overview of the general experimental procedure for spectral measurements will be provided. Finally, the format of the experimental output and data processing measures will be presented in Section 4.3.

### 4.1. Laboratory setup

The experimental setup used for this project is in the Advanced Laser Diagnostics and Flame Laboratory at the TU Delft Aerospace Engineering faculty. It is primarily used for species concentration and temperature measurements in gases and flames. Additionally, the setup incorporates recent CRS spectroscopy advances into the two-beam hybrid fs/ps laser diagnostics system.

In Figure 4.1, a diagram of the system layout is presented where the components are positioned on an optical table with space for measurements across an open-air burner. The layout is based around an ultrafast regenerative amplifier system (7.5 mJ, 1 kHz, Astrella Coherent) which outputs automatically repetition-wise synchronized laser pulses. The output is split into a temporally compressed 35 fs beam (65%, 4.5 mJ) and an uncompressed chirped beam (35%, 2.5 mJ) that is diverted before the amplifier's internal compressor.

The compressed beam is sent to a second harmonic bandwidth compressor (SHBC, Light Conversion) to produce a narrowband 5 ps duration probe pulse. The SHBC-produced probe pulse must be spectrally filtered due to the presence of sidebands resulting from higher-order chirp terms in the bandwidth compression, conducted through sum-frequency generation (SFG) of the pulse. To prevent interference with the CRS signal, the sideband frequencies are removed using a 4f filter in transmission. With the 4f-filter, a transmission grating separates the frequency components of the beam which are then collimated by a lens. At one focal plane behind the lens, the spatial Fourier transform of the input beam is formed and unwanted frequencies are removed with a mechanical slit. After being re-collimated by the second lens, the last transmission grating spatially reconstructs the pulse. Meanwhile, the uncompressed beam is delivered to an external compressor that provides a transform-limited pump/Stokes pulse of 35 fs duration. A transform-limited pulse is one with the shortest possible duration for its optical spectrum, meaning its time-bandwidth product is at a minimum and its instantaneous frequency is time-independent. Furthermore, the external compressor is used to control pulse chirp and compensate for dispersion along the beam path. The final pump/Stokes and probe pulses are centered at 800 nm and 400 nm, respectively.

The difference in path length between the pump/Stokes and probe pulses is offset using an optical delay line, where the relative pulse arrival time set by the position of an automated translation stage with sub-10 fs resolution (Thorlabs). Half-wave plates for 400 nm and 800 nm (Eksma Optics) are placed in the paths of the probe and pump/Stokes beams. Half-wave plates change the polarization orientation of

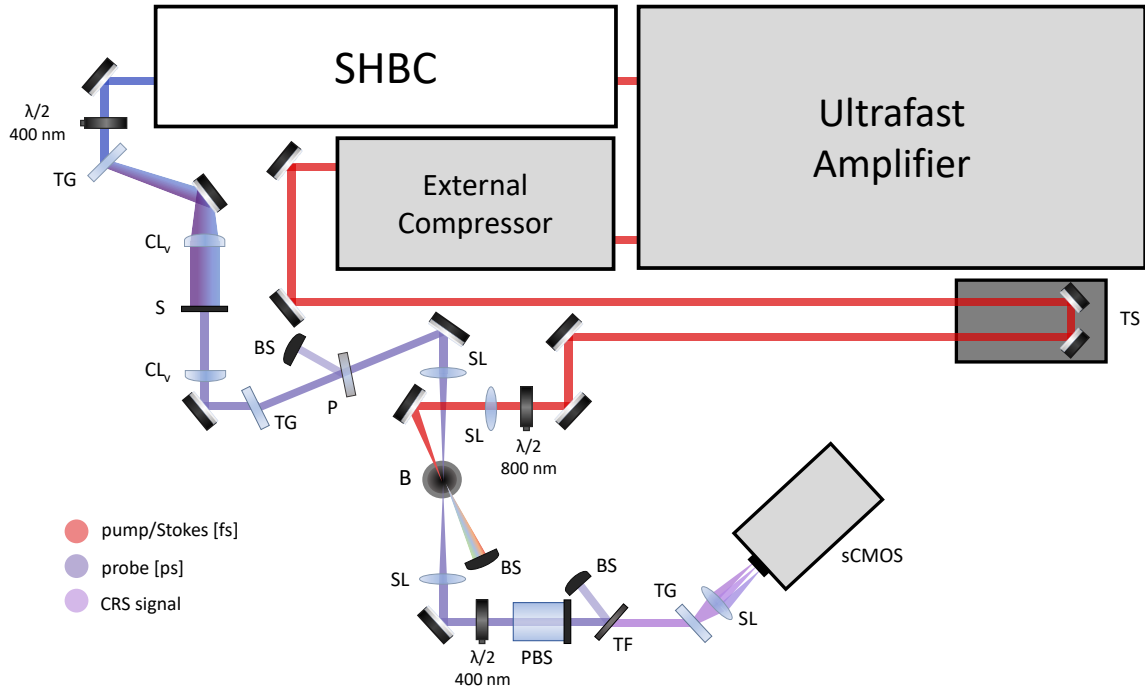


Figure 4.1: Diagram of the ultrabroadband two-beam CRS system. The regenerative amplifier output is split 65%-35% and fed into a second-harmonic bandwidth compressor (SHBC) and external compressor, respectively. TG, transmission gratings; S, slit; SL, spherical lens;  $CL_v$ , cylindrical lenses with vertical alignment symmetry axis; TS, automated translation stage;  $\lambda/2$ , half-wave plates; P, polarizer; PBS, polarization beam splitter; TF, angle-tuneable band-pass filter; BS, beam stop; B, burner.

incident light and are utilized for three goals in this setup: aligning the probe beam with the axis of its transmission gratings (>90% diffraction efficiency at 400 nm, S-pol), controlling the relative polarization of the pump/Stokes beam relative to the probe beam, and rotating the CRS beam polarization to align with the polarization beam splitter and spectrometer grating. Finally, the pump/Stokes and probe beams are crossed following a two-beam phase-matching scheme [28] and focused over the burner using spherical lenses ( $f=500$  mm pump/Stokes,  $f=300$  mm probe) for point measurements.

In two-beam CRS the excitation efficiency at a given Raman shift, or the number of constructive pump/Stokes photon pairs matching the Raman frequency difference, is determined by the bandwidth of the fs pump/Stokes pulse. However, commercially available ultrafast regenerative amplifiers are unable to generate pulse bandwidths capable of exciting transitions past  $400\text{ cm}^{-1}$ . To measure the ‘molecular fingerprint’ region between 800 and  $1800\text{ cm}^{-1}$ , an ultrabroadband pump/Stokes pulse is needed to excite Raman transitions. The experimental setup generates the compressed supercontinuum in-situ, or ‘on-site’ at the measurement location, through the process of fs- laser-induced filamentation [85]. With the high irradiance of the focused pump/Stokes pulse, an intensity-dependent refractive index is induced via the nonlinear Kerr effect. The change in the refractive index causes self-focusing of the pulse and local ionization of the gas medium which produces a visible filament, or plasma channel. In addition, the pulse undergoes self-phase modulation where a phase-shift in the time-domain leads to new frequency components in the pulse spectrum and their temporal compression via nonlinear dispersion in the plasma medium.

Across the burner, the probe beam and CSRS signal are collected and collimated by another spherical lens ( $f=400$  mm). Because the probe beam co-propagates with the CSRS signal, an angle-tuned spectral band-pass filter (Semrock) is used to reject the probe beam before the detector plane. A high-resolution transmission grating (3040 lines/mm, Ibsen Photonics) and a spherical lens are combined to work as a coherent imaging spectrometer to relay and disperse the signal. At the image plane of the spectrometer, a sCMOS camera (Zyla 4.2, Andor) acquires the dispersed signal from a cropped region ( $100 \times 2048$  pixels) at a 1 kHz frame rate with a quantum efficiency of 40% at 400 nm.

## 4.2. Experimental procedure

With the time-resolved CRS spectroscopy theory covered in Section 2.3, this section will present the specifics of the measurement procedure and further experimental details. The main aim of the experiments is to acquire time-resolved measurements of the  $\text{CH}_4 \nu_2$  spectrum to validate the collisional dephasing model. This is achieved through performing a probe delay scan, which consists of varying the time delay  $\tau$  of the probe relative to the pump/Stokes pulse to measure the decay of the coherently excited ro-vibrational mode. Furthermore, measurements were taken across a  $\text{CH}_4/\text{air}$  diffusion flame to demonstrate the diagnostics potential of  $\text{CH}_4 \nu_2$  CRS spectroscopy in chemically reacting flows.

The time-resolved  $\text{CH}_4 \nu_2$  measurements were taken in a gas flow provided by a Bunsen burner made of a stainless-steel pipe. The internal diameter of the pipe was measured to be 19 mm with a length selected for fully developed flow at the pipe exit. The methane gas flow was supplied by a pressurized tank and regulated by a mass flow controller (Bronkhorst) while keeping the volumetric flow rate below 5 standard liter per minute (SLPM) to ensure laminar flow.

Separate from the primary  $\text{CH}_4$  measurements, argon gas is also supplied to the burner pipe to characterize the probe pulse and measure the non-resonant spectrum. Argon is chosen because it is a noble gas with no resonant Raman transitions. The time-domain envelope of the probe pulse is measured through its own probe-delay scan in argon, which allows for the definition of the probe peak at  $t = 0$  relative to the delay stage position. Furthermore, the non-resonant spectrum and its background is acquired in argon to measure the pump and Stokes electric field envelopes ( $E_2^* \times E_1$  in Equation 3.4) and determine the frequency-dependent excitation efficiency of the Raman coherence. With the known excitation efficiency, the resonant CRS spectrum can be corrected through normalization with the non-resonant spectrum.

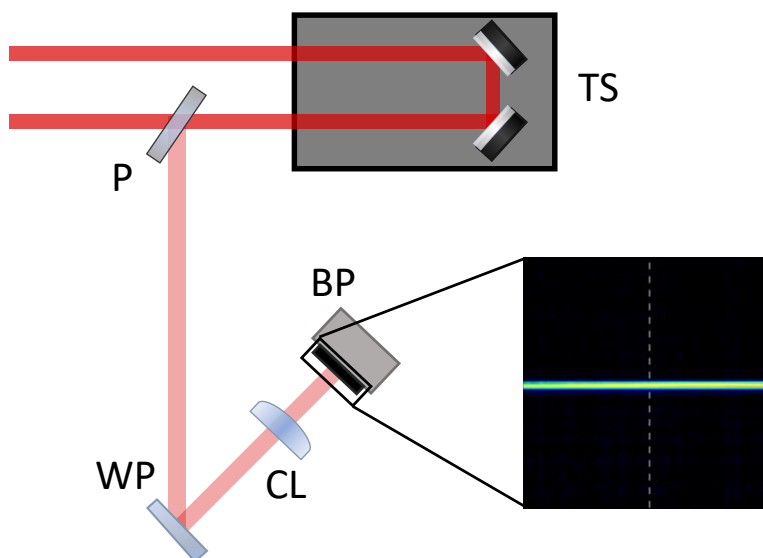


Figure 4.2: Diagram of optical setup for pump/Stokes beam alignment. TS, translation stage; P, polarizer; WP, wedge plate; CL, cylindrical lens; BP, beam profiler.

An important consideration during the measurements was the maintenance of the beam alignment while moving the optical delay stage, which would cause changes in the vertical position of the pump/Stokes beam. As a result, the change in beam position was compensated for by adjusting the pitch of the delay stage mirrors. A reference was needed to ensure that the beam was as close as possible to its original position. After the delay stage, a combination of a polarizer with a half-wave plate was used to attenuate a rejected portion of the beam as the position reference. Then, the rejected part of the beam ( $\sim 100\mu\text{J}$ ) was directed to a wedge plate and focused by a cylindrical lens ( $f:=500\text{ mm}$ ) onto a beam profiler (DataRay). The initial position of the resulting sheet was marked at the beginning of each experiment and was used as a reference for beam re-adjustment after each movement of the delay stage.

For all experiments, the gas flow was started earlier than the measurements to guarantee stable flow. The background signal was acquired in the gas flow for later image processing. A general procedure was followed for the acquisition of time-resolved CRS measurements. First, the optical delay stage was set for probe delay  $\sim 30$  ps and the initial position of the reference beam would be recorded. After checking the quality and position of the dispersed signal, the camera was used to acquire spectra with initial acquisition settings. Between measurements, the delay stage would be moved with steps of 5 ps while re-adjusting the beam to match the reference position each time. This acquisition process was repeated until the signal could no longer be detected. For the delay step immediately before this point, the same spectrum was re-recorded with an increased exposure time to obtain a point of comparison between the two acquisition halves of the probe delay scan. Then, the acquisition procedure continued with the increased exposure until the signal disappeared once again. Overall, for collisional dephasing measurements the probe pulse could be delayed up to 180 ps for single-shot and 10-shot averaged spectra and up to 220 ps for exposure times of 10 and 20 ms. Further details of the acquisition settings and output image processing are provided in Section 4.3.

In the same manner as for pure  $\text{CH}_4$ , collisional dephasing measurements were acquired in different gas mixtures of  $\text{CH}_4$  with  $\text{N}_2$ , Ar, and  $\text{H}_2$ . At room temperature and atmospheric pressure, measurements were performed in a gas flow provided through a stainless-steel T-junction and managed by digital flow controllers. Acquisitions began in a pure  $\text{CH}_4$  flow as a control, starting with an exposure time of 10 ms and increasing to 20 ms when the CRS signal diminished. With each gas mixture, the  $\text{CH}_4$  flow was first replaced by 25%, then 50% of either with  $\text{N}_2$ , Ar, or  $\text{H}_2$ . The maximum achievable probe pulse delay was dependent on mixture and ranged from 170 ps to 230 ps.

In addition to the probe delay scans, point-wise measurements were taken across a laminar  $\text{CH}_4$ /air diffusion flame provided by the Bunsen burner. The  $\text{CH}_4$  flow was set to a velocity of 2.65 cm/s for laminar flow and a steel mesh was placed 15 mm above the burner rim to stabilize the flame. The measurements were positioned  $\sim 1$  mm above the burner rim and acquired at 25 locations across the flame front. The sequence of measurements is shown in Figure 4.3, beginning at the center of the burner ( $y=0$  mm) to beyond the flame front ( $y=12$  mm) in steps of 0.5 mm. At each measurement location, 10-shot-averaged CRS spectra were acquired at a constant probe delay of  $\tau_{pr} = 32$  ps.

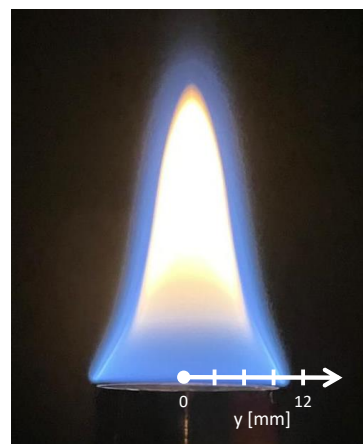


Figure 4.3: Measurement locations across a  $\text{CH}_4$ /air diffusion flame for  $\tau_{pr} = 32$  ps. Acquisitions were taken at 25 locations in steps of 0.5 mm.

### 4.3. Output and data processing

The result of the pump/Stokes and probe pulse interaction is the CSRS signal containing the spectral response of the  $\nu_2$  mode. As previously discussed, the co-propagating probe beam is rejected before the CSRS signal is directed to a coherent imaging spectrometer. The signal is then dispersed into its frequency components and focused onto the pixels of the camera. This section covers the acquisition settings used for both single-shot and shot-averaged measurements. In addition, the processing steps taken to extract final spectra from the raw image measurements are presented.

At the end of the spectrometer, the signal is captured with an Andor Zyla 4.2 sCMOS camera using its accompanying Andor Solis software. The sCMOS camera sensor measures  $13.3 \times 13.3$  mm and contains a pixel array of  $2048 \times 2048$ , leading to a pixel size of  $6.5 \mu\text{m}$ . The pixel array was cropped to a region  $50 \times 2048$  pixels to collect the spectra while forgoing unnecessary image acquisition of the surrounding sensor array. The collected photons at the pixels are represented as the image intensity, with each pixel saturating at 65535 photon counts. The primary factors for determining the acquisition settings were the signal intensity and the signal-to-background ratio (SBR), as viewed through the camera software.

For every measurement of the resonant signal, 1000 frames are acquired to compensate for shot-to-shot fluctuations. Initially the CRS signal intensity would be sufficient for a 'single-shot' measurement, or the capturing of the dynamic process using a single excitation pulse, with a repetition rate of 1 kHz

and exposure time of 1 ms. Single-shot acquisitions were implemented as long as possible for higher measurement accuracy and precision. However, as the measured coherence decay (or probe delay) progressed, the signal intensity and signal-to-background ratio diminished. This prompted the change to acquiring to shot-averaged measurements, where the exposure time was increased to 10 ms for a 10-shot average to improve the signal-to-background ratio of the spectra. The resulting data series of each measurement were read from the Solis software into MATLAB as intensity matrices for further processing.

The captured raw camera images must first be processed into relatively uniform spectra before applying a fitting routine for the model. The processing includes measures such as background subtraction, binning, spectrum calibration, and baseline correction. For acquisitions with substantial noise, smoothing procedures may also be applied. Additionally, the intensity between the single-shot and shot-averaged measurements must be reconciled for consistency during the probe delay.

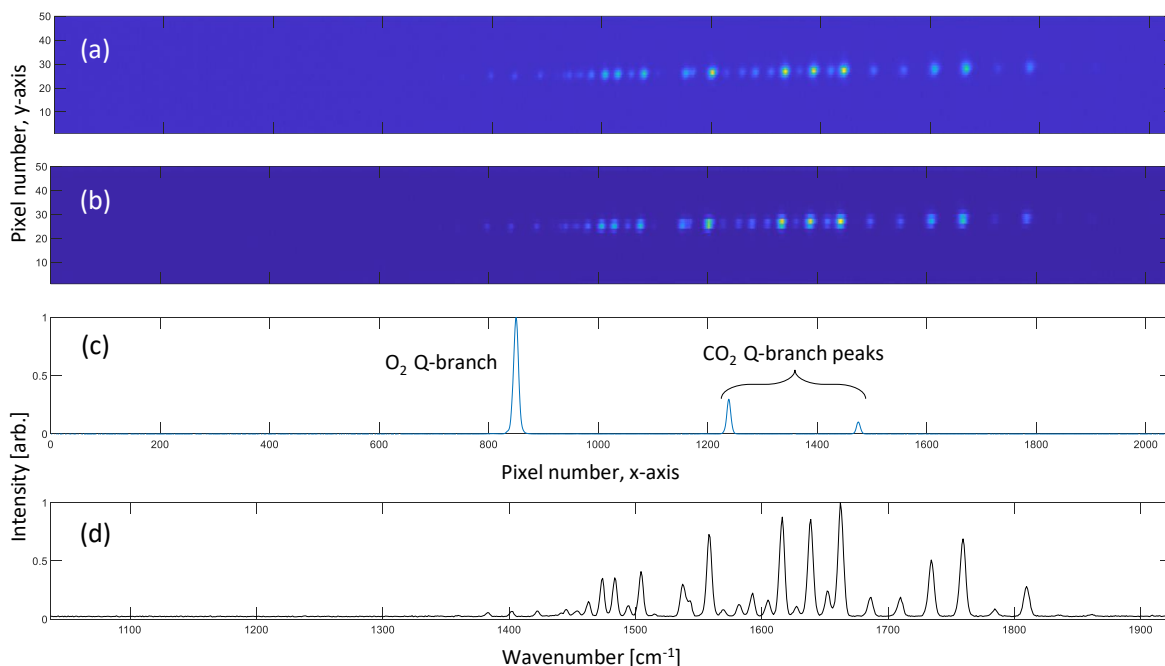


Figure 4.4: General image processing for each acquired spectra shown at probe delay of  $\tau = 48.3$  ps. (a) Single shot raw image captured with 1 ms exposure time. (b) Image after background subtraction and 2x2 binning. (c) Calibration spectrum containing O<sub>2</sub> and CO<sub>2</sub> Q-branch peaks used to convert x-axis pixels to wavenumber [cm<sup>-1</sup>]. (d) Resonant line spectrum after frame-averaging, normalization, and wavenumber calibration.

Background subtraction, binning, and frequency calibration were implemented for all acquired spectra. In Figure 4.4 each step of the process is shown, starting with the raw camera image of the CRS signal (Figure 4.4a). For a set of resonant acquisitions, the corresponding non-resonant background was averaged over 100 frames and subtracted from all the resonant images. The subtraction of the background is meant to reduce the image noise through removing possible stray light. Next digital binning is applied to the spectra, which is the grouping of adjacent pixels into one output intensity value. The measurement images are binned 2x2 to increase the signal intensity at the expense of resolution (Figure 4.4b). Finally, the spectral x-axis of the spectra must be calibrated for the correct Raman shift. Calibration is accomplished through measuring the frequency difference of two known peaks, then scaling the axis with the ratio between frequency and pixel number. For this purpose, another acquisition was taken in air while exhaling so that the resulting spectrum contained known fundamental peaks of O<sub>2</sub> and CO<sub>2</sub> (Figure 4.4c). An example of a processed spectrum is shown in Figure 4.4d, where the intensity of the vertical pixels has been summed and the 1000 frames are averaged to produce a single line spectrum plot along the calibrated x-axis.

Most acquired spectra were of good quality with a high signal-to-background ratio, but further adjustment was sometimes needed on an individual basis. One of the most frequent adjustments was the

correction of the spectrum baseline for uniform peak measurements. Uneven baselines present in the data were attributed to possible amplified spontaneous emission (ASE) from the filament which is spatially coherent and can be detected by the sensor. In this thesis, the baseline was corrected using polynomial curve-fitting to preserve the spectral contours and intensities of the resonant Raman spectra [86]. Furthermore, the spectra SBR typically decreased with a probe delay increase, making it harder to identify clear spectral peaks. The effect of the baseline correction is demonstrated in Figure 4.5 for a longer probe delay ( $\tau = 153.3$  ps) and shows the resulting difference in peak intensity. In the small number of cases that required it, the remaining noise was attenuated by smoothing the spectra using a Savitsky-Golay (SG) filter [87]. However, the trade-off in using a smoothing filter is the possibility of losing smaller spectral peaks amongst the noise.

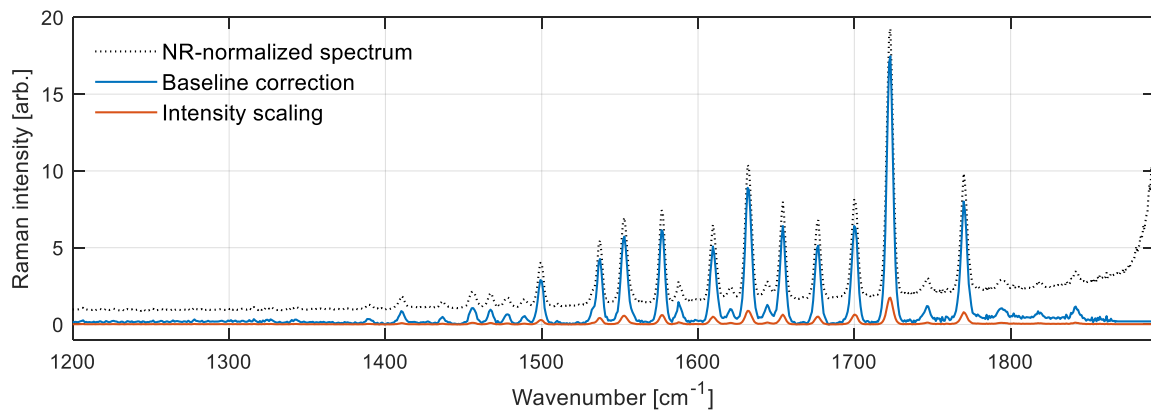


Figure 4.5: Individual processing steps conducted for probe delay  $\tau = 153.3$  ps. After normalization with the NR spectrum, the baseline of the  $\nu_2$  spectrum may still be offset along the y-axis. The baseline is corrected through subtracting a polynomial curve fit [86]. For acquisitions in the latter half of the probe delay scan, the intensity was scaled to match the relative magnitude of the initial half on the basis of exposure time.

The last processing measure was based on reconciling the single-shot and shot-averaged segments of the probe delay scan. Because the purpose of the scan is to measure the signal coherence decay, the spectral intensity must be consistent across all measurements. Under the assumption that the intensity was proportional to the number of laser pulses detected within the exposure time, the 10-shot-averaged measurements were divided by a factor of 10 to obtain spectra comparable to single-shot measurements. This process was repeated for other data sets with different acquisition conditions, but always using the intensity of the initial probe delay to determine the value used in scalar division of intensity. In Figure 4.5 the result of this scaling is shown to greatly diminish peak intensity, which is dependent on the difference of exposure time between the two image acquisition sets. One further method was attempted with the use of a doubly-acquired spectra to compute a scaling factor to apply on the latter-acquired spectra. This was done by dividing the two spectra at the same point to obtain a pixel-by-pixel scale across the different Raman shift frequencies. The implications of these two scaling methods on the collisional dephasing parameters will be discussed in Chapter 5.

# 5

## Results and Discussion

The focus of this chapter is the presentation of the experimental measurements and the resulting linewidth fitting parameters from the time-domain model. Section 5.1 introduces the structure of the  $\text{CH}_4 \nu_2$  spectrum and the time-resolved measurements of its initial collision-independent coherence decay ( $\tau_{pr} < \sim 80$  ps). Furthermore, experimental results for different spectral branches are compared with the output of the theoretical model. Following this, Section 5.2 will present acquired measurements for longer probe delays ( $\tau_{pr} > \sim 80$  ps) in addition to the fitting results of the MEG model used to characterize the collisional dephasing. Finally, Section 5.3 will show  $\text{CH}_4/\text{air}$  diffusion flame measurements to evaluate the diagnostic potential of the  $\text{CH}_4 \nu_2$  spectrum for reacting flows.

### 5.1. Time-resolved $\text{CH}_4 \nu_2$ measurements

A necessary step for characterizing the  $\text{CH}_4 \nu_2$  Raman spectrum is the measurement of its time-domain response. After the Raman coherence is impulsively excited by the pump/Stokes beam, the probe pulse is delayed in order to measure the coherence dephasing, or decay, of the  $\nu_2$  mode. For the initial coherence decay the  $\text{CH}_4 \nu_2$  spectrum was measured in a room-temperature gas flow with single-shot acquisitions. In Figure 5.1, the  $\text{CH}_4 \nu_2$  coherent Stokes Raman scattering (CSRS) spectrum is presented in the spectral range  $1200\text{-}1900 \text{ cm}^{-1}$ .

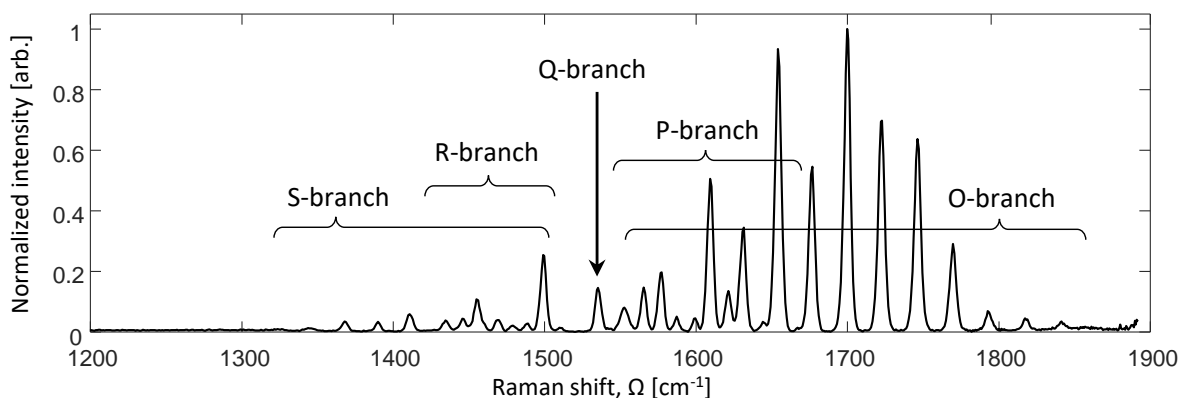


Figure 5.1: Single-shot  $\text{CH}_4 \nu_2$  CSRS spectrum acquired at  $T = 296 \text{ K}$  and  $\tau_{pr} = 28.3 \text{ ps}$ . Spectral branches are labeled in reverse from that of a CARS spectrum, with negative quantum number transitions ( $\Delta J = -1, -2$  for P- and O- branch, respectively) appearing at a higher frequencies.

The spectrum was acquired on the Stokes side of the overall CRS signal and is negatively shifted from the probe frequency opposite to the positively shifted anti-Stokes spectrum. Consequently, any negative changes in the total angular momentum quantum number appear at larger transition frequencies. While the previously discussed theory and spectroscopic  $\text{CH}_4$  data is still applicable to CSRS spectra,

the order of the branch labels must be reversed such that O- and P- branches occur at higher Raman shifts compared to R- and S- branches.

With selection rules allowing  $\Delta J = 0, \pm 1, \pm 2$  ro-vibrational transitions, the  $\nu_2$  spectrum contains all five spectral branches as labeled in the figure. The Q-branch is present at  $1535 \text{ cm}^{-1}$  as a single convolved peak. Although the Q-branch contains a finer rotational structure, the probe bandwidth of  $4.1 \text{ cm}^{-1}$  limits the spectral resolution. At room temperature, the distinguishable peaks in the frequency-domain extend from S(8) around  $1344 \text{ cm}^{-1}$  to O(14) present at  $1841 \text{ cm}^{-1}$  for  $\Delta J = \pm 2$  transitions. The R- and P- branches can be determined from their closer spacing (approximately  $2B$  apart) and overlap with the S- and O- branches, resulting in convolved spectral lines. Figure 5.1 presents clear R-branch peaks up to R(8) at  $1449 \text{ cm}^{-1}$  while the P-branch extends to P(11) at  $1656 \text{ cm}^{-1}$ .

The time-domain response of the  $\nu_2$  spectrum was recorded through the probe delay scan procedure described in Section 4.2. From these measurements a spectrogram can be constructed to visualize both frequency- and time-domain behavior. Figure 5.2 provides two spectrograms to compare experimental measurements with the modeling results for the  $\text{CH}_4 \nu_2$  CRS spectrum. For the experimental spectrogram in Figure 5.2(a), each single-shot CSRS spectrum was normalized to its maximum intensity and plotted for its probe pulse delay relative to the pump/Stokes from 32 to 85 ps with delay steps of 2.2 ps. The time-domain CRS model was used to generate a synthetic spectrogram spanning the same range of probe delays which is shown in Figure 5.2(b).

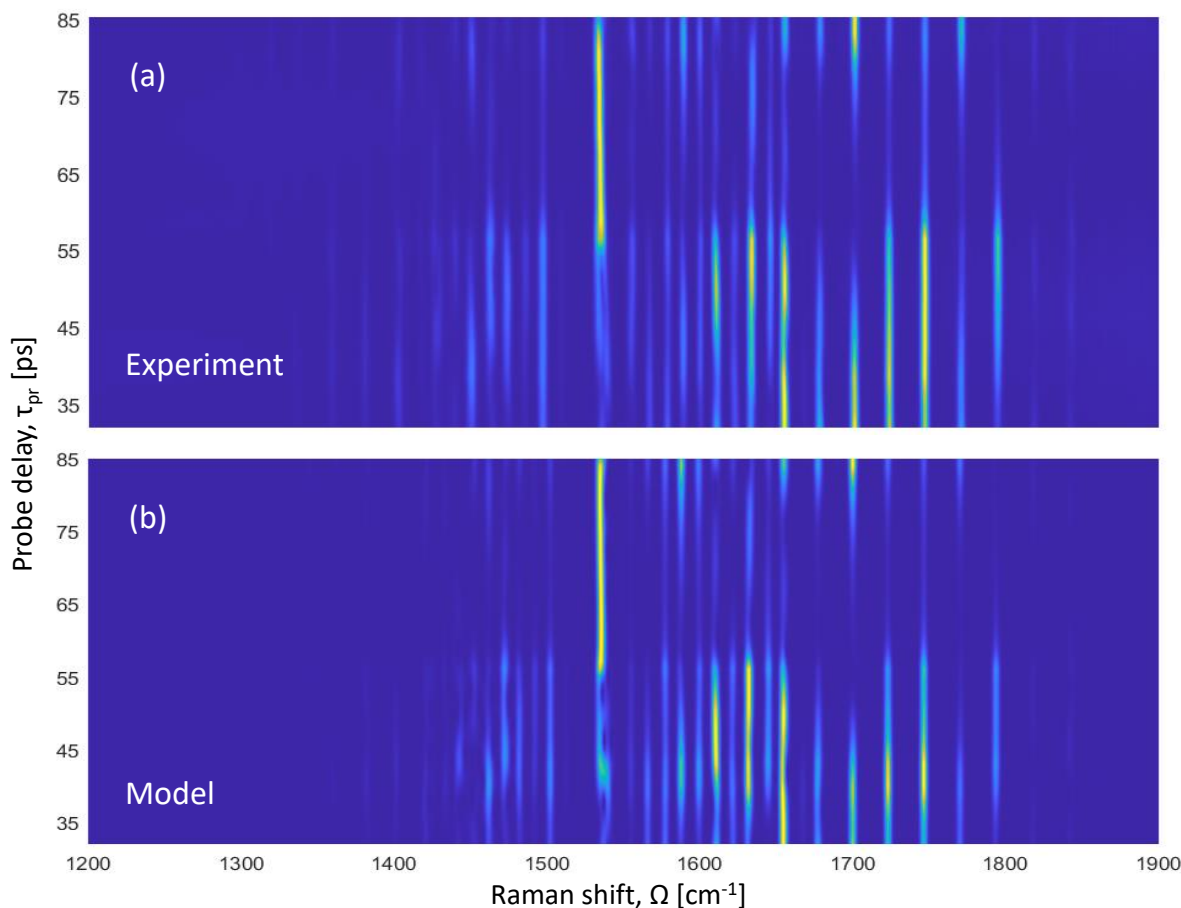


Figure 5.2: Time-resolved  $\text{CH}_4 \nu_2$  CRS spectrograms with probe pulse delay extending from  $\tau_{pr} = 32 \text{ ps}$  to  $\tau_{pr} = 85 \text{ ps}$  for comparison of experimental and time-domain model results. Individual spectra at each probe delay are normalized to their maximum intensity value. (a) Experimental spectrogram of the  $\text{CH}_4 \nu_2$  mode acquired in a  $\text{CH}_4$  gas flow with single-shot measurements at  $T = 296 \text{ K}$  and ambient pressure. (b) Modeled spectrogram at  $T=296 \text{ K}$  considering only the fundamental  $\nu_2$  mode ( $0000 \leftarrow 0100$ ) which limits the included rotational states from  $J=1$  to  $J=23$

There is excellent agreement between the experimental and synthetic spectrograms, as seen from the recreation of the beating behavior of the spectrum. Coherence beating, or the increase and decrease of peak intensity over time, results from spectral lines unresolved by the probe pulse bandwidth. Within this timescale the close spacing of the frequency content of the spectrum produces interference, which in turn causes the initial decay of the macroscopic Raman polarization, contributes to peak convolution, and affects the beating intensity and complexity [34]. In addition, coherence beating is sensitive to temperature since the presence of hot bands increases the number of transitions included in convolution of spectral peaks. For hybrid fs/ps CRS spectra, coherence beating has been observed for unresolved S-branch triplet transitions of O<sub>2</sub> [88] and as a result of unresolved hot bands in high-temperature N<sub>2</sub> and CO<sub>2</sub> measurements [89, 90].

The dynamic behavior of the room-temperature CH<sub>4</sub>  $\nu_2$  CRS spectrum can be further analyzed through comparison with the output of the time-domain model. Considering the timescale of this initial behavior, the main factor in modeling the  $\nu_2$  coherence beating is the number of Raman transitions included in the summation of Equation 3.6. As explained in Section 3.3, the spectral database was first filtered to only include fundamental  $\nu_2$  transitions between the ground and first vibrationally excited states (0000←0100), then filtered again through an intensity-based cut-off value to reduce computational time. A similar procedure was carried out in [61], where the number of transitions taken into account for modeling the  $\nu_1$  mode was limited to 336 lines at 295 K. Because the time-domain model can recreate the temporal beating seen in Figure 5.2(a), it can be inferred that vibrational hot bands do not influence room-temperature CH<sub>4</sub>  $\nu_2$  CRS spectrum. For an intensity cut-off value of  $1e^{-4}$ , the number of included lines is reduced to 3244 for all branches, appearing sufficient for modeling the overall beating pattern of the  $\nu_2$  spectrum. Each of the branches in Figure 5.2 can be investigated in further detail to better understand the beating characteristics for different components of the spectrum.

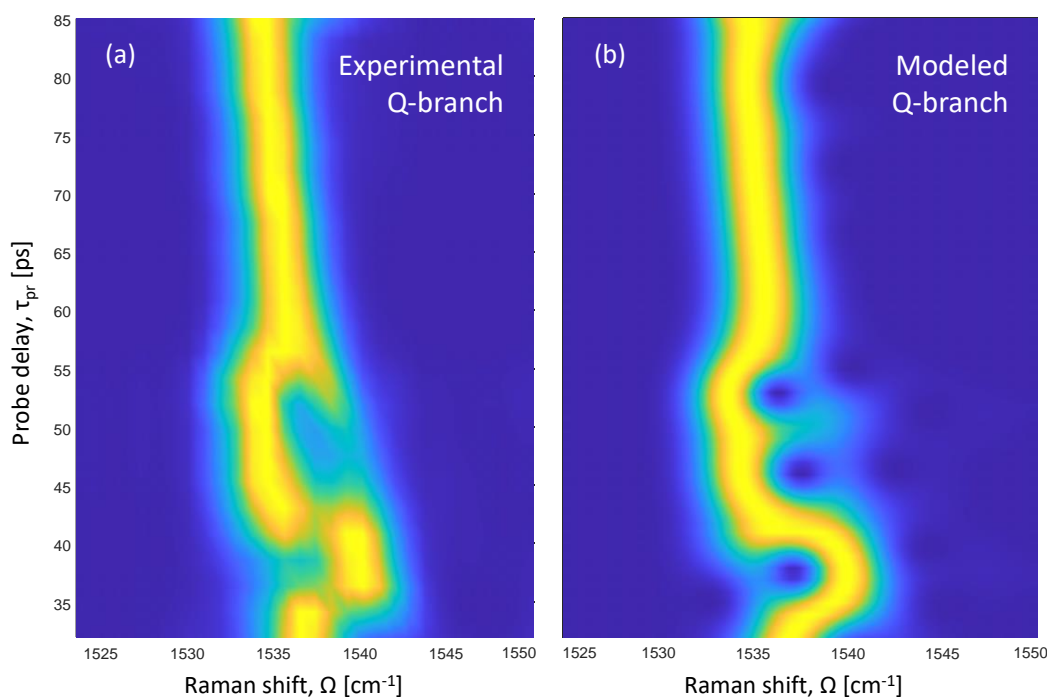


Figure 5.3: Comparison between experimental and modeled CH<sub>4</sub>  $\nu_2$  Q-branch spectrograms. (a) Experimental Q-branch spectrogram acquired in room-temperature CH<sub>4</sub> flow. (b) Modeled spectrogram using 558 filtered spectral lines to model the  $\nu_2$  Q-branch.

Figure 5.3 presents the  $\nu_2$  Q-branch as spectrograms isolated from Figure 5.2. While the Q-branch appears as an unresolved feature in frequency-domain spectra, the experimental spectrogram in Figure 5.3(a) reveals a complicated initial beating pattern centred around 1535 cm<sup>-1</sup>. The Q-branch peak is seen to shift by as much as 5 cm<sup>-1</sup> and occasionally splits below a probe pulse delay of 60 ps. After the filtering was applied to the spectral database, the remaining number of Q-branch lines included in the model was 558 which consequently limited the included rotational states from J=1 up to J=23; this

was sufficient to replicate the specific beating characteristics of the Q-branch as seen in Figure 5.3(b).

In addition to the Q-branch, interesting dynamic behavior is observed for S-, R-, P-, and O-branches of the  $\text{CH}_4 \nu_2$  CRS spectrum. As shown in Figure 5.4, different beating phenomena can occur on both sides of the spectrum, as well as for isolated and overlapping ro-vibrational lines. Starting with Figure 5.4(a) and its modeled counterpart in Figure 5.4(b), convolved P(7) and O(4) ro-vibrational lines are centered at  $1610 \text{ cm}^{-1}$  with pronounced coherence beating until the line splits at a probe delay of 80 ps. In Figures 5.4(c) and (d), an isolated O(8) line at  $1700 \text{ cm}^{-1}$  initially behaves as a sinusoidal pattern, undergoes line splitting at  $\tau_{pr} = 60$  ps, then returns to its initial behavior for the rest of the probe delay duration. Two examples from the R- and S-branch spectra are provided as well: an isolated R(5) line at  $1472 \text{ cm}^{-1}$  in Figure 5.4(e),(f) and convolved R(2) and S(0) lines located at  $1502 \text{ cm}^{-1}$  in Figure 5.4(g),(h).

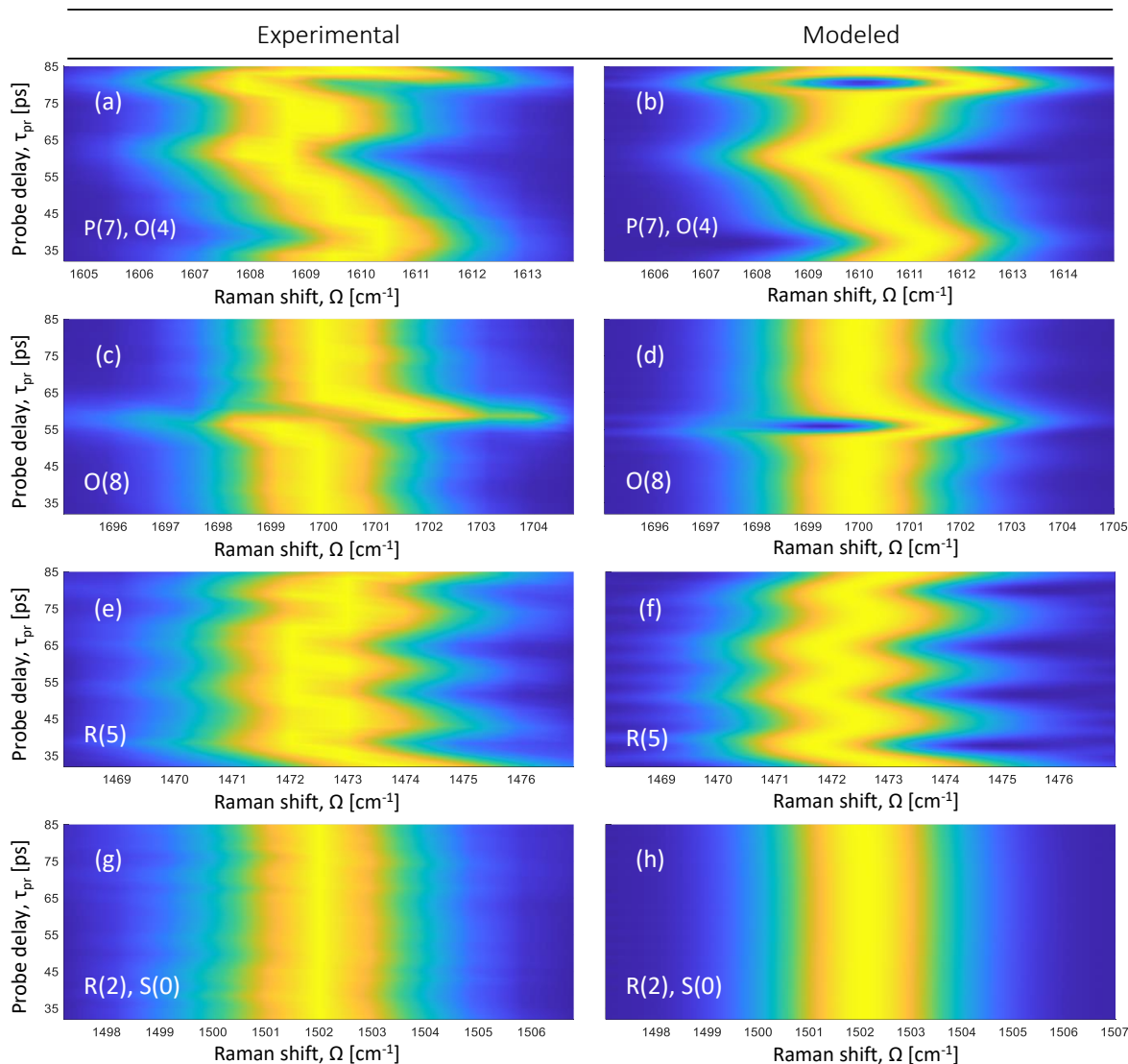


Figure 5.4: Spectrograms selected from the S-, R-, P-, and O-branches of the  $\text{CH}_4 \nu_2$  spectrum comparing experimental CRS measurements with modeled ro-vibrational lines. (a) Experimental spectrogram of the convolved P(7) and O(4) lines. (b) Modeled spectrogram of the convolved P(7) and O(4) lines. (c) Experimental spectrogram of the O(8) line in the O-branch spectrum. (d) Modeled spectrogram of the O(8) line in the O-branch spectrum. (e) Experimental spectrogram of the R(5) line in the R-branch spectrum. (f) Modeled spectrogram of the R(5) line in the R-branch spectrum. (g) Experimental spectrogram of the convolved R(2) and S(0) lines. (h) Modeled spectrogram of the convolved R(2) and S(0) lines. Individual spectral lines are normalized to their own maximum intensity to better visualize their behavior.

Spectral branch overlaps occur for every other line in the P- and R-branch spectra due to the separation of the rotational lines in these branches (2B) and in the O- and S- branches (4B). In these instances,

the result of the overlap is expected to vary with a sinusoidal beating pattern corresponding to interference between the two lines, as seen in Figure 5.4(g),(h) where the R- and S- branches overlap. For Figure 5.4(a),(b) the P- and O-branches also overlap, but differ from the beating observed in Figure 5.4(g),(h) by substantial shifting of the peak across  $1610\text{ cm}^{-1}$  and the previously described line splitting. While completely isolated lines can produce simple beating, such as O(9) at  $1723\text{ cm}^{-1}$ , some isolated lines exhibit significant coherence beating beyond a lone sinusoidal pattern. This beating is displayed in Figures 5.4(c),(d) and (e),(f) which show isolated O(8) and R(5) lines, respectively. From the beating patterns of isolated O(8) and R(5) lines, along with the convolved P(7)-O(4) line beating, it can be determined that there are further contributing effects other than unresolved overlapping lines or vibrational hot bands.

With the potential effects of other contributions ruled out, the dramatic coherence beating patterns seen in Figure 5.4 result from intra-molecular interaction and coupling. For a quantum system, the degeneracy of an energy level is related to the symmetry of the molecule and its wave function. However, when perturbed through an external field or coupling, the symmetry can be broken and results in the splitting of the degenerate level into many distinct energy levels instead, as seen in [88]. Furthermore, energy level-splitting is relevant to the  $\text{CH}_4$   $\nu_2$  mode Raman spectrum where the doubly degenerate  $\nu_2$  mode is coupled to the  $\nu_4$  mode through Coriolis interaction, depicted in Figure 5.5 [91]. Through the Coriolis coupling the degeneracy related to the total angular momentum quantum number  $J$  and its ro-vibrational energy is lifted, leading to distinct rotational sub-states which are convolved into the beating pattern. This is supported through the close replication of experimental coherence beating by the time-domain CRS model such as for the Q-branch spectrum in Figure 5.3(b) which involves only 558 lines and rotational states up to  $J=23$ , resulting from the inclusion of the Coriolis coupling of the fundamental  $\nu_2$  and  $\nu_4$  modes in the spectral database [92, 93].

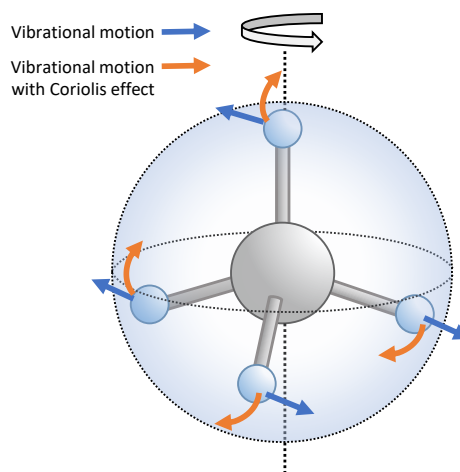


Figure 5.5: Coriolis effect on the  $\text{CH}_4$   $\nu_2$  vibrational mode. As a result of vibrations, the atoms of  $\text{CH}_4$  are moving relative to the rotating coordinate system. Blue arrows depict the original vibrational motion, while orange arrows depict the contributions of the Coriolis effect.

## 5.2. Linewidth measurements

At longer dephasing timescales inelastic collisions between molecules become relevant and cause rotational energy transfer, changing the amount of coherent molecules and the CRS signal strength as a function of time. In this way collisions act as a damping mechanism and manifest as a time-domain decay constant or frequency-domain linewidth for a given Raman transition, as identified in Equation 3.6. Raman linewidths are notably affected by thermodynamic properties that govern the rate of collisions, such as pressure and temperature, and the efficiency of the rotational energy transfer process in each collision, leading to dependence on chemical composition. To account for these effects on the  $\text{CH}_4$   $\nu_2$  dephasing, a modified exponential gap (MEG) scaling law is implemented in the time-domain CRS model and described in Equations 3.12, 3.13, and 3.14.

The MEG scaling law is commonly applied to calculate collisional linewidths for time-resolved CRS techniques and involves four fitting parameters  $\alpha$ ,  $\beta$ ,  $\delta$ , and  $n$ , which adjust the contributions of the pressure, temperature, and energy gap between the two considered states. The predominant collision energy transfer is assumed to be rotational due to the large energy gaps between vibrational and electronic states [94]. The MEG model assumes an exponential dependence of linewidth on the energy gap between rotational sublevels, a linear relationship to pressure, and a complicated dependence on temperature-dependent terms. Because the rate of energy transfer is exponentially dependent on the energy gap between initial and final states, higher rotational energy states will result in decreasing energy transfer rates, or linewidth values, and decay more slowly than lower rotational states [81]. Furthermore, the rate of energy transfer is modified by two temperature-dependent terms: a temperature ratio taken to power  $n$  to reproduce high-temperature rates and a complex empirical term relating

rotational energy, temperature, and fitting parameter  $\delta$  [95].

To reduce the number of simulated spectra required for fitting it is possible to simplify the MEG model and its four fitting parameters. For  $\text{CH}_4$   $\nu_1$  Q-branch modeling in [61], room temperature spectra were used to first optimize parameters  $\alpha$  and  $\beta$  while the parameters involved with high-temperature corrections were set to  $\delta = 1$  and  $n = 0$ . The optimized parameters were then used for fitting  $\delta$  and  $n$  with high temperature spectra, resulting in two fitted linewidth models validated for different temperature ranges. Since the  $\text{CH}_4$   $\nu_2$  probe delay scan was conducted at room temperature a similar approach to [61] is taken for the MEG model, albeit truncated, with  $\delta = 1$  and  $n = 0$  while parameters  $\alpha$  and  $\beta$  are varied during library generation.

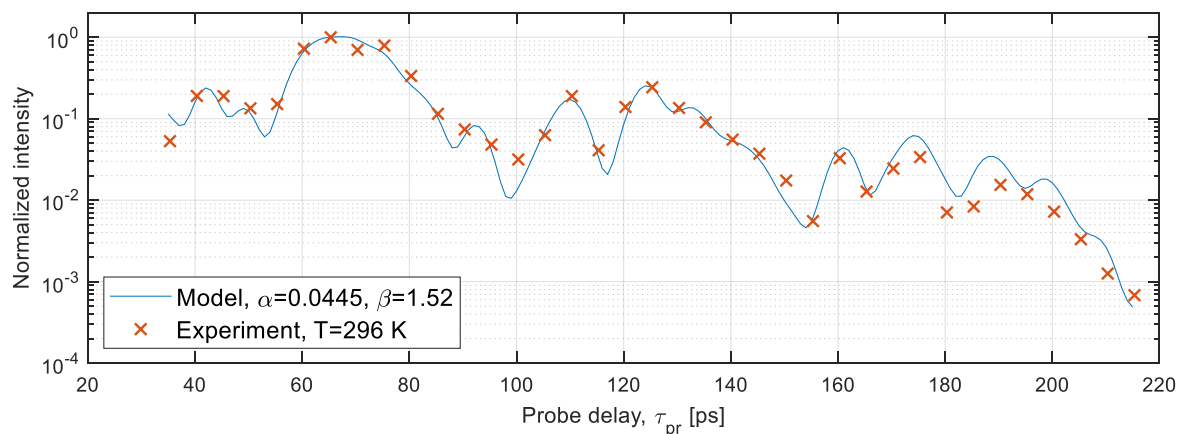


Figure 5.6: Collisional dephasing of the  $\text{CH}_4$   $\nu_2$  Q-branch CRS signal. Experimental  $\nu_2$  CRS spectra were acquired between  $\tau_{pr}=35$  and  $\tau_{pr}=220$  ps for room temperature and atmospheric pressure. The Q-branch ( $\Delta J = 0$ ) peak was isolated and summed for fitting in the time-domain. MEG linewidth parameters were determined through a least-squares fitting routine with  $\alpha=0.0445$  and  $\beta=1.52$ .

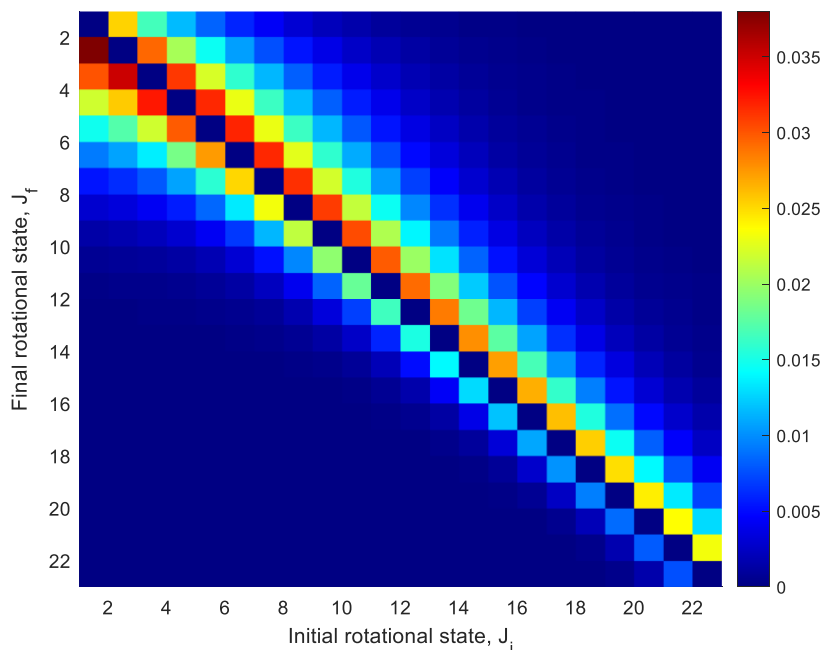


Figure 5.7: Calculated transition rate matrix from  $\nu_2$  Q-branch MEG fit at 296 K and 1 atm. Only rotational states from  $J=1$  to  $J=23$  are included as a result of the database filtering. The intensity of an element represents the rate of transition between its respective states. The total matrix is separated into two parts: an upper triangle corresponding to transitions from a higher rotational state to lower state (Equation 3.12) and a lower triangle corresponding to transitions from a lower rotational state to a higher one (Equation 3.13).

Figure 5.6 shows the experimental probe delay scan of the  $\text{CH}_4 \nu_2$  Q-branch alongside the result of fitting the MEG model in the time-domain. Overall, the experimental Q-branch intensity beating across the probe delay is effectively duplicated by the Q-branch synthetic dephasing with parameters  $\alpha=0.0445$  and  $\beta=1.52$ . Collisional beating is almost exactly reproduced for the first 150 ps, after which the synthetic beating contains the same behavior but begins to deviate slightly from experimental data. This could be attributed to the decrease of the signal-to-background ratio of the spectra which becomes more pronounced at longer probe delays. Furthermore, the comparison reinforces that inclusion of only fundamental  $\nu_2$  mode transitions and further intensity-based cutoff leaves an adequate amount of Raman lines for the time-domain CRS model.

In addition, it is interesting to consider the transition rate matrix resulting from the MEG fitting shown in Figure 5.7, including rotational states from  $J=1$  to  $J=23$ . The matrix is separated into two components: an upper triangle calculated from Equation 3.12 representing upwards transitions from a lower rotational state to a higher state ( $J_i \rightarrow J_j$ ) and a lower triangle calculated from Equation 3.13 representing downward transitions from a higher rotational state to a lower state ( $J_i \leftarrow J_j$ ). The diagonal elements of the matrix are zero since there cannot be a transition between molecules in the same rotational state. The total rate of collisional energy transfer for an initial rotational state  $J_i$  is obtained by summing each column in the matrix according to Equation 3.14, including transitions both upwards and downwards on the rotational energy ladder.

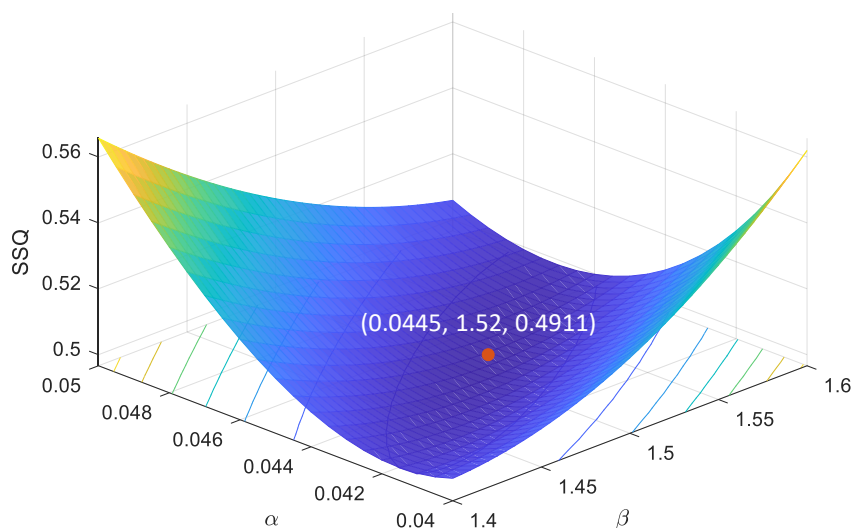


Figure 5.8: Evaluated sum of squares (SSQ) values across generated library entries, represented as an optimization surface as a function of the two fitting parameters  $\alpha$  and  $\beta$ .

While the main procedure for fitting routine is presented in Section 3.4, a few observations are made for the optimization of the MEG parameters  $\alpha$  and  $\beta$ . For the initial approach to least-squares fitting, library generation was very coarse to ensure that relevant parameter values were not excluded. The optimal coarse fit approached the lower bound of  $\alpha$ , so another coarse library was generated with  $\alpha$  between 0.01 and 0.15, within the magnitudes of the  $\alpha$  values reported in [61]. After further refinement, the surface of evaluated SSQ values began to resemble a valley of minima or uni-modal optimization surface. The SSQ surface for the final fit is shown in Figure 5.8, with a marked minimum value containing the optimized MEG parameters.

One last consideration for MEG fitting is the applied scaling between the two acquisition sets of the probe delay scan. In addition to the scalar division to the latter half of the probe delay, Section 4.3 explains how the doubly-acquired point in the probe delay is used to create a scaling factor as an alternative to the initial scaling method. This resulted in slightly lower intensity values, as shown in Figure 5.9, where the original Q-branch intensity and the outcome of the two scaling methods are compared. These two methods had only a minor effect in the outcome of the MEG fitting, where the double-acquisition scaling was fit with only a 0.7% difference for  $\beta$  and no change in  $\alpha$ . While sufficient for the Q-branch, other isolated peaks may be more affected by the non-uniform scaling factor.

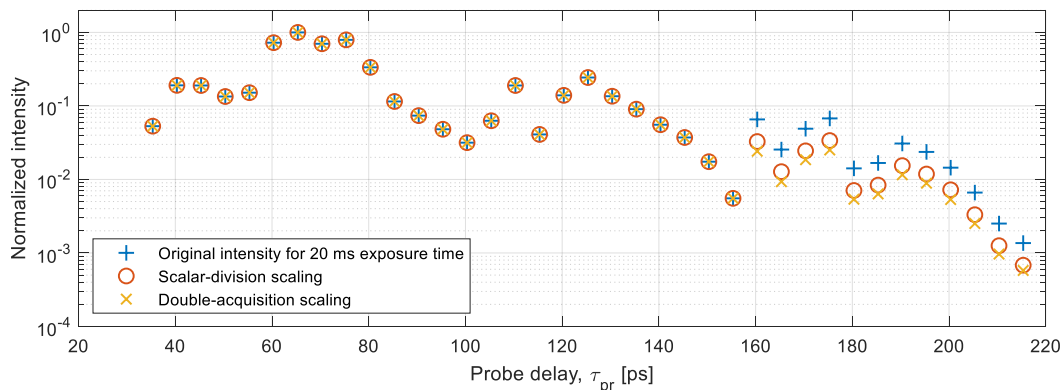


Figure 5.9: Comparison between scaling methods for the latter half of collisional dephasing measurements of the  $\text{CH}_4$   $\nu_2$  Q-branch. Up to the first 160 ps, data points with 10 ms exposure time remain the same. At 160 ps the differences between the scaling methods and the original intensity are observable.

Although the current results of the model match quite well with experimental data, there are still limits and assumptions affecting the applicability of the MEG model for calculating collisional transfer rates. The main limit of the model is the lack of validation under more extensive experimental conditions. Validation at a wider range of pressures and temperatures can provide further understanding of the linewidth behavior and dependencies. For the pressure and high-temperature measurements in [61], all four MEG parameters were utilized and parameter  $\alpha$  was found to have a non-constant value across different pressures. In addition, the probe delay scans of [61] extended well-past the 220 ps achieved in this thesis. This is mainly attributable to the difference in Raman scattering cross-sections between the  $\nu_1$  and  $\nu_2$  modes, but longer probe delays for  $\nu_2$  could potentially be measured using longer exposure times from the outset of the experiments.

Furthermore, several assumptions were included in the modeling of the linewidths for anisotropic, vibrationally degenerate  $\text{CH}_4$   $\nu_2$  Raman transitions. The main assumptions to acknowledge with regards to the applicability of the MEG model are based on the symmetry of ro-vibrational states and the state-to-state collisional dephasing processes. Symmetry is foundational for molecular spectroscopy because it constrains possible forms of the molecular wave function and determines selection and intensity rules; a visual representation of the molecular wave function is given for harmonic vibrational states in Figure 2.3. Methane is a high symmetry molecule belonging to the tetrahedral point group  $T_d$ ; its total wave function  $\Psi$  can be represented as the product of separable functions under the Born-Oppenheimer approximation:

$$\Psi = \Psi_T \Psi_E \Psi_V \Psi_R \Psi_S \quad (5.1)$$

where  $\Psi_T$  is the translational wave function,  $\Psi_E$  electronic wave function,  $\Psi_V$  vibrational wave function,  $\Psi_R$  rotational wave function, and  $\Psi_S$  nuclear spin wave function. Both the translational  $\Psi_T$  and electronic  $\Psi_E$  wave functions are completely symmetric in the electronic ground state, designated as  $A$ . The vibrational wave function symmetry is restricted by the minimal set of possible representations, or irreducible representations, for point group  $T_d$ , resulting in the previously discussed fundamental  $\text{CH}_4$  vibrational modes. In addition to defining rotational states with quantum number  $J$ , the total angular momentum projection with respect to an inertial frame is specified using quantum number  $M$ . The rotational wave function of  $\text{CH}_4$  is also constrained by the tetrahedral symmetry of the molecule, resulting in it being further defined by linearly combining symmetries  $A$ ,  $E$ , and  $F$  irreducible representations, whose dimensions and degeneracies are given in Table 5.1 [96]. The  $\text{CH}_4$  nuclear spin wave function is determined by symmetry through the linear combination  $5A + E + 3F$  which yields 16 possible spin states. Under Pauli's exclusion principle, the global wave function of  $\text{CH}_4$  is constrained to have  $A$  symmetry. This main constraining symmetry determines both the allowed transitions and wave functions (i.e. combinations of ro-vibrational motion of nuclei with spin and electron energy), affecting the statistical weighting of ro-vibrational population distributions.

These symmetry restrictions for  $\text{CH}_4$  also have implications for the assumptions made during collisional linewidth modeling. In this thesis, the linewidths for the same quantum number  $J$  but of different nuclear

$T_d$	Representation
A	1D (non-degenerate)
E	2D (doubly-degenerate)
F	3D (triply-degenerate)

Table 5.1: Point group  $T_d$  irreducible representations and associated spatial dimensions and degeneracy.

spin (A, E, or F) were assumed to be the same and entered the time-domain response calculation without nuclear spin specificity. The assumption was also made in [61] during linewidth modeling of the isotropic  $\text{CH}_4 \nu_1$  Q-branch. While it is important to state this assumption, its effect is ultimately negligible on the collisional linewidth model and the agreement with experimental data. Additionally, the linewidth model neglects rotational wave function symmetry, meaning that the computed linewidth for a rotational quantum number  $J$  is used regardless of its symmetry components similar to the nuclear spin wave function.

Finally, the sum rule in Equation 3.14 is not exactly applicable for the  $\text{CH}_4 \nu_2$  spectrum because of its anisotropic transitions and degenerate states, requiring further considerations when modeling inelastic collisions and line coupling [97, 98]. By neglecting these additional aspects, the determined  $\text{CH}_4 \nu_2$  collisional linewidths are only a first approximation. This has been proven to be adequate for modeling the P- and R- branch linewidths of  $\text{CO}_2$  absorption spectra [99]. Because the experiments were conducted only under ambient conditions, neglecting molecular reorientation from collisions and intra-branch coupling while using the MEG model as a first approximation for the  $\text{CH}_4 \nu_2$  Q-branch spectrum dephasing is justified, as was found for measurements of the  $\text{N}_2$  Raman Q-branch [100]. However, additional approaches for analysis of anisotropic, tetrahedral molecules exist and could be implemented to extend the applicability of the model for  $\text{CH}_4 \nu_2$  spectra [101, 102].

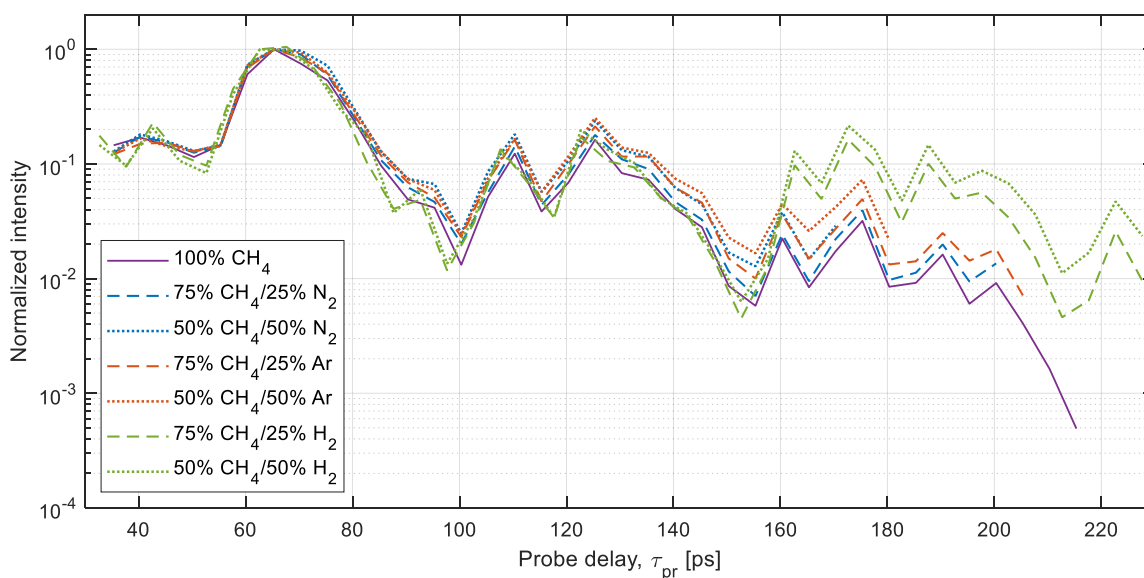


Figure 5.10: Probe delay scans of the  $\text{CH}_4 \nu_2$  Q-branch for varying  $\text{CH}_4$ -gas mixtures at  $T = 296$  K and atmospheric pressure. Three different colliding partners  $\text{N}_2$ , Ar, and  $\text{H}_2$  are mixed with  $\text{CH}_4$  for 25% and 50% of the gas flow. All measurements are normalized to their intensity at  $\tau_{pr}$  for comparison of their time-domain beating behavior.

To further characterize the dephasing behavior of the  $\text{CH}_4 \nu_2$  mode, it is necessary to measure the effect of different collisional partners, particularly those relevant to combustion. For this purpose, several probe delay scans were conducted for different gas mixtures of  $\text{CH}_4$  with nitrogen, argon, and hydrogen at room temperature and atmospheric pressure. An initial measurement of pure methane was acquired as a control while an increasing percentage of the gas flow was substituted with either  $\text{N}_2$ , Ar, or  $\text{H}_2$  for subsequent probe delay scans, as detailed further in Section 4.2. Like previous collisional dephasing measurements, the  $\text{CH}_4 \nu_2$  Q-branch was isolated and summed at each probe delay. In Figure 5.10, the collisional dephasing measurements for all experimental conditions are presented for comparison,

extending from 35 to 230 ps as a whole. The same measurements are separated by gas mixture in Figure 5.11 for clarity.

As seen in Figure 5.10, the general features of coherence beating are shared for all gas mixtures but the overall rate decay rate is influenced by the colliding perturbers. The effects of mixture composition are most noticeable after a probe delay of approximately 80 ps, also called the critical probe delay for collisional partner independence. An estimation of the timescale for the critical probe delay can be calculated and compared with experimental observations using the kinetic theory of gases. The probability that a molecule survives  $t$  seconds without any collision is  $\exp(-t/\tau)$  where  $\tau$  is the mean time between collisions, calculated to be 100 ps for  $\text{CH}_4$  under standard conditions. For a probability of 50% the corresponding probe delay is 69 ps, however, this is well-before the time-domain measurements begin to deviate. At the critical probe delay of 80 ps, this probability drops to 45% and more than half of the considered molecules have collided. This agrees fairly well with the plots in Figure 5.11, where the dephasing of all gases are nearly overlaid with the pure  $\text{CH}_4$  dephasing until  $\tau_{pr} = 80$  ps. It is worth noting that despite the initial divergences at 80 ps, the dephasing lines of the diluted gas flows remain closely parallel to the pure methane flow until approximately 125 ps where the probability of finding a collision-free molecule has fallen to 29%. This timescale is defined as the ‘‘collision sensitivity time’’ in [61], indicating that there is a weak influence of collisional partners on the CRS dephasing.

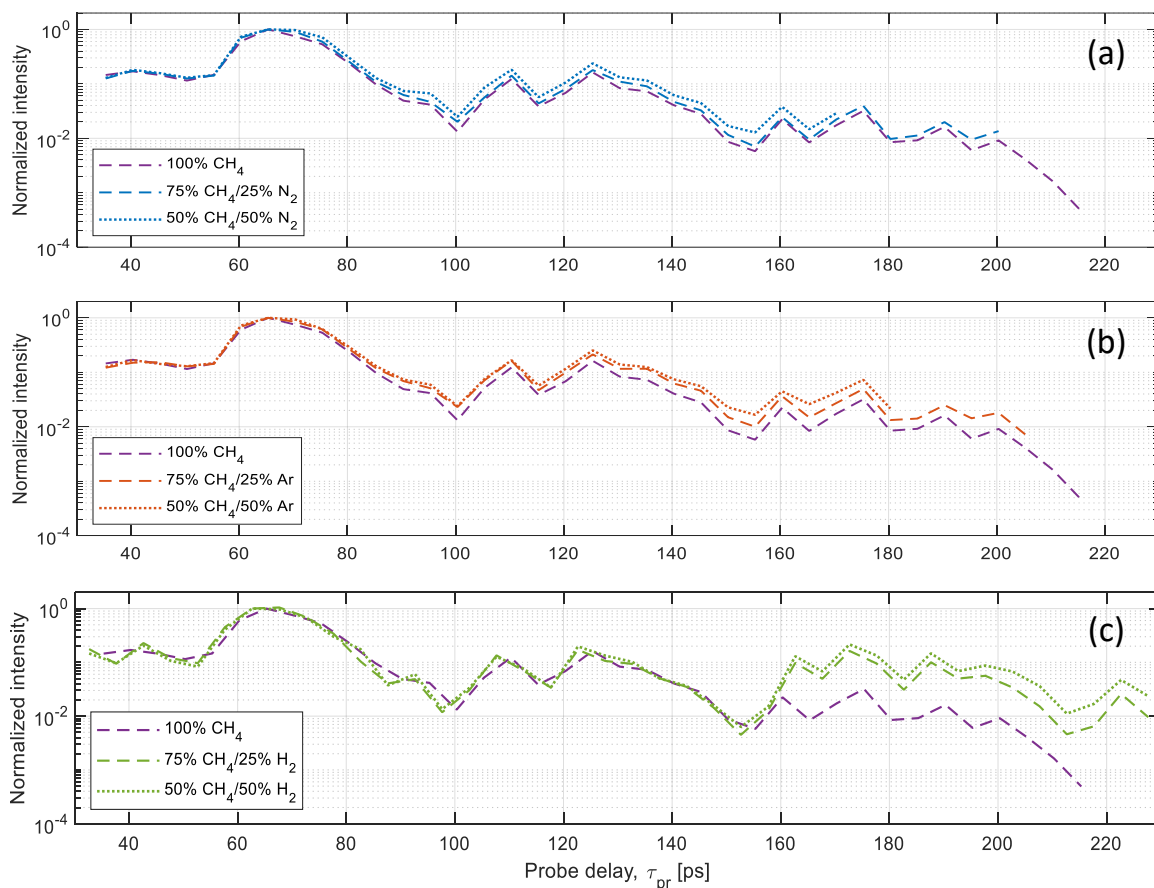


Figure 5.11: Separated probe delay scans for  $\text{CH}_4$   $\nu_2$  Q-branch under gas mixtures with  $\text{N}_2$ , Ar, and  $\text{H}_2$ . The same pure  $\text{CH}_4$  probe delay scan is shown in each sub-figure for comparison. The extent of the measured dephasing timescale is different for each case due to the rate of decay in signal intensity for each mixtures. (a) Collisional dephasing for 75%/25% and 50%/50% gas mixtures of  $\text{CH}_4$ - $\text{N}_2$ , respectively. (b) Collisional dephasing for 75%/25% and 50%/50% gas mixtures of  $\text{CH}_4$ -Ar. (c) Collisional dephasing for 75%/25% and 50%/50% gas mixtures of  $\text{CH}_4$ - $\text{H}_2$ .

More qualitative comparisons can be made between gas mixtures to analyze the collisional partner dependence on the dephasing of the  $\text{CH}_4$   $\nu_2$  mode. In Figure 5.11, the differences between  $\text{N}_2$ , Ar, and  $\text{H}_2$  are more prominent;  $\text{N}_2$  results in the shortest probe delay scan ending at 170 ps while  $\text{H}_2$  has the longest probe delay at 230 ps. Past the critical probe delay  $\text{CH}_4$ / $\text{H}_2$  mixtures lead to the largest

decrease in the dephasing rate, followed then by CH<sub>4</sub>/Ar and CH<sub>4</sub>/N<sub>2</sub> gas mixtures. These dephasing distinctions are due to the energy transfer process between the rotational structures of the two considered molecules, the observed radiator and the perturber. If the colliding partners are identical, such as CH<sub>4</sub>/CH<sub>4</sub>, then the neighboring rotational states of the radiator and perturber are as well and result in a higher probability of energy transfer during a collision. In the case of two different collisional partners like CH<sub>4</sub> and H<sub>2</sub>, there are more disparities between the neighboring rotational states which reduces the energy transfer and decay of the beating pattern. A diagram of this process is provided in Figure 5.12 where the distribution of rotational state energies are given for CH<sub>4</sub> and H<sub>2</sub>. The differences in the energy gaps of the molecules are due to their rotational constants: for CH<sub>4</sub> its constant is  $B = 5.24 \text{ cm}^{-1}$ , N<sub>2</sub> has  $B = 1.99 \text{ cm}^{-1}$ , and for H<sub>2</sub> its constant is  $B = 60.8 \text{ cm}^{-1}$ . The differences in rotational constants are also reflected in Figure 5.11, where the CH<sub>4</sub>/N<sub>2</sub> dephasing is the closest to the pure CH<sub>4</sub> dephasing ( $5.24 \text{ cm}^{-1}$  vs.  $1.99 \text{ cm}^{-1}$ ) and the CH<sub>4</sub>/H<sub>2</sub> deviates the most ( $5.24 \text{ cm}^{-1}$  vs.  $60.8 \text{ cm}^{-1}$ ).

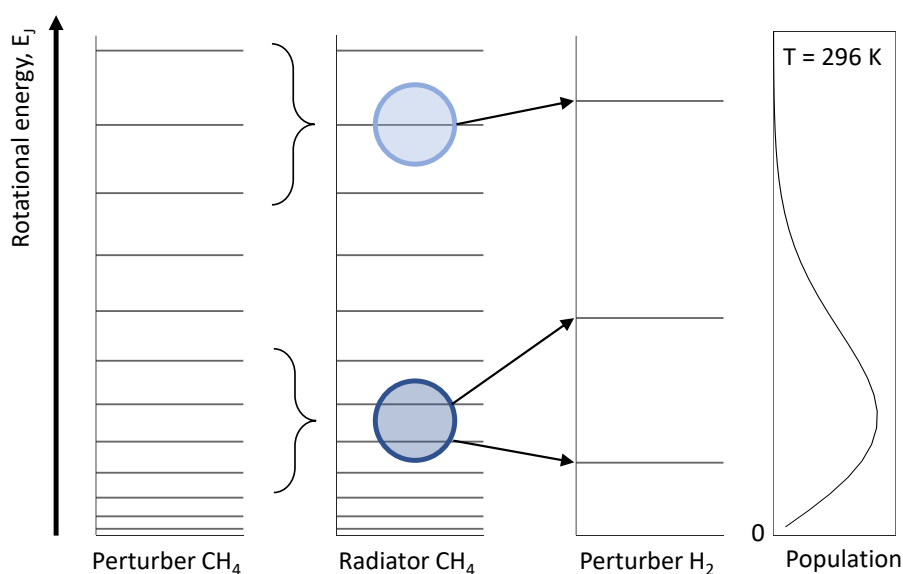


Figure 5.12: Collisionally induced rotational energy transfer process between a radiator CH<sub>4</sub> and different perturbers CH<sub>4</sub> and H<sub>2</sub>. With more adjacent states between the radiator and perturber, the energy transfer process is more likely.

### 5.3. CH<sub>4</sub>/air flame measurements

Under ambient conditions the time-domain behavior and collisional dephasing of the CH<sub>4</sub>  $\nu_2$  mode has been characterized. The eventual goal of developing time- and frequency-resolved spectroscopy for the  $\nu_2$  mode is the application of this knowledge to combustion and gas diagnostics. The spectral range of the  $\nu_2$  mode is deemed as a molecular “fingerprint” region where most molecular species have uniquely identifiable vibrational spectra, making it an appealing focus of investigation for potential quantitative temperature and concentration measurements. This section presents and discusses spatially resolved CRS measurements taken in a CH<sub>4</sub>/air diffusion flame for this purpose.

Although the procedure for flame measurements has been introduced in Section 4.2, a brief summary will be provided to contextualize the results. Point measurements were taken in steps of 0.5 mm across the flame front of a laminar CH<sub>4</sub>/air diffusion flame, resulting in 25 measured locations from the fuel to oxidizer as seen in Figure 4.3. While single-shot spectra were acquired in the fuel stream at the center of the burner, the intensity of the CH<sub>4</sub>  $\nu_2$  CRS signal degraded as the reaction zone of the flame front was approached. To ensure complete detection of the  $\nu_2$  mode without the interference of temperature the acquisition of all measurements was changed to a 10-shot-average, resulting in spectra with very good signal-to-background ratios needing minimal processing.

In Figure 5.13, the CRS spectra are plotted along the transverse position of the flame. There are several spectral structures which indicate the three main regions of the flame: the fuel flow (a), reaction zone (b), and oxidizer flow (c). Within the molecular fingerprint region, the spectra are attributed to four different

species: the  $\text{CH}_4$  ro-vibrational  $\nu_2$  spectrum (1400 to 1950  $\text{cm}^{-1}$ ), the  $\text{CO}_2$  Fermi dyad (Q-branches at 1285 and 1388  $\text{cm}^{-1}$ ), four pure-rotational lines of  $\text{H}_2$  (O-branch lines at 1246, 1447, 1637, and 1815  $\text{cm}^{-1}$ ), and the  $\text{O}_2$  ro-vibrational spectrum (1400 to 1700  $\text{cm}^{-1}$ ). In addition to the overall spectra, specific slices were chosen from the three main regions and shown in Figure 5.14 for a closer look at the physical-chemical processes taking place.

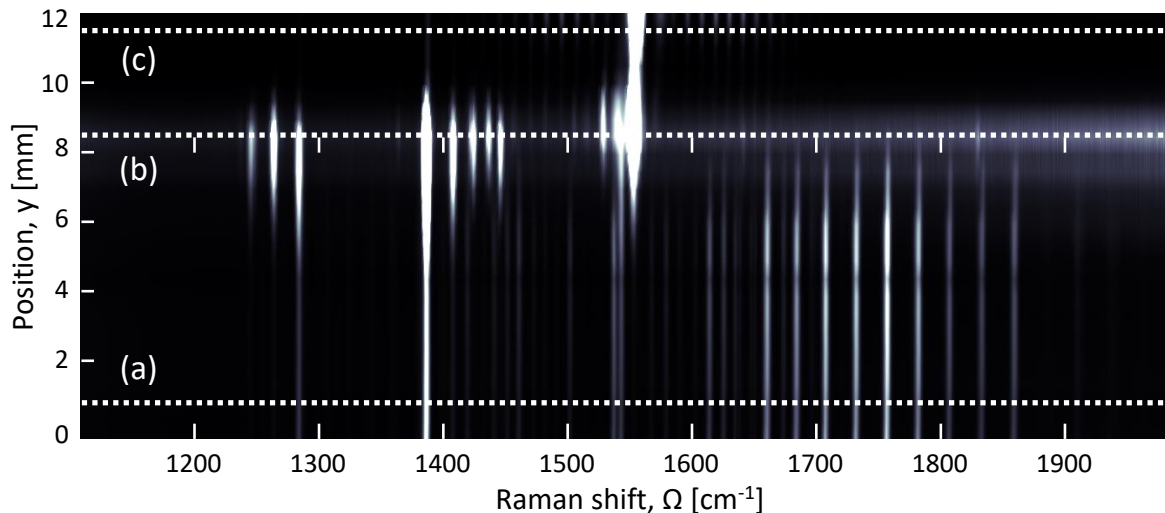


Figure 5.13: CRS spectra acquired across a laminar  $\text{CH}_4/\text{air}$  diffusion flame. Three labeled slices of the spatially resolved measurements are shown with greater detail in Figure 5.14. All spectra were acquired with a probe delay of  $\tau_{pr}$ . Because of the overwhelming intensity of the  $\text{O}_2$  Q-branch, it was necessary to compress the color-scale (Gamma compression) during post-processing to reveal other spectral features.

Starting in sequence with the measurements, the first spectrum shown in Figure 5.14(a) is that of the fuel flow from the center of the burner at  $y=0$  mm to the beginning of the reaction zone around  $y=4$  mm. While the ro-vibrational lines of the  $\text{CH}_4$   $\nu_2$  mode are clearly visible in this range, they are overshadowed by the  $\text{CO}_2$  “blue” Q-branch centered at 1388  $\text{cm}^{-1}$  as part of the Fermi dyad [90]. Due to the relative molecular masses of  $\text{CH}_4$  and  $\text{CO}_2$  ( $M_{\text{CH}_4} = 16$  versus  $M_{\text{CO}_2} = 44$ ), the center of the fuel flow experiences a buoyancy effect with the  $\text{CO}_2$  produced from the reaction zone and the  $\text{CO}_2$  undergoes internal recirculation. Furthermore, mixing of the fuel and oxidizer is observed with the ro-vibrational  $\text{O}_2$  Q-branch peak appearing at 1556  $\text{cm}^{-1}$ .

The reaction zone spectrum is fully discernable at the position of  $y=8.5$  mm and presented in Figure 5.14(b). Here, the most prominent lines are the Q-branches of  $\text{O}_2$  and  $\text{CO}_2$ , followed by four lines of the  $\text{H}_2$  O-branch; the ro-vibrational spectrum of  $\text{CH}_4$   $\nu_2$  mode is no longer visible. In this zone, the heat of the combustion reaction causes the pyrolysis of the  $\text{CH}_4$  fuel. The resulting radicals are used in the synthesis of the  $\text{H}_2$ , with its peaks showing up in Figure 5.14(b). The lack of the  $\text{H}_2$  O-branch peaks at approximately  $y=9$  mm indicates that the hydrogen is consumed in the reaction soon after. Furthermore, the heat release and resulting temperature increase can be seen through the hot bands of  $\text{CO}_2$  and particularly  $\text{O}_2$ .

Finally, in Figure 5.14(c) the spectrum of the oxidizer flow is given and primarily consists of the ro-vibrational  $\text{O}_2$  spectrum accompanied by a much smaller amount of  $\text{CO}_2$  as the result of mass diffusion. The ambient air supply also decreases the temperature of the spectral lines, shown by the growth in magnitude of the low-temperature  $\text{O}_2$  spectra. One point of significance is the  $\text{CO}_2$  presence far within the fuel flow of the flame. Because of its relatively large specific heat capacity, the observed  $\text{CO}_2$  recirculation within the flame is predicted to affect the heat transfer and combustion process. Overall, the appearance of the four discussed chemical species is invaluable for fuel and oxidizer tracking and contributes to the understanding of complex chemical reaction mechanisms.

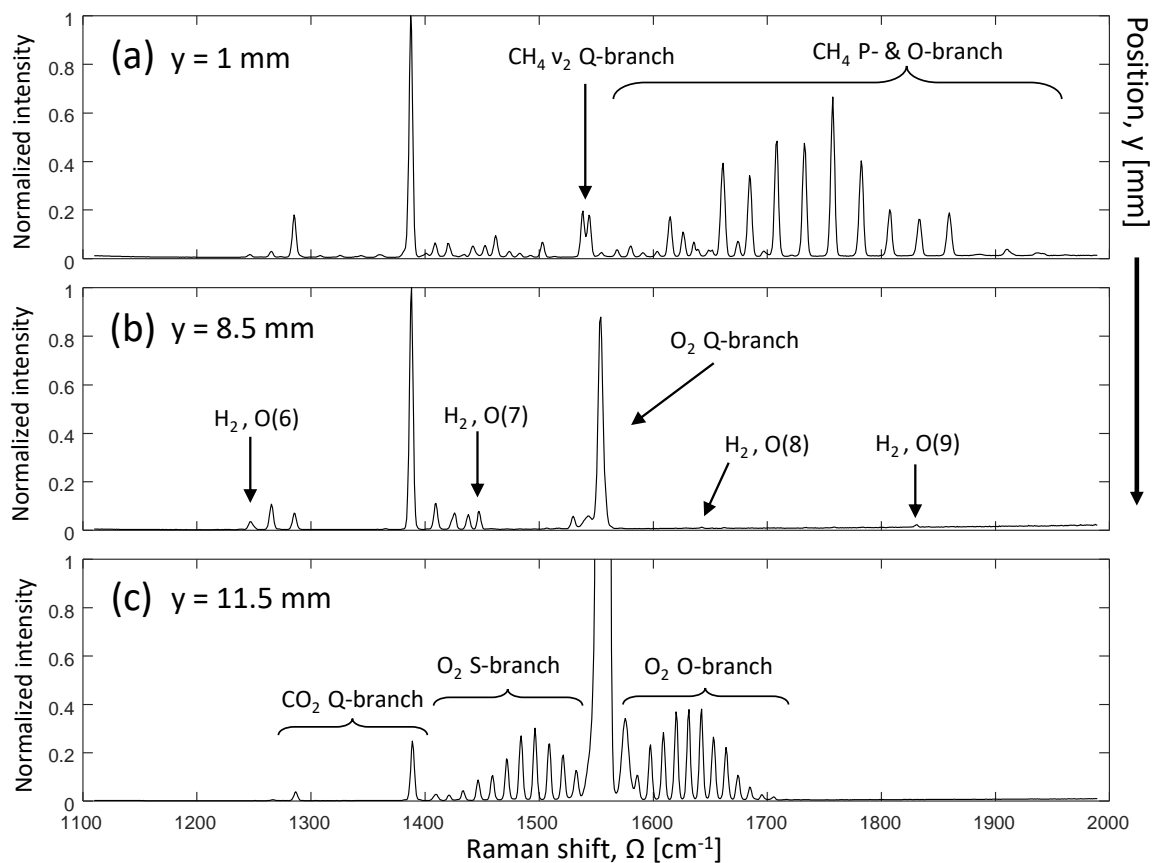


Figure 5.14: Three spectral slices in the molecular fingerprint region containing the CH<sub>4</sub>  $\nu_2$  mode. Each spectrum is acquired at a different location in the flame. (a) Fuel flow at burner center ( $y=1$  mm) containing the full spectrum of CH<sub>4</sub>  $\nu_2$  and ro-vibrational peaks of CO<sub>2</sub>. (b) Reaction zone ( $y=8.5$  mm) where several species such as H<sub>2</sub>, O<sub>2</sub>, and CO<sub>2</sub> are present, with a vast range of intensities indicating increased temperature. (c) Oxidizer flow ( $y=11.5$  mm) displaying spectral branches of both O<sub>2</sub> and CO<sub>2</sub>.



# 6

## Conclusions and Recommendations

The purpose of this thesis was the measurement and analysis of the  $\text{CH}_4$   $\nu_2$  mode using time- and frequency-resolved fs/ps coherent Raman scattering. The interest in characterizing methane spectra generally lies in its importance to both energy generation and climate change. While often overlooked in favor of the  $\nu_1$  mode, the appeal of the  $\nu_2$  specifically is found in its distinctive ro-vibrational structure along with its spectral location in a “molecular fingerprint” region. In Chapter 2, theoretical background for molecular spectra, coherent Raman scattering, and time-resolved CRS spectroscopy was provided to give context to the subsequent work.

Next, Chapter 3 was focused on the time-domain modeling of the  $\text{CH}_4$   $\nu_2$  mode. Beginning with the context of general spectroscopy of methane, mainly of the  $\nu_1$  mode, the first section narrows down to previous studies of the  $\nu_2$  mode specifically and identifies the gap in literature that the thesis aims to fill. Then, the modeling approach is described for the time-domain response of  $\text{CH}_4$   $\nu_2$  after its induced polarization by the excitation pulses; this includes the introduction of the modified exponential gap (MEG) scaling law applied to model the collisional energy transfer linewidths of rotational  $\nu_2$  states. The spectral Raman database MeCaSDa was described in addition to the necessary adjustments made, such that the line information was made relevant to the coherent scattering process. Last, the theoretical library and fitting routine process for extracting Raman linewidths characteristic to the  $\nu_2$  time-domain dephasing behavior was explained.

Chapter 4 features the experimental methodology: the laboratory setup, the experimental procedure, and the measurement processing performed to assure consistency and quality of acquired spectra. The experimental setup implemented a two-beam hybrid fs/ps CRS system for acquisitions of time- and frequency-resolved measurements. This setup was employed for three main components of the experimental campaign: time-resolved single-shot measurements of the  $\text{CH}_4$   $\nu_2$  spectrum for a collision-free timescale, collisional dephasing measurements of the spectrum on its own and with gas mixtures, and spatially resolved spectrum measurements across a laminar flame-front to assess its diagnostic potential. The main measurement procedure consisted of a “probe delay scan” where the relative timing of the pump/Stokes and probe pulses is varied to acquire the time-domain behavior of the frequency-resolved spectrum, repeated for all time-resolved measurements. The chapter closes with the format of the acquired measurements and explanations of the background subtract, binning, calibration, baseline correction, and intensity reconciliation processing steps.

In the first experiment, time-domain measurements were obtained for the  $\text{CH}_4$   $\nu_2$  CSRS spectrum containing all five ro-vibrational branches. All spectral lines were observed to have intensity “beating” as the dephasing unfolded in the time domain, but the source of the coherence beating was attributed to a combination of different effects. As an example, the complex beating pattern of the convolved Q-branch peak results from the closely spaced  $\Delta J = 0$  transitions which cannot be resolved by the  $4.1 \text{ cm}^{-1}$  probe bandwidth. Moreover, various beating features of the S-, R-, O-, and P-branches are interpreted as the effects of branch overlap and degenerate energy level splitting. All experimental results were well-reproduced by the time-domain CRS model, capturing the main features of the beating

while neglecting hot bands and applying a transition intensity cutoff.

For the second set of experiments, the  $\text{CH}_4 \nu_2$  spectrum was measured for a longer timescale to measure the collisional dephasing of the CRS signal with gas flows of pure  $\text{CH}_4$  and  $\text{CH}_4$  mixtures. The MEG model used to calculate the collisional linewidths of the state-to-state energy transfer for the  $\nu_2$  Q-branch. The MEG parameters were reduced to  $\alpha$  and  $\beta$  to reduce the number of spectra needed for fitting. After library generation and least-squares fitting, the linewidth parameters were found to be  $\alpha = 0.0445$  and  $\beta = 1.52$  with a satisfactory fit to the experimental Q-branch dephasing.

In addition, time-resolved measurements were acquired for gas mixtures of  $\text{CH}_4$  with  $\text{N}_2$ , Ar, and  $\text{H}_2$  in various proportions to analyze the influence of different collisional partner. For  $\text{N}_2$  and Ar some slight changes in the dephasing were observed, but  $\text{H}_2$  affected the rate of dephasing the most which is attributed to larger discrepancy between neighboring rotational states and probability of energy transfer during a collision. A critical probe delay was determined at  $\tau_{pr} = 80$  ps, corresponding to the extent of the previous collision-free measurements. Following this, analysis of the dephasing variations and collision probabilities of different probe delays led to the defining of a collision sensitivity time between 80 and 125 ps, during which the measurements are not collision-free but are weakly influenced by the collisional partners. These results agree with previous findings in literature, where the collision sensitivity time for the  $\nu_1$  Q-branch was found to be approximately 100 ps [61].

Several limitations and assumptions are important to highlight for the applicability of the MEG linewidth model. First, the validation of the model was limited to room temperature and the MEG fitting parameters were reduced to  $\alpha$  and  $\beta$  out of four total parameters. Second, while differences in nuclear spin and rotational state symmetries were included in the time-domain response through the calculated MeCaSDa transitions, linewidths for the same quantum number  $J$  were assumed to be the same regardless of symmetry. Finally, the sum rule of the MEG scaling law is not entirely applicable for anisotropic, vibrationally degenerate  $\text{CH}_4 \nu_2$  spectra, making this method of linewidth calculation a first approximation.

The final experiment acquired point-wise measurements across a laminar  $\text{CH}_4$  diffusion flame to conduct CRS spectroscopy in the molecular fingerprint region. A set of 25 measurement locations across the flame capture spectra from the fuel stream, the combustion reaction zone, and the oxidizer stream outside the flame. Four main species were found in this spectral region: the  $\text{CH}_4 \nu_2$  ro-vibrational spectrum, the  $\text{CO}_2$  Fermi dyad, the  $\text{O}_2$  ro-vibrational spectrum, and pure-rotational lines of  $\text{H}_2$ . Through the presence and intensity of the species' spectra, inferences could be made about the reaction progress and combustion mechanisms such as  $\text{CH}_4$  dissociation,  $\text{H}_2$  creation and consumption, and the recirculation and diffusion of  $\text{CO}_2$ . With this information obtained from a purely qualitative assessment, there is a positive outlook for CRS spectroscopy of the  $\text{CH}_4 \nu_2$  mode and its use in *in-situ* diagnostics for thermometry and concentration measurements.

While the thesis results are satisfactory and lay the foundation for the characterization of the  $\text{CH}_4 \nu_2$  mode, a few recommendations can be given for any continuation of the work. Because the CRS measurements were mainly conducted under ambient conditions several aspects of the model were unfulfilled, such as validation and parameter fitting at high temperatures, which would be beneficial for combustion. In addition, the length of the achievable probe delay was limited by the CRS signal of the  $\nu_2$  mode but could be slightly supplemented through an initially higher exposure time at the expense of single-shot measurements. The intensity-scaling reconciliation between the two datasets of the probe delays led to only a minor difference in fitting, but repeating this process again to extend the delay might include measurements with worse signal-to-background ratios and skew the linewidth fitting.

For further work on modeling, the MEG scaling law for linewidths could be expanded in various ways, such as utilizing all four fitting parameters with temperature-varying experimental data. Moreover, the time-domain model would benefit from validation at high temperature and with various pressures, relevant to those found in combustion environments. Last, the MEG model should include adjustments for the symmetry-specificity of rotational states and its sum rule to fully account for the anisotropic, vibrationally degenerate spectra of the  $\text{CH}_4 \nu_2$  ro-vibrational mode.

# Bibliography

- [1] IPCC, “Global Warming of 1.5°C. An IPCC Special Report on the impacts of global warming of 1.5°C above pre-industrial levels and related global greenhouse gas emission pathways, in the context of strengthening the global response to the threat of climate change, sustainable development, and efforts to eradicate poverty,” *Intergovernmental Panel on Climate Change, Special Report*, 2018. DOI: 10.1017/9781009157940.
- [2] D. Lee *et al.*, “Aviation and global climate change in the 21st century,” *Atmospheric Environment*, vol. 43, no. 22-23, pp. 3520–3537, Jul. 2009. DOI: 10.1016/j.atmosenv.2009.04.024.
- [3] S. Yim *et al.*, “Global, regional and local health impacts of civil aviation emissions,” *Environmental Research Letters*, vol. 10, no. 3, p. 034 001, Mar. 2015. DOI: 10.1088/1748-9326/10/3/034001.
- [4] ICAO, “2019 Environmental Report,” International Civil Aviation Organization, Tech. Rep., 2019, publisher: International Civil Aviation Organization. [Online]. Available: <https://www.icao.int/environmental-protection/Pages/envrep2019.aspx>.
- [5] S. E. Takriti, N. Pavlenko, and S. Y. Searle, “Mitigating International Aviation Emissions: Risks and Opportunities for Alternative Jet Fuels,” 2017.
- [6] *Our Commitment to Fly Net Zero by 2050*, English, publisher: International Air Transport Association, 2022. [Online]. Available: <https://www.iata.org/en/programs/environment/flynetzero/>.
- [7] J. Hileman, E. De La Rosa Blanco, P. Bonnefoy, and N. Carter, “The carbon dioxide challenge facing aviation,” *Progress in Aerospace Sciences*, vol. 63, pp. 84–95, Nov. 2013. DOI: 10.1016/j.paerosci.2013.07.003.
- [8] S. Blakey, L. Rye, and C. Wilson, “Aviation gas turbine alternative fuels: A review,” *Proceedings of the Combustion Institute*, vol. 33, no. 2, pp. 2863–2885, Jan. 2011. DOI: 10.1016/j.proci.2010.09.011.
- [9] W. Oberkampf and T. Trucano, “Verification and validation in computational fluid dynamics,” *Progress in Aerospace Sciences*, vol. 38, pp. 210–263, Mar. 1, 2002. DOI: 10.2172/793406.
- [10] A. Eckbreth, *Laser diagnostics for combustion temperature and species*, 1996. DOI: 10.1201/9781003077251.
- [11] K. Kohse-Höinghaus, R. Barlow, M. Aldén, and J. Wolfrum, “Combustion at the focus: Laser diagnostics and control,” *Proceedings of the Combustion Institute*, vol. 30, no. 1, pp. 89–123, Jan. 2005. DOI: 10.1016/j.proci.2004.08.274.
- [12] M. Aldén, J. Bood, Z. Li, and M. Richter, “Visualization and understanding of combustion processes using spatially and temporally resolved laser diagnostic techniques,” *Proceedings of the Combustion Institute*, vol. 33, no. 1, pp. 69–97, 2011. DOI: 10.1016/j.proci.2010.09.004.
- [13] R. Barlow, “Laser diagnostics and their interplay with computations to understand turbulent combustion,” *Proceedings of the Combustion Institute*, vol. 31, no. 1, pp. 49–75, Jan. 2007. DOI: 10.1016/j.proci.2006.08.122.
- [14] S. Roy, J. Gord, and A. Patnaik, “Recent advances in coherent anti-stokes raman scattering spectroscopy: Fundamental developments and applications in reacting flows,” *Progress in Energy and Combustion Science*, vol. 36, no. 2, pp. 280–306, Apr. 2010. DOI: 10.1016/j.peecs.2009.11.001.
- [15] G. Herzberg, *The spectra and structures of simple free radicals: An introduction to molecular spectroscopy*. Cornell University Press, 1971.
- [16] J. Hollas, *Modern Spectroscopy*. Hoboken, NJ: J. Wiley, 2004.

- [17] M. Dresselhaus, G. Dresselhaus, and A. Jorio, *Group Theory*. Berlin, Heidelberg: Springer-Verlag, 2008.
- [18] W Tolles, J Nibler, J McDonald, and A Harvey, "A review of the theory and application of coherent anti-stokes raman spectroscopy (cars)," *Applied Spectroscopy*, vol. 31, no. 4, pp. 253–271, Jul. 1977. DOI: 10.1366/00037027774463625.
- [19] R Boyd, *Nonlinear Optics*. Boston: Academic Press, 2008.
- [20] H. Rigneault and P. Berto, "Tutorial: Coherent raman light matter interaction processes," *APL Photonics*, vol. 3, no. 9, p. 091101, Sep. 2018. DOI: 10.1063/1.5030335.
- [21] A. Bohlin, "Development and application of pure rotational CARS for reactive flows," PhD, Lund University, Division of Combustion Physics, 2012.
- [22] S Chandra, A Compaan, and E Wiener-Avneer, "Phase matching in coherent anti-stokes raman scattering," *Journal of Raman Spectroscopy*, vol. 10, no. 1, pp. 103–105, Jan. 1981. DOI: 10.1002/jrs.1250100118.
- [23] W Demtröder, *Laser Spectroscopy*. Berlin: Springer, 2008.
- [24] A. Eckbreth, "Boxcars: Crossed beam phase matched cars generation in gases," *Applied Physics Letters*, vol. 32, no. 7, pp. 421–423, Apr. 1978. DOI: 10.1063/1.90070.
- [25] H. Lotem, R Lynch, and N Bloembergen, "Interference between raman resonances in four-wave difference mixing," *Physical Review A*, vol. 14, no. 5, pp. 1748–1755, Nov. 1, 1976. DOI: 10.1103/physreva.14.1748.
- [26] T. Meyer, S. Roy, and J. Gord, "Improving signal-to-interference ratio in rich hydrocarbon—air flames using picosecond coherent anti-stokes raman scattering," *Applied Spectroscopy*, vol. 61, no. 11, pp. 1135–1140, Nov. 2007. DOI: 10.1366/000370207782596996.
- [27] D. Richardson, R. Lucht, S. Roy, and J. Gord, "Single-pulse femtosecond coherent anti-stokes raman scattering (cars) spectroscopy for temperature measurements at data rates of 1 khz," in Orlando, Florida: American Institute of Aeronautics and Astronautics, Jan. 5, 2009. DOI: 10.2514/6.2009-527.
- [28] A. Bohlin, B. Patterson, and C. Kliewer, "Communication: Simplified two-beam rotational cars signal generation demonstrated in 1d," *The Journal of Chemical Physics*, vol. 138, no. 8, p. 081102, Feb. 28, 2013. DOI: 10.1063/1.4793556.
- [29] L. Martinsson, P. Bengtsson, M. Aldén, S. Kröll, and J. Bonamy, "A test of different rotational raman linewidth models: Accuracy of rotational coherent anti stokes raman scattering thermometry in nitrogen from 295 to 1850 k," *The Journal of Chemical Physics*, vol. 99, no. 4, pp. 2466–2477, Aug. 15, 1993. DOI: 10.1063/1.466197.
- [30] M. Maiuri, M. Garavelli, and G. Cerullo, "Ultrafast spectroscopy: State of the art and open challenges," *Journal of the American Chemical Society*, vol. 142, no. 1, pp. 3–15, Jan. 2020. DOI: 10.1021/jacs.9b10533.
- [31] H. Kuramochi and T. Tahara, "Tracking ultrafast structural dynamics by time-domain raman spectroscopy," *Journal of the American Chemical Society*, vol. 143, no. 26, pp. 9699–9717, Jul. 2021. DOI: 10.1021/jacs.1c02545.
- [32] S. Roy, T. Meyer, and J. Gord, "Time-resolved dynamics of resonant and nonresonant broadband picosecond coherent anti-stokes raman scattering signals," *Applied Physics Letters*, vol. 87, no. 26, p. 264103, Dec. 26, 2005. DOI: 10.1063/1.2159576.
- [33] D Richardson, R Lucht, W Kulatilaka, S Roy, and J Gord, "Theoretical modeling of single-laser-shot, chirped-probe-pulse femtosecond coherent anti-stokes raman scattering thermometry," *Applied Physics B*, vol. 104, no. 3, pp. 699–714, Sep. 2011. DOI: 10.1007/s00340-011-4489-0.
- [34] R. Lucht, S. Roy, T. Meyer, and J. Gord, "Femtosecond coherent anti-stokes raman scattering measurement of gas temperatures from frequency-spread dephasing of the raman coherence," *Applied Physics Letters*, vol. 89, no. 25, p. 251112, Dec. 18, 2006. DOI: 10.1063/1.2410237.

- [35] B. Prince, A. Chakraborty, B. Prince, and H. Stauffer, "Development of simultaneous frequency- and time-resolved coherent anti-stokes raman scattering for ultrafast detection of molecular raman spectra," *The Journal of Chemical Physics*, vol. 125, no. 4, p. 044 502, Jul. 28, 2006. DOI: 10.1063/1.2219439.
- [36] J. Miller, M. Slipchenko, T. Meyer, H. Stauffer, and J. Gord, "Hybrid femtosecond/picosecond coherent anti-stokes raman scattering for high-speed gas-phase thermometry," *Optics Letters*, vol. 35, no. 14, p. 2430, Jul. 13, 2010. DOI: 10.1364/ol.35.002430.
- [37] J. Miller, S. Roy, M. Slipchenko, J. Gord, and T. Meyer, "Single-shot gas-phase thermometry using pure-rotational hybrid femtosecond/picosecond coherent anti-stokes raman scattering," *Optics Express*, vol. 19, no. 16, p. 15 627, Aug. 2011. DOI: 10.1364/oe.19.015627.
- [38] J. Miller, M. Slipchenko, and T. Meyer, "Probe-pulse optimization for nonresonant suppression in hybrid fs/ps coherent anti-stokes raman scattering at high temperature," *Optics Express*, vol. 19, no. 14, p. 13 326, Jul. 2011. DOI: 10.1364/oe.19.013326.
- [39] H. Stauffer *et al.*, "Time- and frequency-dependent model of time-resolved coherent anti-stokes raman scattering (cars) with a picosecond-duration probe pulse," *The Journal of Chemical Physics*, vol. 140, no. 2, p. 024 316, Jan. 14, 2014. DOI: 10.1063/1.4860475.
- [40] G. Myhre *et al.*, "Anthropogenic and natural radiative forcing," in *Climate Change 2013: The Physical Science Basis. Contribution of Working Group I to the Fifth Assessment Report of the Intergovernmental Panel on Climate Change*, T. F. Stocker *et al.*, Eds. Cambridge, UK: Cambridge University Press, 2013, pp. 659–740. DOI: 10.1017/CBO9781107415324.018.
- [41] B. Amyay, M. Louviot, O. Pirali, R. Georges, J. Vander Auwera, and V. Boudon, "Global analysis of the high temperature infrared emission spectrum of  $12\text{ch}_4$  in the dyad ( $\nu_2/\nu_4$ ) region," *The Journal of Chemical Physics*, vol. 144, no. 2, p. 024 312, Jan. 14, 2016. DOI: 10.1063/1.4939521.
- [42] B. Amyay *et al.*, "New investigation of the  $\nu_3$  c–h stretching region of  $12\text{ch}_4$  through the analysis of high temperature infrared emission spectra," *The Journal of Chemical Physics*, vol. 148, no. 13, p. 134 306, Apr. 7, 2018. DOI: 10.1063/1.5023331.
- [43] G. Magnotti, U. Kc, P. Varghese, and R. Barlow, "Raman spectra of methane, ethylene, ethane, dimethyl ether, formaldehyde and propane for combustion applications," *Journal of Quantitative Spectroscopy and Radiative Transfer*, vol. 163, pp. 80–101, Sep. 2015. DOI: 10.1016/j.jqsrt.2015.04.018.
- [44] D. Bermejo, J. Santos, and P. Cancio, "High-resolution q-cw srs spectrum of  $12\text{ch}_4$  in the region of the level crossing between  $\nu_1$  and  $\nu_2 + \nu_4$ ," *Journal of Molecular Spectroscopy*, vol. 156, no. 1, pp. 15–21, Nov. 1992. DOI: 10.1016/0022-2852(92)90089-7.
- [45] A. Owyong, C. Patterson, and R. Mcdowell, "Cw stimulated raman gain spectroscopy of the  $\nu_1$  fundamental of methane," *Chemical Physics Letters*, vol. 59, no. 1, pp. 156–162, Nov. 1978. DOI: 10.1016/0009-2614(78)85638-3.
- [46] J. Barrett and R. Begley, "Low power cw generation of coherent anti-stokes raman radiation in  $\text{ch}_4$  gas," *Applied Physics Letters*, vol. 27, no. 3, pp. 129–131, Aug. 1975. DOI: 10.1063/1.88379.
- [47] M. Henesian, L. Kulevskii, and R. Byer, "Cw high resolution car spectroscopy of the q ( $\nu_1$ ) raman line of methane," *The Journal of Chemical Physics*, vol. 65, no. 12, pp. 5530–5531, Dec. 15, 1976. DOI: 10.1063/1.433015.
- [48] D. Kozlov, A. Prokhorov, and V. Smirnov, "The methane  $\nu_1(a_1)$  vibrational state rotational structure obtained from high resolution cars spectra of the q branch," *Journal of Molecular Spectroscopy*, vol. 77, no. 1, pp. 21–28, Jul. 1979. DOI: 10.1016/0022-2852(79)90191-7.
- [49] H. Frunder *et al.*, "Revised analysis of the structure of the  $\nu_1$  band of methane," *Chemical Physics Letters*, vol. 100, no. 1, pp. 110–114, Aug. 1983. DOI: 10.1016/0009-2614(83)87273-x.
- [50] J. Boquillon and R. Bregier, "High-resolution coherent stokes raman spectroscopy of the  $\nu_1$  and  $\nu_3$  bands of methane," *Applied Physics*, vol. 18, no. 2, pp. 195–198, Feb. 1979. DOI: 10.1007/bf00934415.

- [51] T Dreier, B Lange, J Wolfrum, and M Zahn, "Determination of temperature and concentration of molecular nitrogen, oxygen and methane with coherent anti-stokes raman scattering," *Applied Physics B Photophysics and Laser Chemistry*, vol. 45, no. 3, pp. 183–190, Mar. 1988. DOI: 10.1007/bf00695289.
- [52] M Ridder, A Suvernev, and T Dreier, "Collision effects in nitrogen and methane coherent anti stokes raman isotropic q branch spectra at high densities," *The Journal of Chemical Physics*, vol. 105, no. 9, pp. 3376–3386, Sep. 1996. DOI: 10.1063/1.472223.
- [53] S. Green, P. Rubas, M. Paul, J. Peters, and R. Lucht, "Annular phase-matched dual-pump coherent anti-stokes raman spectroscopy system for the simultaneous detection of nitrogen and methane," *Applied Optics*, vol. 37, no. 9, p. 1690, Mar. 20, 1998. DOI: 10.1364/ao.37.001690.
- [54] D Pieroni *et al.*, "Experimental and theoretical study of line mixing in methane spectra. iii. the q branch of the raman  $\nu_1$  band," *The Journal of Chemical Physics*, vol. 112, no. 3, pp. 1335–1343, Jan. 15, 2000. DOI: 10.1063/1.480597.
- [55] F Grisch *et al.*, "Cars spectroscopy of  $\text{CH}_4$  for implication of temperature measurements in supercritical  $\text{O}_2/\text{CH}_4$  combustion," *Aerospace Science and Technology*, vol. 11, no. 1, pp. 48–54, Jan. 2007. DOI: 10.1016/j.ast.2006.07.005.
- [56] E. Jourdanneau *et al.*, "Cars methane spectra: Experiments and simulations for temperature diagnostic purposes," *Journal of Molecular Spectroscopy*, vol. 246, no. 2, pp. 167–179, Dec. 2007. DOI: 10.1016/j.jms.2007.09.006.
- [57] A. Bohlin and C. Kliewer, "Two-beam ultrabroadband coherent anti-stokes raman spectroscopy for high resolution gas-phase multiplex imaging," *Applied Physics Letters*, vol. 104, no. 3, p. 031 107, Jan. 20, 2014. DOI: 10.1063/1.4862980.
- [58] A. Bohlin, C. Jainski, B. Patterson, A. Dreizler, and C. Kliewer, "Multiparameter spatio-thermochemical probing of flame-wall interactions advanced with coherent raman imaging," *Proceedings of the Combustion Institute*, vol. 36, no. 3, pp. 4557–4564, 2017. DOI: 10.1016/j.proci.2016.07.062.
- [59] C. Dedic, J. Miller, and T. Meyer, "Dual-pump vibrational/rotational femtosecond/picosecond coherent anti-stokes raman scattering temperature and species measurements," *Optics Letters*, vol. 39, no. 23, p. 6608, Dec. 2014. DOI: 10.1364/ol.39.006608.
- [60] S. Engel, J. Miller, C. Dedic, T. Seeger, A. Leipertz, and T. Meyer, "Hybrid femtosecond/picosecond coherent anti-stokes raman scattering for high-speed  $\text{CH}_4/\text{N}_2$  measurements in binary gas mixtures," *Journal of Raman Spectroscopy*, vol. 44, no. 10, pp. 1336–1343, Oct. 2013. DOI: 10.1002/jrs.4261.
- [61] T. Chen, C. Kliewer, B. Goldberg, E. Kolemen, and Y. Ju, "Time-domain modelling and thermometry of the  $\text{CH}_4$   $\nu_1$  q-branch using hybrid femtosecond/picosecond coherent anti-stokes raman scattering," *Combustion and Flame*, vol. 224, pp. 183–195, Feb. 2021. DOI: 10.1016/j.combustflame.2020.11.017.
- [62] J Kiefer, T Seeger, S Steuer, S Schorsch, M Weikl, and A Leipertz, "Design and characterization of a raman-scattering-based sensor system for temporally resolved gas analysis and its application in a gas turbine power plant," *Measurement Science and Technology*, vol. 19, no. 8, p. 085 408, Aug. 2008. DOI: 10.1088/0957-0233/19/8/085408.
- [63] E. Jourdanneau, F. Chaussard, R. Saint-Loup, T. Gabard, and H. Berger, "The methane raman spectrum from 1200 to  $5500\text{cm}^{-1}$ : A first step toward temperature diagnostic using methane as a probe molecule in combustion systems," *Journal of Molecular Spectroscopy*, vol. 233, no. 2, pp. 219–230, Oct. 2005. DOI: 10.1016/j.jms.2005.07.004.
- [64] T Butterworth *et al.*, "Quantifying methane vibrational and rotational temperature with raman scattering," *Journal of Quantitative Spectroscopy and Radiative Transfer*, vol. 236, p. 106 562, Oct. 2019. DOI: 10.1016/j.jqsrt.2019.07.005.
- [65] D. Petrov and I. Matrosov, "Raman gas analyzer (rga): Natural gas measurements," *Applied Spectroscopy*, vol. 70, no. 10, pp. 1770–1776, Oct. 2016. DOI: 10.1177/0003702816644611.

- [66] D Petrov, "Raman spectrum of methane in the range 20–40°C," *Journal of Applied Spectroscopy*, vol. 84, no. 3, pp. 420–424, Jul. 2017. DOI: 10.1007/s10812-017-0486-3.
- [67] D. V. Petrov, "Pressure dependence of peak positions, half widths, and peak intensities of methane raman bands ( $\nu_2$ ,  $2\nu_4$ ,  $\nu_1$ ,  $\nu_3$ , and  $2\nu_2$ )," *Journal of Raman Spectroscopy*, vol. 48, no. 11, pp. 1426–1430, 2017. DOI: <https://doi.org/10.1002/jrs.5141>.
- [68] D Petrov, "Raman spectrum of methane in nitrogen, carbon dioxide, hydrogen, ethane, and propane environments," *Spectrochimica Acta Part A: Molecular and Biomolecular Spectroscopy*, vol. 191, pp. 573–578, Feb. 2018. DOI: 10.1016/j.saa.2017.10.058.
- [69] R Tipping, A. Brown, Q Ma, J Hartmann, C Boulet, and J Liévin, "Collision-induced absorption in the  $\nu_2$  fundamental band of  $\text{CH}_4$ . i. determination of the quadrupole transition moment," *The Journal of Chemical Physics*, vol. 115, no. 19, pp. 8852–8857, Nov. 15, 2001. DOI: 10.1063/1.1408915.
- [70] T Gabard, I Grigoriev, N Grigorovich, and M Tonkov, "Helium and argon line broadening in the  $\nu_2$  band of  $\text{CH}_4$ ," *Journal of Molecular Spectroscopy*, vol. 225, no. 2, pp. 123–131, Jun. 2004. DOI: 10.1016/j.jms.2004.02.023.
- [71] D. A. Long, *The Raman Effect: A unified treatment of the theory of Raman scattering by molecules*. Wiley, 2002.
- [72] A. Bohlin, P.-E. Bengtsson, and M. Marrocco, "On the sensitivity of rotational raman thermometry to the herman–wallis factor," *Journal of Raman Spectroscopy*, vol. 42, no. 10, pp. 1843–1847, 2011. DOI: <https://doi.org/10.1002/jrs.2869>. [Online]. Available: <https://analyticalsciencejournals.onlinelibrary.wiley.com/doi/abs/10.1002/jrs.2869>.
- [73] J. P. Champion, M. Loëte, and G. Pierre, "Spherical top spectra," in *Spectroscopy of the Earth's Atmosphere and Interstellar Medium*, K. N. Rao and A. Weber, Eds., Jan. 1992, pp. 339–422.
- [74] V. Boudon, J. Champion, T. Gabard, M. Loëte, M. Rotger, and C. Wenger, "Spherical top theory and molecular spectra," in Sep. 2011, vol. 3, ISBN: 9780470749593. DOI: 10.1002/9780470749593.hrs021.
- [75] W. Kulatilaka, P. Hsu, H. Stauffer, J. Gord, and S. Roy, "Direct measurement of rotationally resolved  $\text{H}_2$  q-branch raman coherence lifetimes using time-resolved picosecond coherent anti-stokes raman scattering," *Applied Physics Letters*, vol. 97, no. 8, p. 081112, Aug. 23, 2010. DOI: 10.1063/1.3483871.
- [76] J. Miller, S. Roy, J. Gord, and T. Meyer, "Communication: Time-domain measurement of high-pressure  $\text{N}_2$  and  $\text{O}_2$  self-broadened linewidths using hybrid femtosecond/picosecond coherent anti-stokes raman scattering," *The Journal of Chemical Physics*, vol. 135, no. 20, p. 201104, Nov. 28, 2011. DOI: 10.1063/1.3665932.
- [77] C Kliewer, A Bohlin, E Nordström, B Patterson, P.-E. Bengtsson, and T Settersten, "Time-domain measurements of s-branch  $\text{N}_2$ – $\text{N}_2$  raman linewidths using picosecond pure rotational coherent anti-stokes raman spectroscopy," *Applied Physics B*, vol. 108, no. 2, pp. 419–426, Aug. 2012. DOI: 10.1007/s00340-012-5037-2.
- [78] A. Hosseinnia, M. Ruchkina, P. Ding, P.-E. Bengtsson, and J. Bood, "Simultaneous temporally and spectrally resolved raman coherences with single-shot fs/ns rotational rams," *Optics Letters*, vol. 45, no. 2, p. 308, Jan. 6, 2020. DOI: 10.1364/ol.380247.
- [79] S. Roy *et al.*, "Direct measurements of collisionally broadened raman linewidths of  $\text{CO}_2$  s-branch transitions," *The Journal of Chemical Physics*, vol. 138, no. 2, p. 024201, Jan. 14, 2013. DOI: 10.1063/1.4774093.
- [80] M. Strelakov, "Rotational energy relaxation in  $\text{CH}_4$  and  $\text{CH}_4$ -He, Ar collisions calculated from coherent and stimulated raman spectroscopy data," *Molecular Physics*, vol. 100, no. 7, pp. 1049–1056, Apr. 10, 2002. DOI: 10.1080/00268970110109862.
- [81] L Rahn and R Palmer, "Studies of nitrogen self-broadening at high temperature with inverse raman spectroscopy," *Journal of the Optical Society of America B*, vol. 3, no. 9, p. 1164, Sep. 1, 1986. DOI: 10.1364/josab.3.001164.

- [82] M. L. Dubernet *et al.*, "The virtual atomic and molecular data centre (VAMDC) consortium," *Journal of Physics B: Atomic, Molecular and Optical Physics*, vol. 49, no. 7, p. 074 003, 2016. DOI: 10.1088/0953-4075/49/7/074003. [Online]. Available: <https://doi.org/10.1088/0953-4075/49/7/074003>.
- [83] Y. A. Ba *et al.*, "Mecasda and ecasda: Methane and ethene calculated spectroscopic databases for the virtual atomic and molecular data centre," *Journal of Quantitative Spectroscopy and Radiative Transfer*, vol. 130, pp. 62–68, 2013, HITRAN2012 special issue, ISSN: 0022-4073. DOI: <https://doi.org/10.1016/j.jqsrt.2013.05.001>. [Online]. Available: <https://www.sciencedirect.com/science/article/pii/S0022407313001933>.
- [84] C. Wenger, V. Boudon, M. Rotger, M. Sanzharov, and J.-P. Champion, "Xtds and spview: Graphical tools for the analysis and simulation of high-resolution molecular spectra," *Journal of Molecular Spectroscopy*, vol. 251, no. 1, pp. 102–113, 2008, ISSN: 0022-2852. DOI: <https://doi.org/10.1016/j.jms.2008.01.011>. [Online]. Available: <https://www.sciencedirect.com/science/article/pii/S0022285208000532>.
- [85] A. Couairon and A. Mysyrowicz, "Femtosecond filamentation in transparent media," *Physics Reports*, vol. 441, no. 2, pp. 47–189, 2007, ISSN: 0370-1573. DOI: <https://doi.org/10.1016/j.physrep.2006.12.005>. [Online]. Available: <https://www.sciencedirect.com/science/article/pii/S037015730700021X>.
- [86] C. A. Lieber and A. Mahadevan-Jansen, "Automated method for subtraction of fluorescence from biological raman spectra," *Applied Spectroscopy*, vol. 57, no. 11, pp. 1363–1367, 2003, PMID: 14658149. DOI: 10.1366/000370203322554518. eprint: <https://doi.org/10.1366/000370203322554518>. [Online]. Available: <https://doi.org/10.1366/000370203322554518>.
- [87] A. Savitzky and M. J. E. Golay, "Smoothing and differentiation of data by simplified least squares procedures.," *Analytical Chemistry*, vol. 36, no. 8, pp. 1627–1639, 1964. DOI: 10.1021/ac60214a047. eprint: <https://doi.org/10.1021/ac60214a047>. [Online]. Available: <https://doi.org/10.1021/ac60214a047>.
- [88] T. L. Courtney and C. J. Kliewer, "Rotational coherence beating in molecular oxygen: Coupling between electronic spin and nuclear angular momenta," *The Journal of Chemical Physics*, vol. 149, no. 23, p. 234 201, 2018. DOI: 10.1063/1.5058766. eprint: <https://doi.org/10.1063/1.5058766>. [Online]. Available: <https://doi.org/10.1063/1.5058766>.
- [89] T. Y. Chen, N. Liu, C. J. Kliewer, A. Dogariu, E. Kolemen, and Y. Ju, "Simultaneous single-shot rotation–vibration non-equilibrium thermometry using pure rotational fs/ps cars coherence beating," *Opt. Lett.*, vol. 47, no. 6, pp. 1351–1354, 2022. DOI: 10.1364/OL.453272. [Online]. Available: <https://opg.optica.org/ol/abstract.cfm?URI=ol-47-6-1351>.
- [90] F. Mazza, N. Griffioen, L. Castellanos, D. Kliukin, and A. Bohlin, "High-temperature rotational-vibrational o<sub>2</sub> co<sub>2</sub> coherent raman spectroscopy with ultrabroadband femtosecond laser excitation generated in-situ," *Combustion and Flame*, vol. 237, p. 111 738, Mar. 2022. DOI: 10.1016/j.combustflame.2021.111738.
- [91] R. A. Olafson, M. A. Thomas, and H. L. Welsh, "The raman spectrum of methane-d<sub>4</sub>," *Canadian Journal of Physics*, vol. 39, no. 3, pp. 419–436, 1961. DOI: 10.1139/p61-042. eprint: <https://doi.org/10.1139/p61-042>. [Online]. Available: <https://doi.org/10.1139/p61-042>.
- [92] C. Wenger and J. Champion, "Spherical top data system (stds) software for the simulation of spherical top spectra," *Journal of Quantitative Spectroscopy and Radiative Transfer*, vol. 59, no. 3, pp. 471–480, 1998, Atmospheric Spectroscopy Applications 96, ISSN: 0022-4073. DOI: [https://doi.org/10.1016/S0022-4073\(97\)00106-4](https://doi.org/10.1016/S0022-4073(97)00106-4). [Online]. Available: <https://www.sciencedirect.com/science/article/pii/S0022407397001064>.
- [93] J.-P. Champion, G. Pierre, H. Berger, and J. Cadot, "Vibration-rotation energies of harmonic and combination levels in tetrahedral xy<sub>4</sub> molecules: Analysis of the 2v<sub>2</sub> and v<sub>2</sub> + v<sub>4</sub> bands of 12ch<sub>4</sub>," *Journal of Molecular Spectroscopy*, vol. 79, no. 2, pp. 281–294, 1980, ISSN: 0022-2852. DOI: [https://doi.org/10.1016/0022-2852\(80\)90214-3](https://doi.org/10.1016/0022-2852(80)90214-3). [Online]. Available: <https://www.sciencedirect.com/science/article/pii/0022285280902143>.

- [94] A. K. Patnaik, S. Roy, and J. R. Gord, "Saturation of vibrational coherent anti-stokes raman scattering mediated by saturation of the rotational raman transition," *Phys. Rev. A*, vol. 87, p. 043801, 4 2013. DOI: 10.1103/PhysRevA.87.043801. [Online]. Available: <https://link.aps.org/doi/10.1103/PhysRevA.87.043801>.
- [95] M. Linne, N. T. Mecker, C. J. Kliewer, D. Escofet-Martin, and B. Peterson, "Revisiting n<sub>2</sub>-n<sub>2</sub> collisional linewidth models for s-branch rotational raman scattering," *Combustion and Flame*, vol. 243, p. 111928, 2022, A dedication to Professor Katharina Kohse-Höinghaus, ISSN: 0010-2180. DOI: <https://doi.org/10.1016/j.combustflame.2021.111928>. [Online]. Available: <https://www.sciencedirect.com/science/article/pii/S0010218021006714>.
- [96] E. B. Wilson, "The statistical weights of the rotational levels of polyatomic molecules, including methane, ammonia, benzene, cyclopropane and ethylene," *The Journal of Chemical Physics*, vol. 3, no. 5, pp. 276–285, 1935. DOI: 10.1063/1.1749653. eprint: <https://doi.org/10.1063/1.1749653>. [Online]. Available: <https://doi.org/10.1063/1.1749653>.
- [97] G. Fanjoux, B. Lavorel, and G. Millot, "Collisional shifting and broadening coefficients for the rovibrational anisotropic lines of the v<sub>1</sub>/2v<sub>2</sub> fermi dyad in co<sub>2</sub> gas studied by stimulated raman spectroscopy," *Journal of Raman Spectroscopy*, vol. 29, no. 5, pp. 391–397, 1998. DOI: [https://doi.org/10.1002/\(SICI\)1097-4555\(199805\)29:5<391::AID-JRS251>3.0.CO;2-N](https://doi.org/10.1002/(SICI)1097-4555(199805)29:5<391::AID-JRS251>3.0.CO;2-N). eprint: <https://analyticalsciencejournals.onlinelibrary.wiley.com/doi/pdf/10.1002/%28SICI%291097-4555%28199805%2929%3A5%3C391%3A%3AAID-JRS251%3E3.0.CO%3B2-N>. [Online]. Available: <https://analyticalsciencejournals.onlinelibrary.wiley.com/doi/abs/10.1002/%28SICI%291097-4555%28199805%2929%3A5%3C391%3A%3AAID-JRS251%3E3.0.CO%3B2-N>.
- [98] L. Bonamy, J. Bonamy, D. Robert, S. I. Temkin, G. Millot, and B. Lavorel, "Line coupling in anisotropic raman branches," *The Journal of Chemical Physics*, vol. 101, no. 9, pp. 7350–7356, 1994. DOI: 10.1063/1.468293. eprint: <https://doi.org/10.1063/1.468293>. [Online]. Available: <https://doi.org/10.1063/1.468293>.
- [99] J. Boissoles, C. Boulet, D. Robert, and S. Green, "State-to-state rotational phase coherence effect on the vibration-rotation band shape: An accurate quantum calculation for co-he," *The Journal of Chemical Physics*, vol. 90, no. 10, pp. 5392–5398, 1989. DOI: 10.1063/1.456688. eprint: <https://doi.org/10.1063/1.456688>. [Online]. Available: <https://doi.org/10.1063/1.456688>.
- [100] N. Owschimikow *et al.*, "Cross sections for rotational decoherence of perturbed nitrogen measured via decay of laser-induced alignment," *The Journal of Chemical Physics*, vol. 133, no. 4, p. 044311, 2010. DOI: 10.1063/1.3464487. eprint: <https://doi.org/10.1063/1.3464487>. [Online]. Available: <https://doi.org/10.1063/1.3464487>.
- [101] A. Pine, "Line mixing sum rules for the analysis of multiplet spectra," *Journal of Quantitative Spectroscopy and Radiative Transfer*, vol. 57, no. 2, pp. 145–155, 1997, ISSN: 0022-4073. DOI: [https://doi.org/10.1016/S0022-4073\(96\)00129-X](https://doi.org/10.1016/S0022-4073(96)00129-X). [Online]. Available: <https://www.sciencedirect.com/science/article/pii/S002240739600129X>.
- [102] S. Temkin, L. Bonamy, J. Bonamy, and D. Robert, "Angular-momentum coupling in spectroscopic relaxation cross sections: Consequences for line coupling in bending bands," *Phys. Rev. A*, vol. 47, pp. 1543–1546, 2 1993. DOI: 10.1103/PhysRevA.47.1543. [Online]. Available: <https://link.aps.org/doi/10.1103/PhysRevA.47.1543>.



# Acknowledgements

I will try my best to encapsulate the gratitude that I have for all the people that helped me during my thesis. I truly could not have done this without their knowledge, kindness, and support.

First, I would like to thank Francesco Mazza who was my daily supervisor throughout the project. I know you had many responsibilities in the lab, but you still took me on as an MSc student and helped to bring me from barely knowing the ordering of the spectral branches to being able to articulate some of the finer points of group theory and quantum mechanics. Many times, I would ask a single question and our discussion would essentially become a full lecture covering all tangentially related aspects. This helped me fully comprehend the information I needed to complete my thesis and more. Additionally, our many long hours in the lab during the experimental campaign were bearable because of our conversations and finding out which songs were actually audible over the 1 kHz tone of the laser. Thank you for dedicating so much of your time to my academic growth. As your last MSc student in this group, I hope you can now finish your PhD with some relative peace and I look forward to seeing your future endeavors.

Next, I would like thank Alexis Bohlin, my principal supervisor in this thesis. When I was initially choosing my thesis topic, I remembered the fun I had during the experimental section of your combustion course. I was convinced to join your group once one of my friends had told me about your approachability and patience as a supervisor. Not only have you lived up to what I had heard, but throughout my thesis you continued to offer me support and opportunities that have shaped the direction of my work and ultimately my chosen career path. Beyond that, I enjoyed our conversations about science, life abroad, and the macabre details of the ättestupa along the Kungsleden. I wish you all the best personally and in your future laser diagnostics research.

To complete the four horsemen of the Advanced Laser Diagnostics and Flames lab, I would like to extend my thanks to Leonardo Castellanos and Dmitrii Kliukin. Even if you were busy, you would still make time to answer my questions, teach me how to use the lab equipment, or even just to chat. I share the sentiment of my fellow MSc students that your presence in the lab contributed to its atmosphere and made it an enjoyable place to work.

Finally, I would like to express my undying gratitude and love to my friends and to my family. For my friends, you provided a much-needed respite and tolerated my incoherent ramblings on many evenings. You made life in Delft very fun and have given me many good memories to look back on during my time in graduate school. For my family, we have been separated for one of the longest consecutive times over the past couple of years. I can't wait to finally return to you and tell you about everything that I have learned. Your encouragement and belief in me have kept me going, and I am proud to share this achievement with you. Last, but not least, my partner. You have been present for my worst failures and best accomplishments and have handled all of it with such grace. Thank you for making me excited for the future.